

**ADVANCED CONTROL OF A MULTI-PORT AUTONOMOUS  
RECONFIGURABLE SOLAR POWER PLANT**

A Dissertation  
Presented to  
The Academic Faculty

by

Qianxue Xia

In Partial Fulfillment  
of the Requirements for the Degree  
Doctor of Philosophy in the  
School of Electrical and Computer Engineering

Georgia Institute of Technology  
December 2022

**COPYRIGHT © 2022 BY QIANXUE XIA**

# **ADVANCED CONTROL OF A MULTI-PORT AUTONOMOUS RECONFIGURABLE SOLAR POWER PLANT**

Approved by:

Dr. Maryam Saeedifard, Advisor  
School of Electrical and Computer  
Engineering  
*Georgia Institute of Technology*

Dr. Mahshid Amirabadi  
School of Electrical and Computer  
Engineering  
*Northeastern University*

Dr. Lukas Graber  
School of Electrical and Computer  
Engineering  
*Georgia Institute of Technology*

Dr. Suman Debnath  
Electrical and Electronics Systems  
Research Division  
*Oak Ridge National Laboratory*

Dr. Santiago Carlos Grijalva  
School of Electrical and Computer  
Engineering  
*Georgia Institute of Technology*

Date Approved: Nov 28, 2022

Deliciated to my husband and parents.

## ACKNOWLEDGEMENTS

Ph.D. has been an important part of my life journey, filled with challenges, happiness, upset, and growth. It's a mix of good and bad phases, but all the bad phases have been turned into good ones with the help and encouragement of many people. I would like to express my appreciation to all of them.

First and foremost, I am greatly indebted to my supervisor, Dr. Maryam Saeedifard, for her excellent supervision, immense knowledge, and continuous encouragement during my studies. It has been a great privilege and honor to pursue my higher education under her supervision.

Furthermore, I thank my Ph.D. examination committee, Dr. Lukas Graber, Dr. Santiago Grijalva, Dr. Mahshid Amirabadi, and Dr. Suman Debnath, for serving in my thesis committee and reviewing my dissertation. Especially, I would like to thank Dr. Debnath for guiding me through the whole MARS project.

I extend my sincere appreciation to my friends in Prof. Seedifards's group. Among them, I would like to especially thank Dr. Mahmoud Mehrabankhomartash, Dr. Xiangyu Han, Shiyuan Ying, and Dr. Jingfan Sun for their help in research and life. I am also thankful to Dr. Phani Marthi and Dr. Shilpa Marti at ORNL for their fellowship.

Finally, I owe special thanks to my parents and my husband. No amount of words will be enough to tell how grateful I am to you. Thank you for your endless love and support.



# TABLE OF CONTENTS

<b>ACKNOWLEDGEMENTS</b>	<b>v</b>
<b>LIST OF TABLES</b>	<b>ix</b>
<b>LIST OF FIGURES</b>	<b>x</b>
<b>SUMMARY</b>	<b>xv</b>
<b>CHAPTER 1. Introduction</b>	<b>1</b>
1.1 Motivation and Statement of the Problem	1
1.2 Objective of the Research	7
1.3 Literature Survey Pertinent to the Thesis Objectives	11
1.3.1 ML-Based EBC Criteria of the MARS	11
1.3.2 NN-based EBC of the MARS	15
1.3.3 MPC of the MARS	17
1.4 Thesis Outline	19
<b>CHAPTER 2. Modelling of the MARS</b>	<b>21</b>
2.1 MARS Circuit Architecture	22
2.2 Reduced-Order Model of the MARS	23
2.3 High-Fidelity Model of MARS	25
2.3.1 PV SM	26
2.3.2 ESS SM	28
2.3.3 Normal SM	29
2.4 Simulation Algorithms	29
2.4.1 Hybrid Discretization	30
2.4.2 Interpolating Method	32
2.5 Simulation Results and Comparison	34
2.5.1 Single DAB	35
2.5.2 MARS	37
2.6 Summary	39
<b>CHAPTER 3. Hierarchical Control of the MARS</b>	<b>41</b>
3.1 L1 Control	41
3.1.1 qd Current Controller	42
3.1.2 Circulating Current Controller	43
3.1.3 Energy Balancing Control	45
3.2 L2 control	50
3.3 L3 Control	53
3.4 PSCAD Offline Simulation of High-fidelity Model of the MARS	53
3.4.1 Cyclic Test Under Various Operating Conditions	54
3.4.2 The MARS System Under Different Grid Events	56
3.5 Standard Compliance of the MARS	60

3.6	Summary	61
<b>CHAPTER 4. Machine Learning-Based EBC Criteria of the MARS</b>		<b>62</b>
4.1	Dynamics of the Capacitor SM Voltage Differences	62
4.2	EBC Criteria	64
4.2.1	Impact of Capacitor Voltage Balancing Algorithms	65
4.2.2	ML-Based EBC Criteria	67
4.3	Simulation Results	73
4.4	cHIL Results	76
4.4.1	cHIL System Setup	76
4.4.2	cHIL Test Results	78
4.5	Summary	84
<b>CHAPTER 5. NN-Based EBC of the MARS and Power Mismatch Elimination Strategy</b>		<b>87</b>
5.1	Power Mismatch Elimination Strategy of the MARS	88
5.1.1	Inter-SM Power Mismatch Elimination	89
5.1.2	Inter-Phase Power Mismatch Elimination	90
5.1.3	Inter-Arm Power Mismatch Elimination	93
5.2	NN-Based EBC Control	94
5.2.1	Introduction of NN	94
5.2.2	Data Acquisition and Model Training	96
5.2.3	ANN vs NARX	97
5.2.4	Comparison of Existing EBC Methods	99
5.3	Simulation Results	101
5.3.1	Arm Power Mismatch Balanced	101
5.3.2	Phase Power Mismatch Balanced	107
5.4	cHIL Results	112
5.4.1	EBC Transition from Disabled to Enabled under Unstable Operating Conditions	112
5.4.2	Dynamic Operation with NN Based EBC	114
5.4.3	Robustness of NN-Based EBC Evaluated under Different Grid Events	116
5.5	Summary	118
<b>CHAPTER 6. Model Predictive Control of the MARS</b>		<b>120</b>
6.1	Nonlinear Model of the MARS	120
6.2	Mathematical Modelling	126
6.2.1	Predictive Model of the MMC	127
6.2.2	Cost Function Minimization	128
6.2.3	CVBC	131
6.3	Performance Evaluation	132
6.3.1	Steady-State Performance	132
6.3.2	Dynamic Performance	134
6.3.3	Robustness Performance Analysis	137
6.4	Summary	141
<b>CHAPTER 7. Conclusion and Future work</b>		<b>143</b>

<b>7.1</b>	<b>Conclusion</b>	<b>143</b>
<b>7.2</b>	<b>Contributions</b>	<b>148</b>
<b>7.3</b>	<b>Future Work</b>	<b>150</b>
<b>APPENDIX A. DESCRIPTION OF DEFAULT SUBHEADING SCHEME</b>		<b>152</b>
<b>A.1</b>	<b>PV SM dc-dc Control</b>	<b>152</b>
<b>A.2</b>	<b>ESS SM dc-dc Control</b>	<b>155</b>
<b>APPENDIX B. Standard Compliance of the MARS</b>		<b>160</b>
<b>B.1</b>	<b>IEEE 1547-2018. PRC-024-3 compliance for voltage, and frequency support under defined disturbances</b>	<b>162</b>
<b>B.2</b>	<b>Harmonics Compliance with IEEE 519-2014</b>	<b>164</b>
<b>B.3</b>	<b>Harmonics Compliance with NERC PRC-024-3</b>	<b>165</b>
<b>REFERENCES</b>		<b>168</b>

## LIST OF TABLES

<b>Table 2.1 – Operating modes of SMs .....</b>	<b>23</b>
<b>Table 2.2 – Pittsburgh MARS system DAB parameters .....</b>	<b>35</b>
<b>Table 2.3 – Pittsburgh MARS system DAB simulation parameters .....</b>	<b>35</b>
<b>Table 3.1 – MARS system parameters.....</b>	<b>54</b>
<b>Table 4.1 – Utilization in real-time simulation .....</b>	<b>73</b>
<b>Table 4.2 – Testing accuracy of the confusion matrix .....</b>	<b>73</b>
<b>Table 4.3 – The MARS system parameters. ....</b>	<b>73</b>
<b>Table 4.4 – Statistics of the data w/wo EBC criteria. ....</b>	<b>76</b>
<b>Table 5.1 – Algorithm 1&amp; 2&amp; 3: Power mismatch elimination algorithm .....</b>	<b>92</b>
<b>Table 5.2 – Utilization in real-time simulation.....</b>	<b>100</b>
<b>Table 5.3 – Testing accuracy of the confusion matrix .....</b>	<b>100</b>
<b>Table 5.4 – Comparison of the EBC controller performance .....</b>	<b>101</b>
<b>Table 7.1 – Comparison of different control strategies. ....</b>	<b>147</b>

## LIST OF FIGURES

<b>Figure 1.1 – MARS circuit architecture. ....</b>	<b>7</b>
<b>Figure 1.2 – Capacitor voltages of all SMs in the upper arm phase A. The nominal voltage of the SM capacitor voltage is 1600V.....</b>	<b>9</b>
<b>Figure 1.3 – Output grid current of the MARS while power mismatch exists in the system. ....</b>	<b>10</b>
<b>Figure 2.1 – The reduced-order model. ....</b>	<b>24</b>
<b>Figure 2.2 – Circuit diagram of MARS DAB with front-end half-bridge in a PV SM. ....</b>	<b>28</b>
<b>Figure 2.3 – Circuit diagram of MARS dc-dc converters with front-end half-bridge in a ESS SM. ....</b>	<b>29</b>
<b>Figure 2.4 – Hysteresis relaxation applied to isolated PV DAB inductor currents' dynamics during blocked state. ....</b>	<b>31</b>
<b>Figure 2.5 – Comparison of the simulation results for the proposed algorithm and reference model. ....</b>	<b>37</b>
<b>Figure 2.6 – Comparison of the simulation results for the proposed algorithm and reference model. ....</b>	<b>38</b>
<b>Figure 2.7 – Transformer current and PV-side capacitor voltage waveforms for the proposed algorithm. ....</b>	<b>38</b>
<b>Figure 2.8 – Transformer current and PV-side capacitor voltage waveforms for the proposed algorithm. ....</b>	<b>39</b>
<b>Figure 3.1 – Hierarchical control system to control the MARS. ....</b>	<b>41</b>
<b>Figure 3.2 – Block Diagram of L1 and L2 controllers.....</b>	<b>42</b>
<b>Figure 3.3 – Control block diagram of qd current controller.....</b>	<b>43</b>
<b>Figure 3.4 – Control block diagram of ac components of the circulating current....</b>	<b>44</b>
<b>Figure 3.5 – Control block diagram of the ac components of the circulating current. ....</b>	<b>45</b>
<b>Figure 3.6 – The EBC of the MARS.....</b>	<b>50</b>
<b>Figure 3.7 – Block diagram of L2 controller. ....</b>	<b>51</b>
<b>Figure 3.8 – Upper arm phase A capacitor voltages under the operating point of <math>P_{dc} = -30\text{MW}</math>, <math>P_{ac} = 100\text{MW}</math>, <math>P_{pv} = 100\text{MW}</math>, <math>P_{ess} = 30\text{MW}</math> (a) With the MARS current control, and (b) Without the MARS current control.....</b>	<b>53</b>
<b>Figure 3.9 – MARS grid-side measured three-phase voltages and currents, active and reactive powers, and dc current. ....</b>	<b>56</b>
<b>Figure 3.10 – Capacitor voltages in representative SMs subsequent to changes in the operating condition. ....</b>	<b>56</b>
<b>Figure 3.11 – One PV and ESS converter outputs.....</b>	<b>56</b>
<b>Figure 3.12 – The MARS grid-side measured three-phase voltages and currents, active and reactive powers. ....</b>	<b>57</b>
<b>Figure 3.13 – The MARS grid-side measured three-phase voltages and currents, active and reactive powers. ....</b>	<b>58</b>
<b>Figure 3.14 – Ac-side grid frequency. ....</b>	<b>59</b>

Figure 3.15 – The MARS grid-side measured three-phase voltages and currents, and active and reactive powers. ....	59
Figure 3.16 – Capacitor voltages in the representative SMs subsequent to changes in the operating condition.....	60
Figure 4.1 – Block Diagram of L1 and L2 controllers with EBC criteria. ....	65
Figure 4.2 – Ratio of stable operating conditions and unstable operating conditions vs sorting frequency of capacitor voltage balancing algorithm.....	66
Figure 4.3 – Visualization of the stability for all 6158 operating conditions. ....	68
Figure 4.4 – Random Forest algorithm.....	69
Figure 4.5 – Feature importance. ....	70
Figure 4.6 – Diagram of ANN algorithm. ....	71
Figure 4.7 – Confusion matrix of ANN training. ....	71
Figure 4.8 – (a) Ploss reduction percentage for 1104 operating conditions (b) The average frequency reduction percentage for 1104 operating conditions. ....	76
Figure 4.9 – Diagram for cHIL system setup. ....	77
Figure 4.10 – Connection set up for OP4510 and OP5707 (a) Front-side connection; (b) Back-side connection.....	78
Figure 4.11 – Capacitor voltages in representative SMs subsequent to changes in the EBC criteria; ESS and PV side capacitor voltages and inductor current under three operating conditions in which capacitor voltage balancing cannot be maintained without the EBC. (a) $P_{ac}=100$ $P_{dc}=60$ $Q_{ac}=0$ ; (b) $P_{ac}=-100$ $P_{dc}=-170$ $Q_{ac}=0$ ; (c) $P_{ac}=-150$ $P_{dc}=-220$ $Q_{ac}=50$ . ....	80
Figure 4.12 – (a) The MARS grid-side measured three-phase voltages and currents, active and reactive powers, and dc current. (b) Capacitor voltages in representative SMs subsequent to changes in operating condition; one PV and ESS converter outputs.....	82
Figure 4.13 – The MARS grid-side measured active and reactive powers, dc power, and capacitor voltages of different types of SMs. ....	83
Figure 4.14 – The MARS grid-side measured active and reactive powers, dc power, and capacitor voltages of different types of SMs. ....	84
Figure 5.1 – L1 controller diagram with NN EBC.....	88
Figure 5.2 – Flowchart to evaluate the power reference of the dc power, PV and ESS power. ....	92
Figure 5.3 – Data acquisition process.....	97
Figure 5.4 – Diagram of ANN algorithm. ....	97
Figure 5.5 – The architecture of NARX NN. ....	98
Figure 5.6 – Learning curve of ANN model. ....	99
Figure 5.7 – Learning curve of NARX model.....	99
Figure 5.8 – Response to arm power mismatch under SPA mode: active power measured at grid side, grid side current, circulating current, capacitor voltage, and inductance current at PV side of random PV SMS in the upper arm of three phases. ....	104
Figure 5.9 – Response to arm power mismatch under SPA mode: the capacitor voltages of three phases Normal, PV, and ESS SM in upper arm phase A without NN-based EBC. ....	105

<b>Figure 5.10 – Response to arm power mismatch under SPA mode: the capacitor voltages of three phases Normal, PV, and ESS SM in upper arm phase A with NN-based EBC.....</b>	<b>105</b>
<b>Figure 5.11 – Response to the arm power mismatch: active power measured at the grid side, grid-side current, circulating current, capacitor voltages, and inductor current at the PV side of random PV SMs in the upper arm of the three phases. .</b>	<b>106</b>
<b>Figure 5.12 – Response to the arm power mismatch under fixed Pac mode: the capacitor voltages of the three-phase normal, PV, and ESS SMs in the upper arm phase a without the NN-based EBC. ....</b>	<b>107</b>
<b>Figure 5.13 – Response to the arm power mismatch under fixed Pdc mode: the capacitor voltages of the three-phase normal, PV, and ESS SMs in the upper arm phase a without the NN-based EBC. ....</b>	<b>107</b>
<b>Figure 5.14 – Response to the phase power mismatch under SPA mode: active power measured at grid side, grid side current, circulating current, capacitor voltage, and inductance current at PV side of random PV SMS in the upper arm of three phases. ....</b>	<b>109</b>
<b>Figure 5.15 – Response to the phase power mismatch under SPA mode: the capacitor voltages of three phases Normal, PV, and ESS SM in upper arm phase A without NN-based EBC. ....</b>	<b>110</b>
<b>Figure 5.16 – Response to the phase power mismatch under SPA mode: the capacitor voltages of three phases Normal, PV, and ESS SM in upper arm phase A with NN-based EBC.....</b>	<b>110</b>
<b>Figure 5.17 – Response to the phase power mismatch under fixed Pdc mode: active power measured at grid side, grid side current, circulating current, capacitor voltage, and inductance current at PV side of random PV SMS in the upper arm of three phases. ....</b>	<b>111</b>
<b>Figure 5.18 – Response to the phase power mismatch under fixed Pac mode: the capacitor voltages of the three-phase normal, PV, and ESS SMs in the upper arm phase a without the NN-based EBC. ....</b>	<b>112</b>
<b>Figure 5.19 – Response to the phase power mismatch under fixed Pac mode: the capacitor voltages of the three-phase normal, PV, and ESS SMs in the upper arm phase a without the NN-based EBC. ....</b>	<b>112</b>
<b>Figure 5.20 – SM capacitor voltages; ESS, PV capacitor voltages and inductor current under operating condition which capacitor voltage balancing cannot be maintained without the EBC. <math>Pac=100MW</math> <math>Pdc=60MW</math> <math>Qac=50</math> MVar.....</b>	<b>114</b>
<b>Figure 5.21 – SM capacitor voltages; ESS, PV capacitor voltages and inductor current under operating condition which capacitor voltage balancing cannot be maintained without the EBC. <math>Pac=-100MW</math> <math>Pdc=-170MW</math> <math>Qac=0</math>. ....</b>	<b>114</b>
<b>Figure 5.22 – The MARS grid-side measured three-phase currents, active and reactive powers, dc current, capacitor voltages in representative SMs subsequent to changes in operating condition .....</b>	<b>115</b>
<b>Figure 5.23 – The MARS L1 cHIL test results: ac-side grid frequency, capacitor voltages of different types of SM during loss of generation event.....</b>	<b>116</b>
<b>Figure 5.24 – The MARS L1 cHIL test results: ac-side current, voltage, capacitor voltages of different types of SM during three-phase to ground fault.....</b>	<b>117</b>

Figure 5.25 – The MARS L1 cHIL test results: ac-side current, voltage, capacitor voltages of different types of SM during a line-to-line phase fault event. ....	117
Figure 6.1 – Schematic diagram of one arm of the MARS .....	122
Figure 6.2 – Schematic diagram of the proposed MPC method.....	132
Figure 6.3 – (a)The MARS grid-side measured three-phase voltages. (b) The MARS grid-side measured three-phase currents and circulating currents. ....	133
Figure 6.4 – (a)The MARS grid-side active and reactive powers. (b) Capacitor voltages in representative SMs. ....	133
Figure 6.5 – (a)The MARS grid-side measured three-phase voltage under various operating conditions. (b) The MARS grid-side measured three-phase currents and circulating current under various operating conditions. ....	135
Figure 6.6 – (a)The MARS grid-side active and reactive powers under various operating conditions. (b) Capacitor voltages in representative SMs under various operating conditions.....	135
Figure 6.7 – One PV and ESS converter outputs.....	135
Figure 6.8 – (a) THD of grid side current during change of the reference power : $P_{ac}=260\text{MW}$ , $Q_{ac}=0$ , $P_{dc}=260\text{MW}$ to $P_{ac}=100\text{MW}$ , $Q_{ac}=100\text{MVar}$ , $P_{dc}=-10\text{MW}$ ; (b) THD of grid side current during change of the reference power $P_{ac}=100\text{MW}$ , $Q_{ac}=100\text{MVar}$ , $P_{dc}=-10\text{MW}$ to $P_{ac}=-100\text{MW}$ , $Q_{ac}=0$ , $P_{dc}=-230\text{MW}$ .....	137
Figure 6.9 – The MARS grid-side measured three-phase voltages and currents under three-phase to ground fault.....	138
Figure 6.10 – The MARS grid-side measured three-phase voltages and currents under a line-to-line fault. ....	139
Figure 6.11 – (a)The MARS grid-side measured three-phase voltages and currents under loss of generation event. (b)Ac-side grid frequency.....	139
Figure 6.12 – Capacitor voltages in representative SMs under various operating conditions. ....	140
Figure 6.13 – Comparison of THD ( $ig_{abc}$ ) during grid event with the implementation of the MPC and NN-based EBC. ....	141
Figure 7.1 – Comparison of different control strategies regarding the system loss and the system dynamics. ....	146
Figure A.1 – Block diagram of L3 PV controller.....	155
Figure A.2 – Block diagram of L3 ESS controller. ....	159
Figure B.1 – PE-HIL setup to evaluate hierarchical control system of the MARS. ....	162
Figure B.2 – The open loop MARS PE-HIL test layout. ....	162
Figure B.3 – Voltage ride-through requirements for IEEE 1547 2018 and duration for MARS at Pittsburg providing voltage support during balanced three-phase fault and unbalanced line-to-line fault.....	163
Figure B.4 – Frequency protection setting for PRC-024-3 and preliminary characterization of MARS at Pittsburg based on fast frequency response provided by MARS during 804.4 MW loss of generation. ....	164
Figure B.5 – Harmonics compliance for cHIL test: (a) TDD for grid current. (b)instantaneous grid current. ....	165
Figure B.6 – Change in frequency tested at the western off normal frequency capability curve. ....	166



**Figure B.7 – Change in PCC voltage tested at the voltage ride-through time  
duration curve. .... 167**

## SUMMARY

Today's electric power systems are transitioning towards low-carbon grids with an increased penetration level of renewable energy resources. Large-scale photovoltaic (PV) systems are amongst the fast-growing, non-traditional sources in the grid. However, the intermittent nature of PV power poses challenges in the power system with output power fluctuation. Coupling the PV power with an energy storage system (ESS) has been a well-established approach to address those challenges. The multi-port autonomous reconfigurable solar power plant (MARS), which is an integrated concept for integration of PV and ESS to the transmission ac grid and a high-voltage direct current (HVdc) link, is designed to provide frequency response and reject disturbances in the grid with continued operation and reduced transient instability. In the MARS system, various input power sources are connected to the submodules (SMs) through dc-dc converters. However, the presence of different sources such as PV and ESS in each arm of the MARS causes uneven distribution of active power among different SMs present in MARS, thereby leading to capacitor voltage disparity and may impact system stability under various operating conditions. Moreover, in the case of partial shadings, shaded PV SMs will suffer from decreased injected PV power, causing power mismatch within different SMs in the MARS system. Therefore, the main goal of this thesis is to propose advanced control methods applicable to the MARS and MARS-type systems to address the aforementioned challenges and achieve better performance.

In this thesis, an energy balancing control (EBC) method is introduced to balance the capacitor voltages of different types of SMs. Moreover, the machine learning (ML)-

based EBC criteria are proposed to improve the system efficiency and reduce the switching frequency. The proposed EBC criteria can disable/enable the EBC depending on the MARS input power dispatch commands with high accuracy. The PI-based EBC combined with ML-based EBC criteria solves the capacitor voltage disparity problem with improved system efficiency.

Afterward, a neural network-based power mismatch elimination (NNPME) strategy is proposed to (i) address the power mismatch between the arms and phases, (ii) further reduce the simulation design complexity, and (iii) increase the efficiency of the system. The proposed NNPME strategy employs ESS to its maximum capacity and the dc and ac circulating currents to transfer power between the SMs, arms, and legs of the MARS system.

As none of the aforementioned ML-based control methods can quantitatively control the capacitor voltages of different types of SMs. A model predictive control (MPC) that can satisfy the required constraints on the input and states is proposed. The challenge of using an MPC for MARS is that assuming all SM capacitor voltages are balanced is not valid. Thus, the complexity in the control of their internal dynamics appears to be one of the main technical challenges. The proposed MPC largely improves the dynamic response of the MARS and further simplifies the control design process.

All three proposed advanced controls facilitate the efficient control and energy management of a system with multiple input power sources like MARS to fully utilize its potential with an extended operating region while maintaining high efficiency.

# **CHAPTER 1. INTRODUCTION**

## **1.1 Motivation and Statement of the Problem**

Renewable energy generation increased by about 7% in 2020 while the demand for all other fuels declined [1]. After it decreased by 4.5% in 2020, the global energy consumption rebounded by 5% in 2021 and is expected to increase in the long run. In the meantime, the continuing expansion of renewable power deployment can be foreseen to meet the net zero emissions by 2050 and to cope with the increasing energy demand.

The global cumulative photovoltaics (PV) capacity is well above 700 GW by 2020. Solar PV, as a promising option for renewable electricity generation and one of the two types of the fastest growing renewable resources, is expected to propel continuing investment in the coming years [2]. PV generation has exceeded 1 000 TWh in 2021. The grid-tied utility-scale installations of PV farms have been the majority of the growth of total installed PV solar power and pose challenges to the grid operators due to the intermittent nature of the PV. Thus, the increasing penetration of PV could potentially affect grid reliability in a negative manner. The energy storage system (ESS) can instantly deliver active power to provide services such as spinning reserve, peak shaving, load leveling, and load frequency control. It can also smooth the stochastic power output of the PV plants and provide the existing and future projected ancillary service products by various balancing authorities and system operators in the U.S. At the end of 2020, there was only 1.5 GW battery storage capacity installed in the U.S., most of which was standalone. However, to address the increased challenges imposed by fast growing variable renewable generation including solar power, 14.5 GW new battery storage capacity has

either become online or been planned to be online from 2021 to 2024 [3]. The majority of these battery energy storage systems, roughly 63%, are co-located or will be co-located with PV farms. For instance, the Lily solar-plus-storage project started to operate in Texas in December 2021, which has 181 MW solar PV and 55 MW battery storage; this hybrid plant is estimated to produce 367 GWh green electricity and reduce 242,000 tons of carbon dioxide (CO<sub>2</sub>) emissions per year [4].

The hybrid power plant in which PV and ESS are collocated and share a point of common coupling is getting more and more attention, and an efficient ac-dc (and dc-ac) power converter is desired as the interface between the electrical grid and the renewable energy sources. The modular multilevel converter (MMC) has been a promising option for integrating renewable power plants and hybrid plants into the grid. The main advantage of the MMC is, compared to other competing technologies, the modular structure that allows MMC to be easily scaled up into a large-scale converter, thus eliminating the need for bulky line transformers since they can reach medium- and high-voltage levels owing to their multilevel output voltage [5][6]. The MMC has low grid-side current harmonics and fewer ac filtering requirements [7]. Moreover, the MMC can provide lower power losses due to the lower switching frequency of the switching devices [8]. The production cost is reduced since it features a modular design based on identical submodules (SMs) [9]. These merits have made the MMC a potential solution for grid integration of renewable energy resources. The drawback of the MMC is its control complexity which stems from the high number of switching devices [10].

Proper operation of the MMC necessitates a strategy to eliminate or minimize its circulating currents. However, this challenge has been addressed nowadays using different

control methods. Controlling the circulating current based on proportional-integral (PI) controller in dq reference frame and tuning the proportional resonant (PR) and repetitive controllers to suppress the even harmonics of the circulating current are the most commonly used methods in the literature [11]-[14].

In addition to the above-mentioned issues, one of the major challenges associated with the control of MMCs is maintaining the SM capacitor voltages at their nominal values. Different control methods have been proposed in the literature to address this challenge. Balanced capacitor voltages are commonly achieved by sorting algorithms [15][29]; other methods such as averaging and balancing control also exist [16][30][31]. In the averaging and balancing control scheme of MMC, the capacitor voltage of each SM is controlled individually with the control loops. The SM capacitor voltage balancing algorithms proposed in [15] measured the SM capacitor voltages and sorted them within each sampling period. Then, based on the direction of the arm currents and the number of required on-state SMs within each sampling period, a number of SMs are inserted/bypassed. To reduce the switching frequency, the strategy proposed in [17] limits the number of switches changing their state at any instant to the minimum possible value, even lower to only one switch change.

With the capacitor voltage balancing algorithms, the rest of the control of MMC is designed based on the assumption that all capacitor voltages are well balanced, which largely reduces the complexity of the control design. With energy sources integrated to SMs, the capacitor voltage balancing algorithm may not be capable of balancing the SMs. Thus, the control of MMC with distributed energy sources becomes challenging.

The MMC with distributed energy sources has either an asymmetric topology [18] or a symmetric topology [19]-[22]. In [18], an asymmetric circuit structure of the MMC, which has PV integrated with the SMs in the upper arm and ESS integrated with the SMs in the lower arm, is proposed. The asymmetric topology leads to uneven distribution of active power between the arms in each phase and circulating current needs to enforce to balance the inter-arm power mismatch. Since the asymmetric circuit topology suffers from high circulating current and power losses, it is not suitable for systems with large power ratings. The symmetric topology is more common and can be categorized as (i) Topology-a: all SMs are integrated with the same external sources; (ii) Topology-b: SMs in one arm are integrated with different external sources (including normal SMs). Topology-b could be derived from Topology-a, for example: partial shedding happens for MMC with distributed PV; MMC with distributed battery has some cells with faulty battery; the state-of-charge (SoC) of batteries for MMC-based ESS system is unbalanced, etc. For Topology-a, since all SMs are integrated with an identical amount of external power, the control of a traditional MMC can be directly applied. The system of Topology-b, however, has an uneven distribution of active power in one arm. The intra-arm power mismatch may endanger the stable operation of the entire system and requires advanced control.

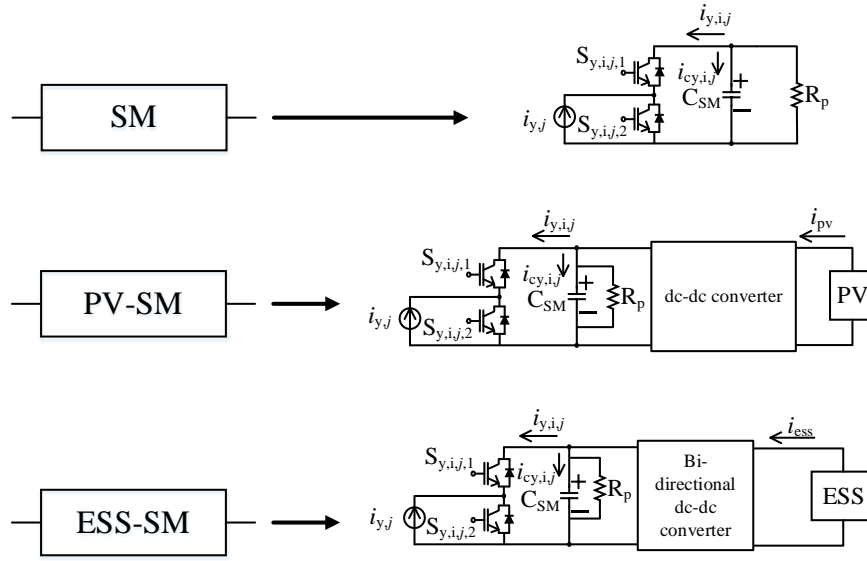
Significant improvement of control quality could be achieved through implementing the model-based control procedures for MMC-based hybrid systems which has multi-input-multi-output (MIMO) processes and inherently non-linear characteristics due to switching. However, such control applications are still not widely implemented because mathematical process models in model-based control could be complicated and expensive to obtain due to the complexity of those processes. The machine learning (ML) algorithms can be

investigated in the control of the MMC based-hybrid system to understand the model through samples. Moreover, the model predictive control (MPC) has the potential to be used to replace the conventional simple multi-loop single-input–single-output (SISO) controllers with the development of powerful processors. The MPC utilized the discrete-time model of the system to predict the future evolution of the system's states over a user-defined prediction horizon. An optimization problem is created with a formulated cost function based on the predicted states and the constraints associated with the states and control variables of the system. The optimization problem is solved for every time step and out of the sequence of control variables, the first control variables in the control horizon will be applied to the system while the rest will be abundant.

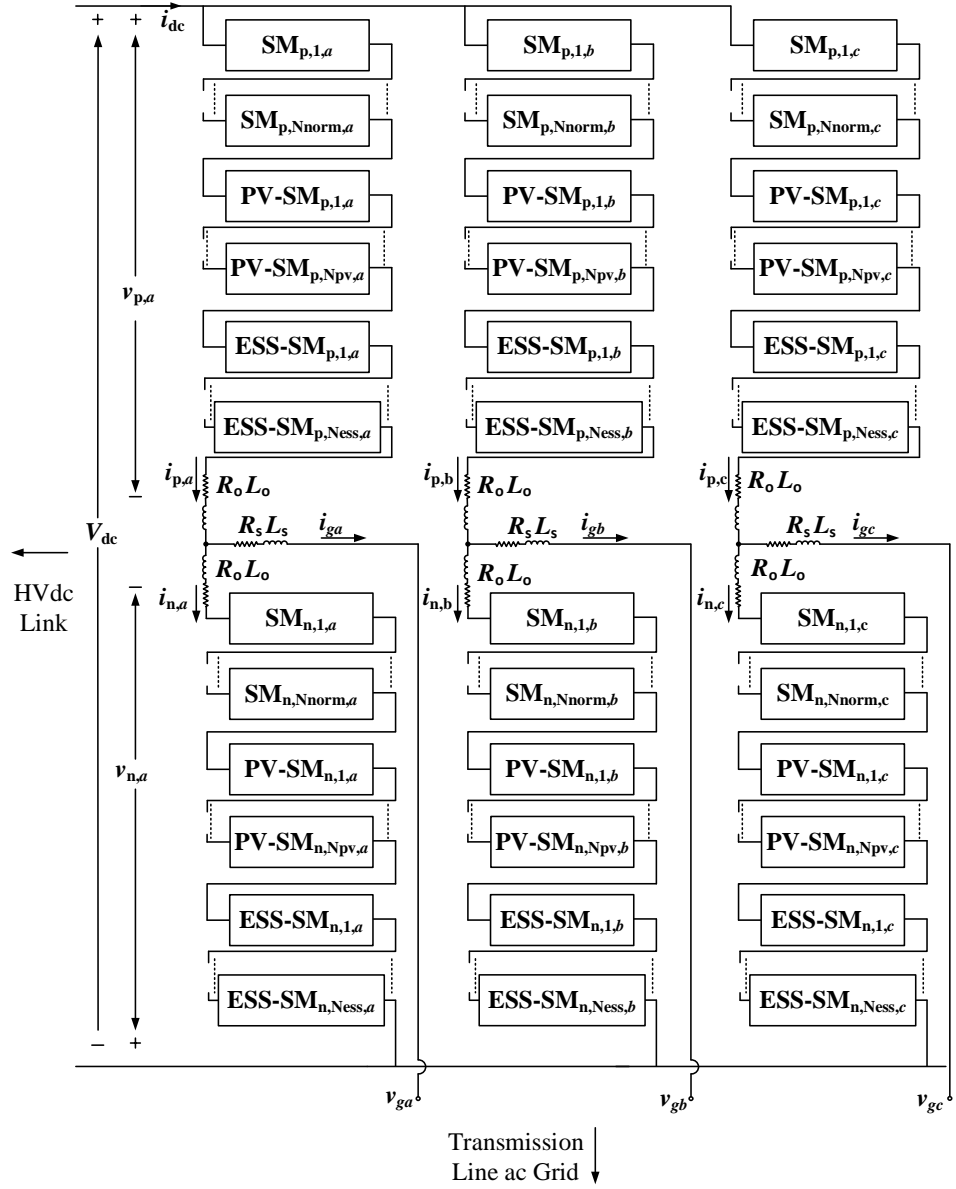
A novel hybrid system called multi-port autonomous reconfigurable solar power plant (MARS) is studied in this dissertation. It provides an attractive alternative to connect PV and ESS to high-voltage direct current (HVdc) links and high-voltage ac grids. Its circuit topology is illustrated in Figure 1.1. The MARS, which is modular and inherently reconfigurable to enable different operating conditions of PV and ESS, overcomes the disadvantages of the discrete development of hybrid PV-ESS plants and HVdc systems with reduced cost, improved efficiency, and enhanced reliability. In addition, it can provide frequency support and boost the system inertia. It consists of two arms in each phase, with the differential of the arms connecting to ac grid and the common-mode connecting to the HVdc link. Each arm consists of series connected submodules (SMs). The SMs in the MARS, according to the external power sources with which the front-end half-bridge is interfaced, are categorized into normal SMs, PV SMs, and ESS SMs. The numbers of normal SMs, PV SMs, and ESS SMs are determined based on the PV and ESS plant size.



The normal SM is a half-bridge converter. The PV SM and ESS SM have a dc-dc converter connecting the half-bridge front-end converter to the PV and ESS, respectively. An isolated dc-dc converter that integrates PV panel with the front-end half-bridge of the PV SM is preferred for high voltage applications according to the insulation requirement of the PV system. Note that the selection of the dc-dc converter in PV or ESS SM has limited impact on the higher-level control design.



(a) Configurations of normal SM, PV-SM, and ESS-SM.



(b) Overview of the circuit topology of MARS.

**Figure 1.1 – MARS circuit architecture.**

## 1.2 Objective of the Research

The main target of this Ph.D. thesis is to design and study the control of MARS and to examine and extend its stable operation region. In addition, the thesis will widen the

knowledge of the advanced control strategies of the MMC-based hybrid systems and achieve better system performance. A PI-based energy balancing control (EBC) and the ML-based EBC criteria is implemented to balance the SM capacitor voltage of different types of SMs. To simplify the design process of the PI-based EBC and achieve better system efficiency, an NN-based EBC is proposed. In the meantime, an MPC method to control the MARS system with fast dynamic response, low total harmonic distortion (THD) of grid side current, and maintaining capacitor voltage with the optimization constraint is developed.

In the MARS system, the power from PV panels and ESS units is delivered directly to the SMs rather than being injected into a common dc link. Thus, for each arm, this topology suffers from inter-SMs power mismatch since three types of SMs exist in one arm including the normal SMs, PV SMs, and ESS SMs. The details of the SMs can be observed in Figure 1.1. Figure 1.2 shows the illustrative SMs capacitor voltages measured from all 250 normal SMs, PV SMs, and ESS SMs in phase A upper arm under the operating condition:  $P_{dc} = 60\text{MW}$ ,  $P_{ac} = 100\text{MW}$ , and  $Q_{ac} = 0$ . The capacitor voltages shown in Figure 1.2 are not balanced, causing instability in the ESS system since the capacitor voltage of ESS SMs lies below the capacitor voltage limit.

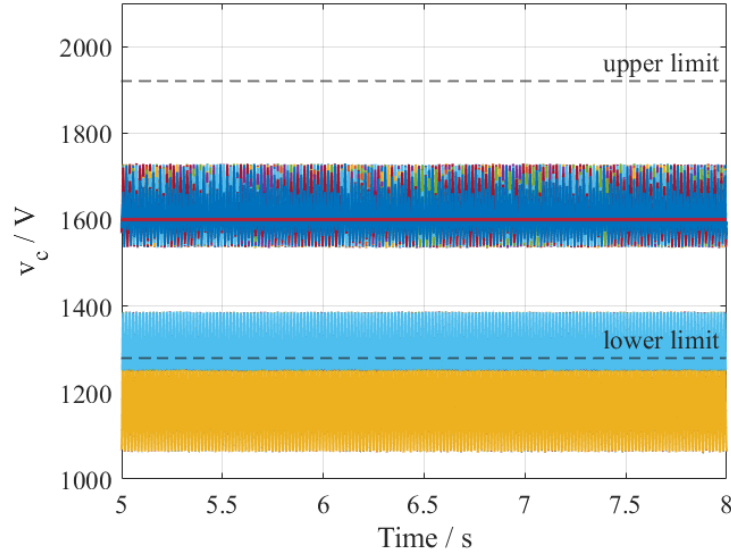


**Figure 1.2 – Capacitor voltages of all SMs in the upper arm phase A. The nominal voltage of the SM capacitor voltage is 1600V.**

In addition to the inter-SM power mismatch, inter-arm power mismatch or inter-phase power mismatch exists when partial shading affects the maximum power output of the PV panels, meaning that the aggregated power injected into the arms of each phase is not equal, or the aggregated power injected into the legs of the system are not equal. The system may inject unbalanced currents into the power system and fail to comply with the grid codes according to the IEEE Std 1547.2-2008 when any of the inter-arm or inter-phase power mismatches occur in the MARS system. Moreover, the IEEE Std 1547-2018 further required the distributed generation units to provide voltage regulation through reactive power exchange with the grid. Figure 1.3 shows illustrative three-phase output currents of the MMC-based PV system while power mismatches exist in the structure of the converter. The output currents are not balanced, and the magnitude of each phase current is different depending on the power injected into the grid from the corresponding phase.

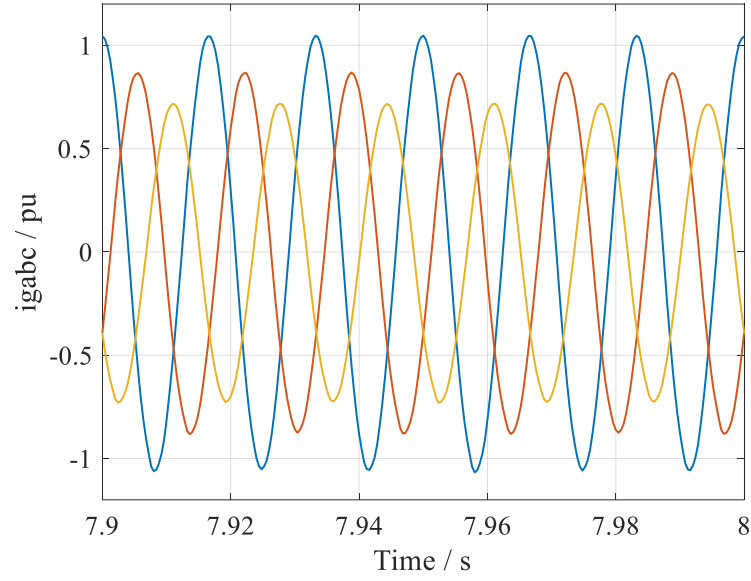


**Figure 1.3 – Output grid current of the MARS while power mismatch exists in the system.**

**The objectives of this work can be divided into the followings:**

1. Introduce a control method to maintain power balance among all types of SMs of the MARS with distributed PV and ESS so that capacitor voltage can be balanced under all operating conditions.
2. Design a power mismatch elimination strategy for the MARS system that extracts the maximum possible power from the PV generators, fully uses the ESS, and injects balanced currents into the power grid despite the presence of power mismatches in the structure of MARS.
3. Develop an ML-based method to avoid unnecessary injection of the fundamental circulating current to reduce the system loss and increase the system efficiency.
4. Employ machine learning algorithms in control designed for addressing the inter-SM power mismatch problem.

5. Design an MPC applicable to the MMC-based hybrid system like MARS to optimize the performance of the control systems implemented to control MARS systems.
6. Construct and develop software and control hardware in the loop (cHIL) to operate an experimental MARS system to verify the proposed theories.

### **1.3 Literature Survey Pertinent to the Thesis Objectives**

#### *1.3.1 ML-Based EBC Criteria of the MARS*

A number of papers aim at studying the operation and control of integrating energy sources into the grid utilizing the MMC topology. References [20][24][25] introduce the control of an MMC integrated with PV units. References [24][25] utilize individual control for each SM, which increases the complexity of an MMC with a large number of SMs. A power mismatch elimination strategy is proposed in [20] to deal with unevenly distributed power in the MMC under the conditions of partial shading of PV units or faulty cells. This strategy utilizes dc and ac circulating currents to balance the inter-arm and inter-phase power. There have been a number of papers discussing the presence of both normal and ESS SMs in an MMC-based ESS system [21], [26]-[28]. The presence of normal SMs is caused by various conditions, including faulty battery units for some of the SMs [21], recycled battery units [26], or the existence of redundant SMs [27]. Having different types of SMs in one arm will lead to uneven distribution of intra-arms active power under some operating conditions. For the general MMC topologies, balanced capacitor voltages are generally achieved by methods based on sorting algorithms. However, the existing capacitor voltage balancing algorithms have their operational limits and do not guarantee

proper operation of the system when there are multiple types of SMs in one arm. The operation boundary of the MMC-based ESS is studied in [21], [26]-[28]. A PQ plot produced by the power balance test is proposed in [21] to identify the stable operating region of the MMC. Similarly, a different practice of the analyzed boundary in the control of the MMC is introduced in [28] through a criteria vector to determine the stable operating conditions from the input of arm voltage, arm current, and SM capacitor voltages. The analytical method to derive the SM power disparity limit introduced in [21], [26]-[28] is not applicable to the MARS system or MMC systems with more than two types of SMs in one arm. In [21] and [28], the power balance test is used to calculate the maximum discharge power from the ESS SMs based on ac-side current and voltage by assuming that the ESS SMs have priority during the sorting process and the sorting frequency is sufficiently fast. The system is considered unstable under the tested operating condition when the maximum discharge power of each ESS SM exceeds its external input power. Such ESS SM power balance test is applied to a range of different operating conditions to obtain the operation boundary of the system. However, when there are more than two types of SMs, the dimension of unknown variables increases while the number of equations remains the same, which in general has no solution. The analysis in [32]-[35] is based on the assumption that the MMC can be decoupled into ac and dc equivalent circuits, which is not suitable for systems using nearest-level control such as the MARS. The capacitor voltage balancing control (CVBC) can heavily impact the stability boundary of the system; however, none of the aforementioned references takes the capacitor voltage balancing algorithm into consideration when enforcing the operating condition limit. The way they use to access the inter-SM active power disparity limit is conservative since they assume

the capacitor voltage balancing algorithm is ideal and can allow one type of SM to charge/discharge at any time when needed.

Control and power management of an MMC with hybrid PV and ESS are rarely discussed in the literature. An MMC-based PV-ESS system presented in [36] aims to smoothen the power generation of PV panels using the ESS. The power mismatch caused by PV is balanced using the ESS and the circulating current when the ESS does not meet the required power. However, the power mismatch between the PV and ESS SMs in one arm is not considered and the designed system is not capable of providing frequency support to the grid.

In this thesis, a novel data-driven method for the analysis of the operating region of the MARS system with multiple types of distributed sources is proposed. In addition, the operating region is extended by an PI-based EBC method, which can deal with capacitor voltage disparity issue and balance the power mismatch in each arm by injecting a fundamental circulating current. The boundary operating conditions are determined and subsequently, the EBC criteria are proposed to mitigate the need for circulating current to increase the system efficiency and reduce the current stress as well as the overall switching frequency. In this thesis, a general analysis and study of the control of MARS are performed and the proposed analysis of the EBC method and the EBC criteria are applied to the MARS system to showcase its efficiency and reliability. Factors affecting the operating region are analyzed and validated using the cHIL tests with the MARS system.

This thesis compares the implementation of the EBC criteria with two different machine learning algorithms: the Random Forest (RF) and artificial neural network (ANN).



The ANN-based approaches are currently growing in the area of power electronics. The design of the neural network (NN)-based controller considers the whole system as a black box and does not require the mathematical model of the system. Thus, the NN-based controller may also be designed with the absence of exact knowledge of the system. Another advantage of the ANN is that the hyperparameter tuning of the shallow network is usually easier than tuning conventional controllers. Pattern recognition is defined as a process of finding regularities and similarities in data using algorithms. The ANN is used here to perform pattern recognition. The training process of the NN involves optimizing the weight of each neuron to create a model that can accurately map the input variables to the output variables from the given training data. In power electronics, the NN has either been used as a system identification method to deal with the nonlinear relationship of the input and output variables or as a control method. Most applications of system identification are in induction motor drives to estimate the rotor speed [37] or rotor flux [38]. Reference [39] maps the input of wind speed and air temperature variations of the wind turbine to optimize rotor speed through a cascade-forward NN instead of solving the complicated dynamics. A few papers involve the NN in MMC applications [40]-[45]. In [40]-[43], NN is implemented to reduce the computational burden associated with the model predictive control of MMC. Reference [44] utilizes NN to improve the efficiency of weight factor tuning. A NN observer for SM capacitor voltage estimation is introduced in [45]. Reference [46] calculates the circulating current reference under unbalanced grid faults by an artificial NN trained to relate the circulating current references and the capacitor voltage ripples.

The RF is one of the most widely used algorithms due to its simplicity and diversity. It is a flexible, easy-to-use machine learning algorithm that reduces overfitting and can provide higher accuracy among most available classification methods, even without hyper-parameter tuning.

### *1.3.2 NN-based EBC of the MARS*

MMC has been used to integrate PV to HVdc links and ESS to HVdc links [47]-[50]. There are limited studies on architectures needed to integrate PV and ESS together to HVdc and transmission ac grid.

One of the challenges associated with the MARS-type architecture comprising both normal SMs and SMs with external power sources is the energy balancing of the capacitor in the SMs. The difference in the power consumed or produced by SMs is referred to as inter-SM power mismatch in this thesis. Inter SM power mismatch shrinks the operating region of the system since capacitor voltage balancing is a vital factor for the safe and sound operation of MARS-type architectures. For MARS-type architectures, the balanced SM capacitor voltage also ensures stable operation of the integrated power sources such as PV and ESS. However, the well-known SM capacitor voltage sorting algorithm has its limitations and fails to control the capacitor voltages in the presence of different types of SMs (with different power sources) in one arm. Reference [28] presents the boundary of operating conditions under which the MMC-based battery energy storage system (BESS) can operate properly; it formulates a criteria vector that is used to determine whether the system can supply the demanded output power. However, the analysis to derive the criteria is conservative and only suitable for systems with one type of external power source.

Additionally, it is not the most optimum means to operate the system. Reference [35] studies the power flow of the MMC with BESS integrated into the SMs and proposed a method to maintain the SM capacitor voltage balancing by injecting dc and circulating currents. Injecting circulating currents has been widely employed in the literature for the MMC-based PV or BESS systems' internal control purposes as it can address operation region extension [51]-[52], reduce SM capacitor voltage ripples [53]-[54], and eliminate inter-phase or inter-arm power mismatch [20][36] without affecting the grid current. However, the presence of the circulating currents leads to increased current stress on the switching components, increased magnitude of the SM capacitor voltage fluctuation, and increased conduction losses. Identifying the optimum circulating current injection needed may improve the operational characteristics. The relationship between the system arm power and the circulating current references is analyzed in [20][35] and [55]. However, the precise relation between the SM capacitor voltage ripples and circulating current is not discussed. The stability of the PI-based control in [20][35] and [55] cannot be guaranteed since the theoretical foundation set is not sufficient to explicitly derive circulating current references for controlling three-phase SM capacitor voltage ripples. In addition, for the multi-objective optimization problems, where minimizing circulating current and capacitor voltage ripples are conducted simultaneously, PI-based control with fixed gains cannot adaptively control the magnitude of the injected circulating current under different operating conditions. A new control method for balancing the energy in different SM capacitors needs to be designed.

The second challenge is the unequal aggregated power generated by the external sources injected into the arms of the MARS-type system, referred to as inter-arm or inter-

phase power mismatch in this thesis. It can violate the limitation of current distortion imposed in the IEEE 1547 [23] by injecting unbalanced currents into the grid. Reference [24] proposed a method for adjusting the phase voltage of the MMC-based PV system to balance the grid current during unequal PV power outputs. The method, with limited capability of eliminating mismatched power, lacks a mathematical basis to justify the stability and effectiveness of the designed parameters. Moreover, it cannot deal with inter-arm power mismatch. Authors of [19]-[20] and [36] study the power mismatch between arms and phases. In [19], a redundant module to compensate for the fluctuation voltage of PV SM caused by partial shading is designed. The work [19] improves the output power quality to the grid under partial shading by controlling the PV SMs individually, which is not suitable for a system with a large number of SMs. Reference [20] eliminated the power mismatches in the MMC PV-based system by continuously injecting circulating current; however, the additional power loss associated with the continual injection of circulating current is a drawback. Reference [24] improved the injected circulating current by adjusting the terminal voltage of the MMC-based PV system with the presence of power mismatch. Not many papers discussed the MARS-type architecture that incorporates two or more external power sources integrated with the SMs. Authors of [36] analyzed the control to eliminate power mismatch in a hybrid MMC-based PV and BESS. They employed ESS system, dc, and ac circulating current to compensate for the power mismatch between arms and legs; however, inter-SM power mismatch is not discussed and the system efficiency reduction due to the injected circulating current is not considered.

### *1.3.3 MPC of the MARS*

MMCs are multiple-input-multiple-output (MIMO) nonlinear systems since the physically interconnected SMs have nonlinear and discontinuous dynamics due to switching. Various control strategies including the conventional proportional-integral (PI) controllers [29], the sum of squares decomposition method [56], repetitive control [57], proportional resonant control [58], and model predictive control [59]-[69] have been proposed and investigated.

Renewable energy generation and energy storage systems have been growing at a fast pace in the last decade. More and more literature investigated the control of MMC-based PV, MMC-based ESS, or hybrid MMC and PV. Most of them used conventional PI control or PR control, Hierarchical PI SISO control schemes are well-established control solutions for these systems but are quite limited in performance. Moreover, the external sources connect to the MMC SMs increase the complexity of the control to a certain limit. Model predictive control shows its superior in significantly improving the dynamic response of the system and controllability through including the nonlinearity of the MMC's dynamic in the control. In addition, it is robust to the variation of system parameters, and the constraints to the input and state can be strictly achieved. Despite the advances made in MPC, to the best knowledge of the authors, there is no literature using the MPC for an MMC-based PV or ESS system with normal SM and PV/ESS SM in each arm, not to mention the MMC systems with SM integrated with multiple sources.

The multi-objective control of the MARS is realized using a hierarchical control structure consisting of 3 control levels as discussed in chapter 3. The L1 and L3 controllers rely on cascaded PI-based control while the L2 controller is implemented by CVBC. One of the main technical challenges associated with the control of the MARS is to

simultaneously maintain the SM capacitor voltages balanced and minimize the circulating currents flowing through the three phases of the converter. The uneven distribution of active power in one arm due to the external sources connected to the SM leads to capacitor voltage disparity even with the capacitor voltage balancing algorithm. The unbalanced capacitor voltages make the traditional cascaded control inefficient since the cascaded control is designed based on the assumption that all capacitor voltages are balanced. The EBC, which acts as a remedial measure, and is proposed in chapter 3, chapter 4, and chapter 5. It maintains the SM capacitor voltages at their nominal values and ensures proper operation of the MARS through injecting fundamental circulating current. Although the classical controllers have been able to control the internal dynamics of the MARS, the nonlinear MIMO dynamics of the MARS with strong coupling among its states necessitates adoption of advanced control strategies. In addition, the lack of a mathematical analysis of the relationship between the capacitor voltage difference and circulating current make the control less efficient. The MPC of the MARS is then proposed in this thesis, which is also applicable to other MARS-type systems.

## **1.4 Thesis Outline**

This thesis consists of seven chapters including the Introduction. The remaining six chapters are outlined as follows:

Chapter 2 introduces the modeling of the MARS. The reduced-order model and the high-fidelity model of the MARS are presented.

Chapter 3 presents each level of the hierarchical control of the MARS as well as the developed EBC control.

Chapter 4 proposes the PI-based EBC combined with the EBC criteria to maintain balanced SM capacitor voltage while increasing the system efficiency. This chapter includes a detailed analytical equation of the capacitor voltage ripple, and develops the system stability boundary through data-driven method and further proposed the ML-based EBC criteria. Different ML algorithms are implemented and compared.

Chapter 5 presents an easier way to implement the EBC which is an NN-based EBC method. The data collection and network training are introduced in this chapter.

Chapter 6 proposes an MPC applicable to the MARS and MARS-type hybrid systems.

Chapter 7 summarizes the thesis and concludes the contributions of the thesis. The future work is also discussed in Chapter 7.

## CHAPTER 2. MODELLING OF THE MARS

The MARS system overcomes the disadvantages of the discrete development of hybrid PV-ESS plants and HVdc systems through reduced cost, increased efficiency, enhanced reliability, among others. MARS can provide frequency support and increase the system inertia. It is also modular and inherently reconfigurable to enable different operating conditions of PV and ESS. The MARS configuration introduced in [70], may incorporate isolation in PV systems, as desired in the location where it is built. The isolation in the PV SM happens through a dual active bridge (DAB) converter.

The challenge in the simulation of a high-fidelity switched system model of the MARS lies in the long simulation time. The long simulation arises from a large number of states present in the MARS that consists of several hundred to thousands of SMs. In addition, the MARS system is numerically stiff, which creates additional computational complexity and requires longer computing time. Increased complexity, further, arises in the DAB converter that usually operates at a frequency in the order of tens of thousands Hz ( $\sim 10\text{kHz}$ ). The controller in the DAB converter requires introducing delays within these switching signals to control the flow of power [71]; very small timesteps such as sub- $1\ \mu\text{s}$  are required to simulate the MARS with isolated PV SMs accurately. The flow of power observed in the simulations of the DAB converter is extremely sensitive to the simulation timestep chosen and the accuracy of the delay represented in the model. The simulation timestep needed to maintain the accuracy is extremely small and usually around 10-100 nanoseconds. In the MARS, the presence of several hundred to thousands of DABs further increases the computational burden imposed. While the average-value model [72] and



discrete-time models [73]-[74] of the DAB have been introduced, they do not represent the detailed switching dynamics that are necessary for evaluating the stability and performance of the hierarchical control system in the MARS (that includes generation of switching signals). These issues necessitate a fast simulation capable of reducing the imposed computational burden to simulate the MARS systems.

The challenge of simulating a large number of states in a MARS and the corresponding simulation algorithm required to reduce the computational burden is explained in [70]. In this thesis, efficient simulation algorithms are proposed to further speed up the simulation of high-fidelity models of MARS and the DAB converter. The proposed simulation algorithms include the hybrid discretization method, relaxation techniques, and the interpolating method. These algorithms reduce the matrix inversion requirements and increase the simulation timestep needed while maintaining the accuracy of the simulation results.

## 2.1 MARS Circuit Architecture

The MARS circuit architecture, as shown in Figure 1.1 (a), consists of three legs with two arms in each leg. Each arm of the MARS is comprised of  $N$  series connected, half-bridge SMs, a series inductor  $L_o$ , and a resistor  $R_o$ . Each half-bridge SM consists of two series connected switches, connected in parallel to a capacitor  $C_{sm}$  and a resistor  $R_p$ . Among the  $N$  SMs in each arm, there are  $N_{normal}$  of normal SMs,  $N_{pv}$  of PV SMs, and  $N_{ess}$  of ESS SMs, with their corresponding circuit topologies shown in Figure 1.1 (b). Depending on the state of the switches  $S_{y,i,j,1}$  and  $S_{y,i,j,2}$ , each SM of the MARS can

provide two voltage levels at its terminal, i.e., zero or the capacitor voltage at the front-end half-bridge SM  $v_{c,y,i,j}$ ,  $\forall y \in (p, n), \forall j \in (a, b, c), \forall i \in [1, N]$ .

Different operating modes of SM- $i$  in arm- $y$  of phase- $j$  and its corresponding switching conditions are presented in the table below.

**Table 2.1 – Operating modes of SMs**

Operating modes	$S_{y,i,j,1}$	$S_{y,i,j,2}$
ON-state or inserted	On	off
OFF-state or bypassed	off	on
Blocked state	off	off

Each of the three types of SMs consists of a silicon (Si) insulated-gate bipolar junction transistor (IGBT)-based front-end half-bridge. Especially, the PV SMs are comprised of a silicon carbide (SiC) metal-oxide semiconductor field-effect transistor (MOSFET)-based unidirectional dc-dc converter that connects to the dc-link of front-end half-bridge. In ESS SMs, the unidirectional dc-dc converter is replaced with a SiC MOSFET-based bidirectional buck-boost converter to interface the ESS system and the dc side of the half-bridge converters. The states present within the MARS include the arm currents, normal SM capacitor voltages, PV SM capacitor voltages, PV SM inductor currents, ESS SM capacitor voltages, and ESS SM inductor currents.

## 2.2 Reduced-Order Model of the MARS

Assuming that the voltage ripple of each SM capacitor is zero, the reduced order model of the system is shown in Figure 2.1. In the reduced order model, both the blocked

state of the switches and the linear conductivity losses are neglected. Since the number of SMs per arm is large, the fluctuation of capacitor voltages is assumed to be 0, and the equivalent arm capacitor voltage is  $C_{arm} = \frac{C}{N}$ . Since the capacitor voltages are assumed to be balanced, the capacitor voltage of each SM is  $v_{c1} = v_{c2} = \dots = \frac{V_{dc}}{2N}$ ,  $V_{dc}$  is the dc side voltage of MARS. The arm voltage can then be represented as:

$$V_{arm} = m \frac{V_{dc}}{2}$$

where m is the modulation index of an arm.

The reduced order model cannot be used to perform the protection study, conductivity losses analysis, or study the capacitor voltage balancing algorithm as it averages each arm to an equivalent switching function model. Nevertheless, it can still be used to study the energy transferred from the ac to the dc side into each arm and the circulating current control.

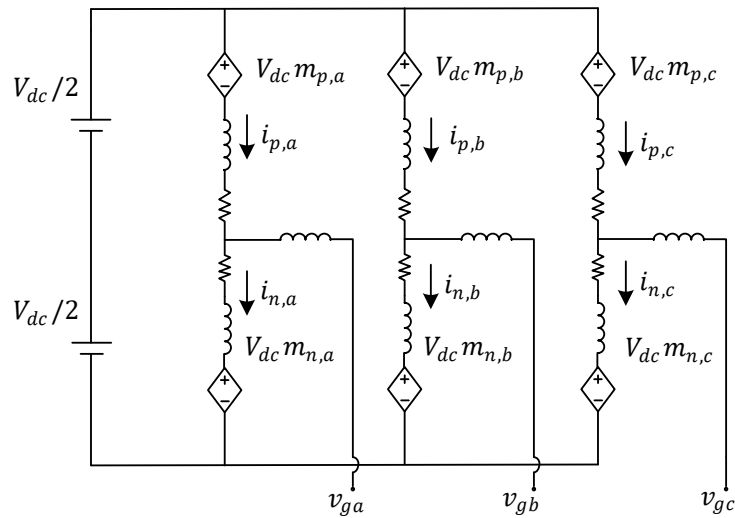


**Figure 2.1 – The reduced-order model.**

### 2.3 High-Fidelity Model of MARS

The differential-algebraic equations (DAEs) that represent the dynamics of the states of each arm are given by (2.1) and (2.2).

$$(L_o + L_s) \frac{di_{p,j}}{dt} - L_s \frac{di_{n,j}}{dt} = -(R_o + R_s)i_{p,j} + R_s i_{n,j} + \frac{V_{dc}}{2} - v_{gj} - v_{cm} - v_{p,j}, \quad (2.1)$$

$$\forall j \in (a, b, c),$$

$$(L_o + L_s) \frac{di_{n,j}}{dt} - L_s \frac{di_{p,j}}{dt} = -(R_o + R_s)i_{n,j} + R_s i_{p,j} + \frac{V_{dc}}{2} + v_{gj} + v_{cm} - v_{n,j}, \quad (2.2)$$

$$\forall j \in (a, b, c)$$

where,

$$v_{y,j} = \sum_{i=1}^{N_{normal}} v_{smnorm,y,i,j} + \sum_{i=N_{normal}+1}^{N_{normal}+N_{pv}} v_{smpv,y,i,j} + \sum_{i=N_{normal}+N_{pv}+1}^N v_{smess,y,i,j}$$

$$\sum_{i=i_x}^{N_x} v_{smx,y,l,j} = \sum_{i=i_x}^{N_x} [S_{y,i,j,1} v_{c,y,i,j} + \{(1 - S_{y,i,j,1})(1 - S_{y,i,j,2})v_{c,y,i,j}\}sgn(i_{y,j})], \forall y \in (p, n), \forall j \in (a, b, c), \forall i \in [1, N]$$

where  $x=norm, pv$  or  $ess$ .  $i_x = 1$  or  $(N_{normal} + 1)$  or  $(N_{normal} + N_{pv} + 1)$  ;  $N_x = N_{normal}$  or  $(N_{normal} + N_{pv})$  or  $N$ .

Blocked state is taken into consideration when implementing the dynamics of MARS as it happens during dead time, dc faults, ac startup charging, and dc startup charging.

### 2.3.1 PV SM

A PV SM with isolation is shown in Figure 2.2. The isolated dc-dc converters in the PV SM in this thesis are considered to be DAB converter. The galvanic isolation provided by the DAB converters enables the grounding of the negative terminals of the PV generators and eliminates the potential induced degradation (PID) phenomenon [76]. In addition, the existing practical implementations of DAB up to 100 kW [77] are also one of the reasons to utilize DAB in the MARS.

The two H-bridge cells of the DAB converter connect the PV arrays and the front-end half-bridge cells together through a high-frequency transformer, as shown in Figure 2.2. A high-frequency transformer with 1:a turns ratio is in between the two H-bridge cells. The leakage inductance and the collective resistance of the transformer are  $L_t$  and  $R_t$ , respectively. All switches are controlled with 50% duty ratio gate signals. To control the power flow of the DAB converter, a delay is introduced between the switching pulses of its two H-bridges by the controller. The delay is calculated within every control time period that may be the same as the switching period. The dynamics of the PV side capacitor voltage ( $v_{dcpv,y,i,j}$ ), transformer currents in PV SM ( $i_{acDAB2,y,i,j}$ ), and front-end half-bridge capacitor voltage ( $v_{cy,i,j}$ ) are given by (2.3), (2.4), and (2.5), respectively.

$$\begin{aligned}
C_{dcpv} \frac{dv_{dcpv,y,i,j}}{dt} &= -\frac{1}{R_{dcpv}} v_{dcpv,y,i,j} + S_2 \times i_{acDAB2,y,i,j} \\
&+ S_{BLDAB2} \times i_{acDAB2,y,i,j} \times \text{sgn1}(i_{acDAB2,y,i,j}) + i_{pv,y,i,j}
\end{aligned} \tag{2.3}$$

$$\begin{aligned}
L_t \frac{di_{acDAB2,y,i,j}}{dt} &= S_1 \times v_{c,y,i,j} + S_{BLDAB1} \times \text{sgn1}(i_{acDAB1,y,i,j}) v_{c,y,i,j} \\
&- a \times S_2 \times v_{dcpv,y,i,j} \\
&- S_{BLDAB2} \times \text{sgn1}(i_{acDAB2,y,i,j}) v_{dcpv,y,i,j} - i_{acDAB2,y,i,j}' \\
&* R_t
\end{aligned} \tag{2.4}$$

$$\begin{aligned}
C_{SM} \frac{dv_{c,y,i,j}}{dt} &= -\frac{v_{c,y,i,j}}{R_p} - i_{acHB,y,i,j} + S_2 \times i_{acDAB2,y,i,j}' \\
&+ S_{BLDAB2} \times i_{acDAB2,y,i,j}' \times \text{sgn1}(i_{acDAB2,y,i,j}')
\end{aligned} \tag{2.5}$$

where,

$$S_1 = S_{y,i,j,13} \times S_{y,i,j,12} - S_{y,i,j,14} \times S_{y,i,j,11}$$

$$S_2 = S_{y,i,j,23} \times S_{y,i,j,22} - S_{y,i,j,24} \times S_{y,i,j,21}$$

$$S_{BLDAB1} = (1 - S_{y,i,j,11})(1 - S_{y,i,j,12})(1 - S_{y,i,j,13})(1 - S_{y,i,j,14})$$

$$S_{BLDAB2} = (1 - S_{y,i,j,21})(1 - S_{y,i,j,22})(1 - S_{y,i,j,23})(1 - S_{y,i,j,24})$$

$$i_{acHB,y,i,j} = S_{y,i,j,1}i_{y,j} + (1 - S_{y,i,j,1})(1 - S_{y,i,j,2})sgn(i_{y,j})i_{y,j}$$

$$i_{acDAB2,y,i,j}' = \frac{i_{acDAB2,y,i,j}}{a}$$

$$sgn1(x) = \begin{cases} -1 & \text{if } x < 0 \\ 1 & \text{if } x > 0 \end{cases}; \forall y \in (p,n), \forall j \in (a,b,c), \forall i \in [1,N]$$

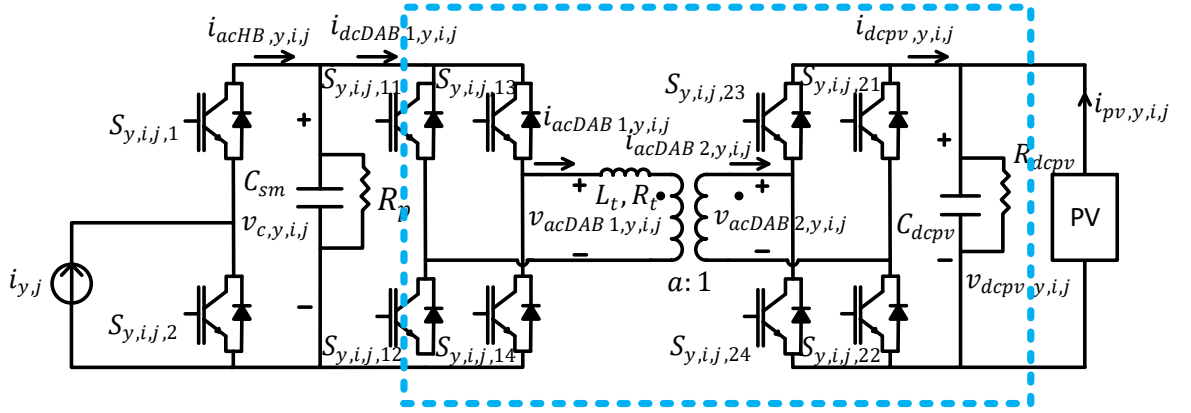


**Figure 2.2 – Circuit diagram of MARS DAB with front-end half-bridge in a PV SM.**

### 2.3.2 ESS SM

The dynamics of the ESS side capacitor voltage, inductor current, and the SM side capacitor voltage are given by (2.6), (2.7), and (2.8), respectively.

$$C_{ess} \frac{dv_{cess,y,i,j}}{dt} = i_{ess,y,i,j} - i_{Less,y,i,j} \quad (2.6)$$

$$L_{ess} \frac{di_{Less,y,i,j}}{dt} = v_{cess,y,i,j} - S_{y,i,j,14}(1 - S_{y,i,j,13}) \times v_{c,y,i,j} - (1 - S_{y,i,j,13})(1 - S_{y,i,j,14})v_{c,y,i,j}sgn(i_{Less,y,i,j}) \quad (2.7)$$

$$C_{SM} \frac{dv_{c,y,i,j}}{dt} = -\frac{v_{c,y,i,j}}{R_p} - i_{y,i,j} + S_{y,i,j,14}(1 - S_{y,i,j,13}) \times i_{Less,y,i,j} + (1 - S_{y,i,j,13})(1 - S_{y,i,j,14})i_{Less,y,i,j} \text{sgn}(i_{Less,y,i,j}) \quad (2.8)$$

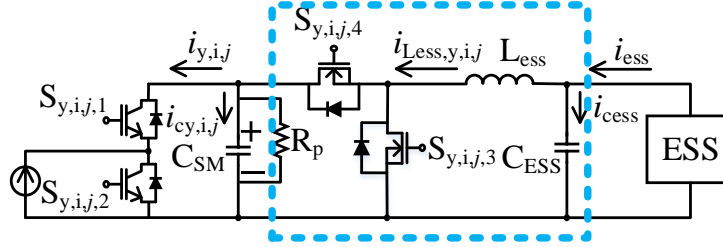


**Figure 2.3 – Circuit diagram of MARS dc-dc converters with front-end half-bridge in a ESS SM.**

### 2.3.3 Normal SM

The dynamics of the normal SM capacitor voltages in MARS are given by

$$C_{SM} \frac{dv_{c,y,i,j}}{dt} = -\frac{v_{c,y,i,j}}{R_p} + S_{y,i,j,1} i_{y,j} + (1 - S_{y,i,j,1})(1 - S_{y,i,j,2}) i_{y,j} \text{sgn}(i_{y,j}) \quad (2.9)$$

## 2.4 Simulation Algorithms

A fast electromagnetic transient (EMT) simulation algorithm to simulate the detailed switched system model of MARS with the isolated PV SM is presented in this section. The simulation algorithms for MARS are studied in [78] and the detailed DAEs representing the dynamics of PV inductor current, PV side capacitor voltage, ESS inductor current, and ESS side capacitor voltage are discussed in [78]. Enhancements to simulation of DAB are considered here and incorporated into the MARS simulation model. Due to the  $\text{sgn1}$  function being presented in the dynamics of the isolated PV SM's transformer current,



there is numerical stiffness in the DAEs representing the dynamics of the PV SM's transformer current. The DAEs representing the dynamics of the other states (capacitor voltages) in the isolated PV SM are non-stiff. Based on the stiffness identified, a hybrid discretization algorithm is applied.

#### 2.4.1 Hybrid Discretization

The non-stiff DAEs representing the capacitor voltage dynamics of the isolated PV SM are discretized using forward Euler based discretization, which is an explicit method. The backward Euler discretization is used to discretize stiff DAEs representing the dynamics of the DAB transformer current, which enables stable simulation with larger simulation timesteps. As proved in [75], the hybrid discretization is stable for all operating conditions of MARS while reducing the computation burden by reducing the size of the matrix that is inverted at each simulation timestep.

To reduce the stiffness in the system and to avoid the requirement of circuit reconfiguration, a hysteresis relaxation technique is utilized for the  $\text{sgn}$  function and approximates the arm voltage, capacitor voltage for PV and ESS SM as shown in [75]. The details of the approximation process of arm voltage, capacitor voltage for PV and ESS SM are illustrated in [75]. A hysteresis relaxation algorithm is applied to the  $\text{sgn1}$  function in the DAEs that represent the dynamics of the DAB transformer current. The approximated  $v_{\text{dcpv},y,i,j}$  under blocked operating condition, as shown in Figure 2.4, are implemented as  $v_{\text{dcpv},y,i,j}[k] = v_{\text{dcpvn},y,i,j}[k] + i_{\text{acDAB2},y,i,j}[k]R_{pv,y,i,j}[k]$ , the detailed information on  $v_{\text{dcpvn},y,i,j}[k]$  and  $R_{pv,y,i,j}[k]$  is listed in (2.10) and (2.11).

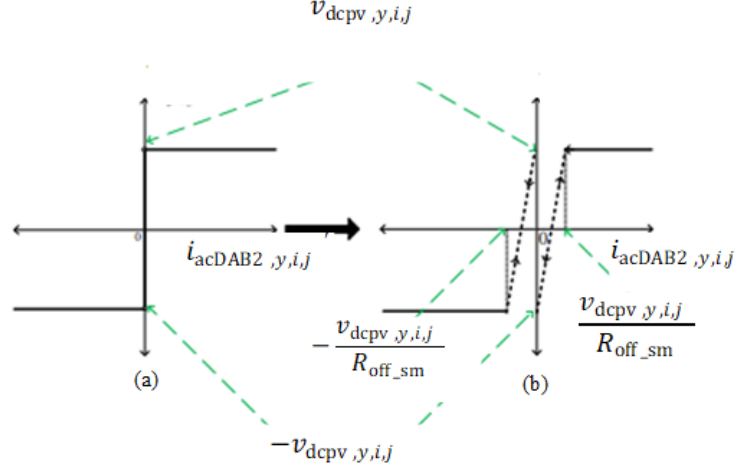


**Figure 2.4 – Hysteresis relaxation applied to isolated PV DAB inductor currents' dynamics during blocked state.**

$$v_{dcpvn,y,i,j}[k] = \begin{cases} v_{dcpvn,y,i,j}[k] * a, & \text{if } (i_{acDAB2,y,i,j}[k-2] > 0 \text{ and,} \\ & i_{acDAB2,y,i,j}[k-1] > \frac{v_{dcpvn,y,i,j}[k] * a}{R_{off\_sm}}) \\ -v_{dcpvn,y,i,j}[k] * a, & \text{if } (i_{acDAB2,y,i,j}[k-2] < 0 \text{ and,} \\ & i_{acDAB2,y,i,j}[k-1] < -\frac{v_{dcpvn,y,i,j}[k] * a}{R_{off\_sm}}) \\ v_{dcpvn,y,i,j}[k] * a, & \text{if } (i_{acDAB2,y,i,j}[k-1] < 0) \\ -v_{dcpvn,y,i,j}[k] * a, & \text{if } (i_{acDAB2,y,i,j}[k-1] > 0) \end{cases} \quad (2.10)$$

$$R_{pv,y,i,j}[k] = \begin{cases} R_{on\_sm}, & \text{if } (i_{acDAB2,y,i,j}[k-2] > 0 \text{ and } i_{acDAB2,y,i,j}[k-1] \\ & > \frac{v_{dcpvn,y,i,j}[k] * a}{R_{off\_sm}}) \\ R_{on\_sm}, & \text{if } (i_{acDAB2,y,i,j}[k-2] < 0 \text{ and } i_{acDAB2,y,i,j}[k-1] \\ & < -\frac{v_{dcpvn,y,i,j}[k] * a}{R_{off\_sm}}) \\ R_{off\_sm}, & \text{if } (i_{acDAB2,y,i,j}[k-1] < 0) \\ R_{off\_sm}, & \text{if } (i_{acDAB2,y,i,j}[k-1] > 0) \end{cases} \quad (2.11)$$

### 2.4.2 Interpolating Method

In the control system of the DAB converter, the delay in  $\mu\text{s}$  is rounded to the first decimal place to simplify the control implementation while preserving the resolution in the control of power flow. In the conventional simulators, the minimum timestep required is  $0.1 \mu\text{s}$  to simulate the DAB converter accurately. However, with the proposed interpolating method applied to DAB's discretized DAEs, the minimum simulation timestep can be increased to  $1 \mu\text{s}$  (or higher). Without loss of generality, let the switching signals  $S_{y,i,j,11}/S_{y,i,j,12}/S_{y,i,j,13}/S_{y,i,j,14}$  be the older signals  $S_{y,i,j,11\_old}/S_{y,i,j,12\_old}/S_{y,i,j,13\_old}/S_{y,i,j,14\_old}$  before the delay and be the newer signals  $S_{y,i,j,11\_new}/S_{y,i,j,12\_new}/S_{y,i,j,13\_new}/S_{y,i,j,14\_new}$  after the delay within a control time period. In the proposed interpolating method, the value of the delay in the switching signals  $S_{y,i,j,11}/S_{y,i,j,12}/S_{y,i,j,13}/S_{y,i,j,14}$  closest to the next simulation timestep is extracted. For example, if the simulation timestep is  $1 \mu\text{s}$  and the delay is  $7.2 \mu\text{s}$ , the value extracted here is  $8 \mu\text{s}$ . In the simulation timestep corresponding to the extracted value within every control time period  $T$ ,  $S_{y,i,j,11\_old}/S_{y,i,j,12\_old}/S_{y,i,j,13\_old}/S_{y,i,j,14\_old}$  are applied as the switching signals for delay – (extracted value – 1) time. For the rest of the time within the current simulation timestep,  $S_{y,i,j,11\_new}/S_{y,i,j,12\_new}/S_{y,i,j,13\_new}/S_{y,i,j,14\_new}$  are applied as the switching signals. In the preceding example, in the 8<sup>th</sup> simulation timestep that corresponds to the simulation time between  $7 \mu\text{s}$  and  $8 \mu\text{s}$  in the current control time period, the older signals are applied for  $0.2 \mu\text{s}$  while the newer signals are applied for  $0.8 \mu\text{s}$  in the discretized DAEs. Prior to and post the extracted value based timestep, older and newer switching signals are applied, respectively, in the discretized DAEs. To implement this algorithm, in each control time period, the discretization of the DAEs representing the front-end half-

bridge capacitor voltage dynamics and the DAB transformer current dynamics at  $t = \text{Ceiling}\left(\frac{\text{delay}_{y,i,j}}{h}\right)h$  and  $t = \frac{T}{2} + \text{Ceiling}\left(\frac{\text{delay}_{y,i,j}}{h}\right)h$  or  $k = \text{Ceiling}\left(\frac{\text{delay}_{y,i,j}}{h}\right)$  or  $\frac{m}{2} + \text{Ceiling}\left(\frac{\text{delay}_{y,i,j}}{h}\right)$  are modified to (2.12) and (2.13), respectively. The  $h$  term represents the simulation timestep, while  $k$  is defined as the number of timesteps taken from  $t = 0$ ,  $m = T/h$ . For the rest of the time, the discretized DAEs remain unchanged and are given in (2.14) and (2.15).

$$\begin{aligned}
di_{acDAB2,y,i,j}'[k] &= \left\{ i_{acDAB2,y,i,j}' \times [k-1] \frac{t_1}{L_t} \times S_1[k] \times V_{cy,l,j}[k] \right. \\
&\quad + \frac{h}{L_t} S_{BLDAB1}[k] \times v_{cn,y,i,j}[k] - \frac{h}{L_t} a \times S_2[k] \times V_{dcpv,y,i,j}[k] \\
&\quad \left. - S_{BLDAB2}[k] \times v_{dcpvn,y,i,j}[k] + \frac{t_2}{L_t} \times S_{1\_old}[k] \times V_{cy,i,j}[k] \right\} / deno
\end{aligned} \tag{2.12}$$

where

$$S_1[k] = S_{y,i,j,13}[k] \times S_{y,i,j,12}[k] - S_{y,i,j,14}[k] \times S_{y,i,j,11}[k]$$

$$S_2[k] = S_{y,i,j,23}[k] \times S_{y,i,j,22}[k] - S_{y,i,j,24}[k] \times S_{y,i,j,21}[k]$$

$$S_{1\_old}[k] = S_{y,i,j,13\_old}[k] \times S_{y,i,j,12\_old}[k] - S_{y,i,j,14\_old}[k] \times S_{y,i,j,11\_old}[k]$$

$$S_{2\_old}[k] = S_{y,i,j,23\_old}[k] \times S_{y,i,j,22\_old}[k] - S_{y,i,j,24\_old}[k] \times S_{y,i,j,21\_old}[k]$$

$$t_1 = h - \text{delay}_{y,i,j}[k] + \text{FLOOR}(\text{delay}_{y,i,j}[k])$$

$$t_2 = \text{delay}_{y,i,j}[k] - \text{FLOOR}(\text{delay}_{y,i,j}[k])$$

$$\text{deno} = 1 + \frac{h}{L_t} * R_t + \frac{h}{L_t} R_{dcpv,y,i,j}[k] S_{BLDAB2}[k] + \frac{h}{L_t} R_{c,y,i,j}[k] S_{BLDAB1}[k]$$

$$V_{cy,i,j}[k] = V_{cy,i,j}[k-1] * \left(1 - h * \frac{C_{sm}}{R_p}\right) + \frac{h}{C_{sm}} (1 - S_{y,i,j,1}) * i_{acHB,y,i,j}[k] \quad (2.13)$$

$$\begin{aligned} & - \frac{t_1}{C_{sm}} S_2[k] \times i_{acDAB2,y,i,j}'[k] - \frac{h}{L} S_{BLDAB1}[k] \times |i_{acDAB2,y,i,j}'[k]| \\ & - \frac{t_2}{C_{sm}} S_{2\_old}[k] \times i_{acDAB2,y,i,j}'[k] \end{aligned}$$

$$di_{acDAB2,y,i,j}'[k] \quad (2.14)$$

$$\begin{aligned} & = \left\{ i_{acDAB2,y,i,j}'[k-1] \frac{h}{L_t} \times S_1[k] \times V_{cy,i,j}[k] \right. \\ & + \frac{h}{L_t} S_{BLDAB1}[k] \times v_{cn,y,i,j}[k] - \frac{h}{L_t} a \times S_2[k] \times V_{dcpv,y,i,j}[k] \\ & \left. - S_{BLDAB2}[k] \times v_{dcpvn,y,i,j}[k] \right\} / \text{deno} \end{aligned}$$

$$V_{c,y,l,j}[k] = V_{c,y,l,j}[k-1] * \left(1 - h * \frac{C_{sm}}{R_p}\right) + \frac{h}{C_{sm}} (1 - S_{yl1,j}) * i_{acHB,y,l,j}[k] \quad (2.15)$$

$$- \frac{h}{C_{sm}} \times S_2[k] \times i_{acDAB2,y,i,j}'[k] - \frac{h}{L} S_{BLDAB1} \times |i_{acDAB2,y,i,j}'[k]|$$

## 2.5 Simulation Results and Comparison

In this section, two case studies, one with a single DAB converter and the other with a MARS with multiple PV SMs (and DABs), are used to compare the results obtained from the proposed simulation algorithm with the reference results. The test system for the

MARS is described in [70] and [78]. The DAB circuit parameters, such as the transformer leakage inductance, resistance referred to the primary side, PV side capacitor, and switching frequency are tabulated in Table 2.2. The parameters of the DAB simulation are provided in Table 2.3.

**Table 2.2 – Pittsburgh MARS system DAB parameters**

Parameter	Value
DAB leakage inductance referred to primary side ( $L_t$ )	100 $\mu$ H
DAB resistance referred to primary side ( $R_t$ )	0.001 $\Omega$
DAB PV-side capacitor ( $C_{dcpv}$ )	1mF
Switching frequency for PV and ESS converters ( $f_{sw}$ )	10000.0 Hz
DAB transformer turns ratio ( $a$ )	1.6

**Table 2.3 – Pittsburgh MARS system DAB simulation parameters**

Parameter	Value
Simulation interpolation accuracy	0.1 $\mu$ s
DAB timestep chosen (proposed model)	1 $\mu$ s
DAB timestep chosen (reference model)	0.1 $\mu$ s
Switch-off parameters for PV and ESS converters ( $R_{off\_sm}$ )	1e6 $\Omega$
Switch-on parameters for PV and ESS converters ( $R_{on\_sm}$ )	1e-3 $\Omega$
MARS front-end half-bridge switch-off parameters ( $R_{off}$ )	1e6*N $\Omega$
MARS front-end half-bridge switch-on parameters ( $R_{on}$ )	1e-3*N $\Omega$

### 2.5.1 Single DAB

A time-domain single DAB switching model is developed in the PSCAD software environment using library components that serve as the reference model (and this is in

addition to the model generated from the application of the proposed simulation algorithm to the high-fidelity switched system DAB converter model). Both models are simulated in open loop with a defined delay value. The PV side capacitor voltage and the transformer current obtained from the simulation of DAB converter with the proposed algorithm and from the simulation of the reference model are compared in Figure 2.5.

The delay is represented until the first decimal point. The proposed high-fidelity DAB model is able to achieve the accuracy by using a timestep of  $1\text{ }\mu\text{s}$  while the DAB circuit using PSCAD components has to use the timestep of  $0.1\text{ }\mu\text{s}$ . The input delay changes from  $7.8\text{ }\mu\text{s}$  to  $7.2\text{ }\mu\text{s}$ . As observed from Figure 2.5, the transformer inductor current and the capacitor voltage of the proposed high-fidelity model and the reference model overlap, with an error of less than 0.4% in the states. The results validate the accuracy of the proposed simulation algorithm in single DAB open-loop control case study.

The time taken to simulate 1 s with the proposed simulation algorithm is 3.42 mins, while it takes 35.1 mins to simulate using the reference model without the interpolating method with a timestep of  $0.1\text{ }\mu\text{s}$ . The improvement is around 10 times.

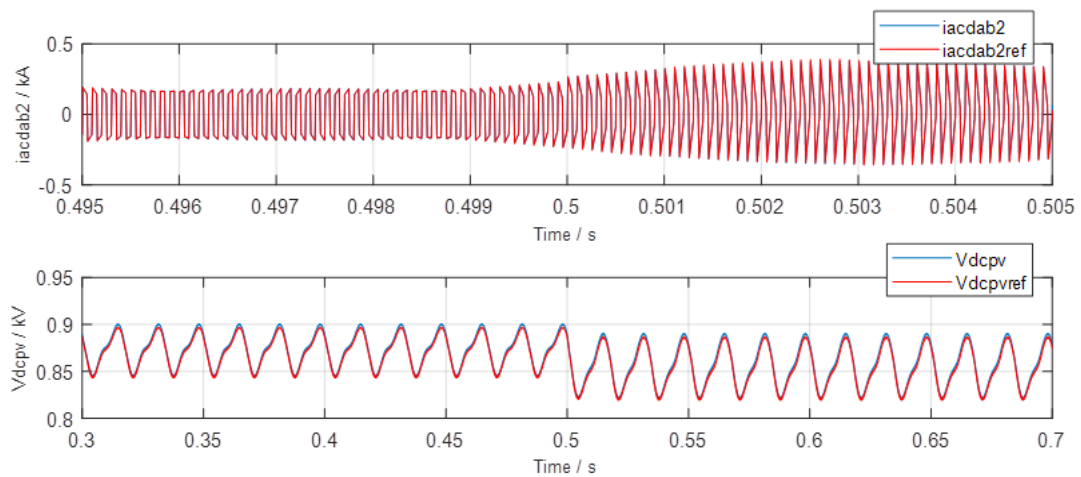


**Figure 2.5 – Comparison of the simulation results for the proposed algorithm and reference model.**

### 2.5.2 MARS

The closed-loop control of the DAB converters in the MARS model (with 666 isolated PV SMs) is compared with the corresponding closed-loop control of a single DAB circuit model developed in MATLAB/Simulink using library components. Both models are given the reference power of  $P_{pvref} = 100 \text{ MW}$ . The delays generated by the MATLAB model and by one of the DAB converters in the MARS model are very similar, as shown in Figure 2.6. The average error is 3%. The speedup of the proposed algorithm to simulate a MARS compared to the MARS developed using library components in MATLAB or PSCAD is expected to be of the order of thousands to tens of thousands. The estimation is based on [78] and the speedup observed with a single DAB converter simulation.

The transformer current and the PV side capacitor voltages under the steady state operating condition  $P_{pvref} = 100 \text{ MW}$  for all three phases of MARS are illustrated in Figure 2.7. The observed shape of the voltage in Figure 2.7 arises from the presence of the fundamental and second-order harmonics in the SM-side capacitor voltage. The average value of the voltage is tracking its reference value generated from the PV model.

A step change of the PV reference power from 100 MW to 30 MW is applied in the simulation at  $t = 0.5 \text{ s}$ . The measured transformer current and the PV side capacitor voltage are provided in Figure 2.8. The transition observed is as expected. These studies indicate the stability of the proposed simulation algorithm to simulate MARS under different operating conditions.



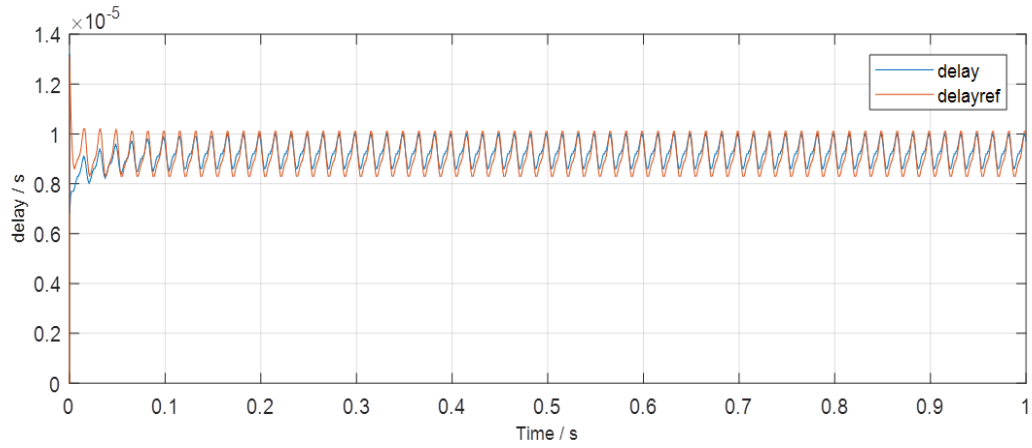


**Figure 2.6 – Comparison of the simulation results for the proposed algorithm and reference model.**

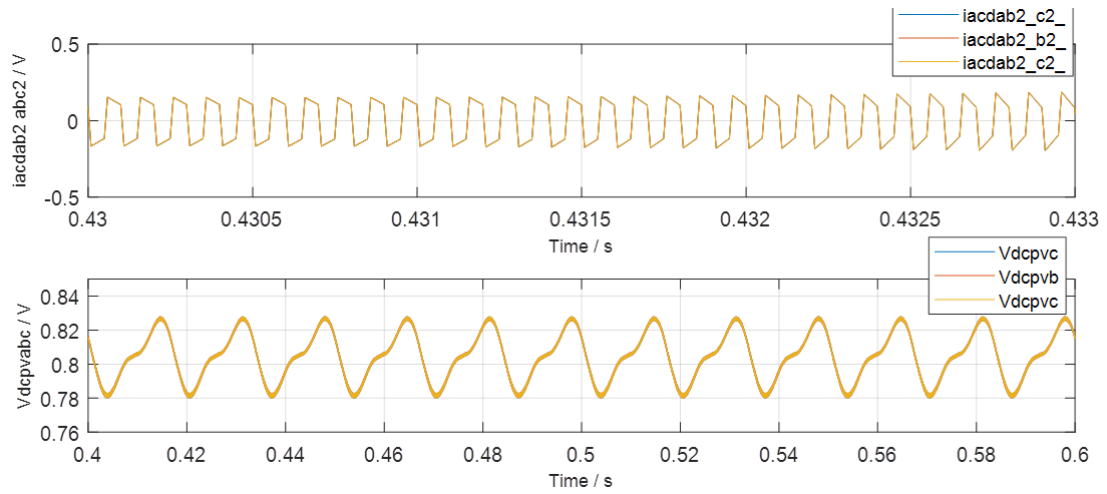


**Figure 2.7 – Transformer current and PV-side capacitor voltage waveforms for the proposed algorithm.**

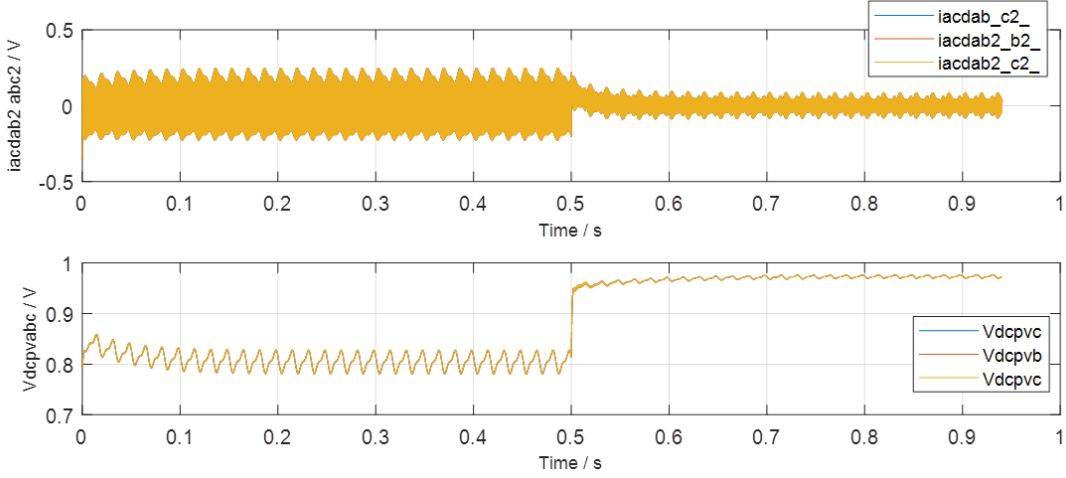


**Figure 2.8 – Transformer current and PV-side capacitor voltage waveforms for the proposed algorithm.**

## 2.6 Summary

In this chapter, the reduced-order model and the high-fidelity model of the MARS are introduced as the testbed for the later advanced control design. Simulation algorithms are proposed to simulate the DAB and MARS power plant with isolated PV SM. The proposed algorithm utilizes hybrid discretization to separate the differential-algebraic equations and discretize the non-stiff and stiff systems with different discretization methods. The interaction between the stiff and non-stiff systems is stabilized through a hysteresis relaxation algorithm. The interpolating method is used to increase the minimum timestep required to simulate the isolated DAB converter present in the MARS while maintaining the resolution of the delay being sent to the switching gate. These algorithms are applied to both the single DAB converter model and MARS model and the results generated from simulations are compared with the simulation of PSCAD single DAB (open-loop) and MATLAB single DAB converter (closed-loop) reference model. A speed-up of the order 10 times is achieved in the single DAB model. The errors in simulating a

single DAB model and MARS model by the proposed algorithms are 0.4% and 3%, respectively. A speed-up of the order of thousands to tens of thousands is expected when the full system of MARS model is developed in the PSCAD or MATLAB.

## CHAPTER 3. HIERARCHICAL CONTROL OF THE MARS

The control objective of the MARS is to track the power dispatch command, provide continuity of operation under low short circuit ratio (SCR) conditions, and enable fast frequency support when a loss of generation event happens. The hierarchical control system shown in Figure 3.1 is designed to control the MARS and achieve the control objectives. It consists of L1, L2, and L3 controllers.

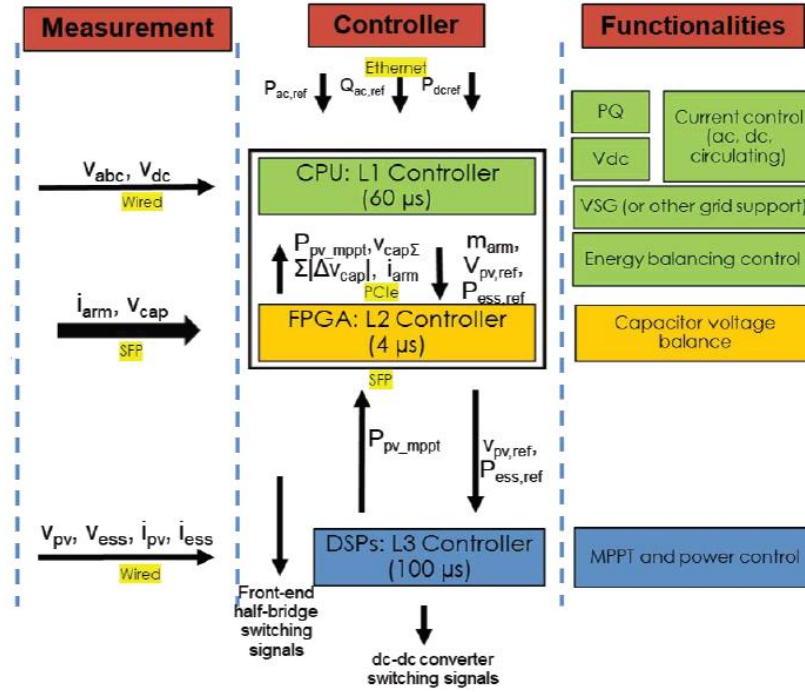
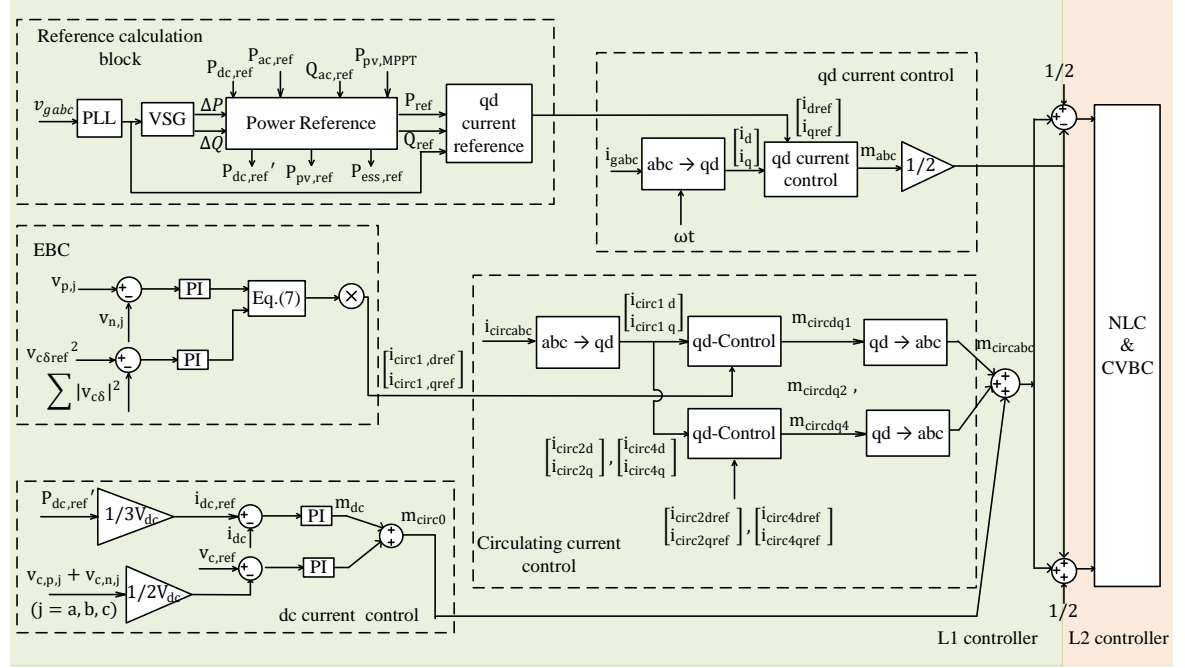


Figure 3.1 – Hierarchical control system to control the MARS.

### 3.1 L1 Control

The detailed implementation of the L1 controller is shown in Figure 3.2. The controller gains have been tuned using either approximate linear time-invariant models or

linearized models such that the controlled states are well separated with respect to their corresponding time constants.



**Figure 3.2 – Block Diagram of L1 and L2 controllers.**

### 3.1.1 qd Current Controller

The qd current controller aims at controlling the power flow at the point of common coupling. It is systematically designed using the dynamic model of the MARS. The closed-loop qd current control system is shown in Figure 3.3, and the closed-loop transfer function of the grid current control is given in (3.1).

$$\frac{I_{qd}(s)}{I_{qd,ref}(s)} = \frac{sK_p + K_i}{L_s s^2 + (R_s + K_p)s + K_i} \quad (3.1)$$

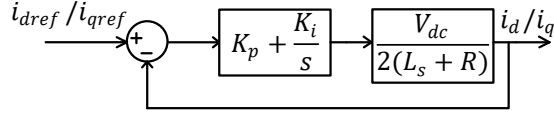


**Figure 3.3 – Control block diagram of qd current controller.**

Gains  $K_p$  and  $K_i$  are tuned using the characteristic equation  $s^2 + \frac{(R_s + K_p)}{L_s}s + \frac{K_i}{L_s}$  such that the settling time  $8L_s/(R_s + K_p)$  is an order of magnitude greater than the settling time of the current filters. With designed settling time  $t_{s,qd}$  and damping constant  $\delta$ , the PI controller parameters in the qd current controller are given by:

$$K_p = 8 \left( \frac{L_s}{t_{s,qd}} \right) - R_s \quad (3.2)$$

$$K_i = \frac{(R_s + K_p)^2}{4\delta^2 L_s} \quad (3.3)$$

### 3.1.2 Circulating Current Controller

The dc current controller and the circulating current controller of the MARS are considered as internal controllers. The objectives of the internal controllers are to regulate the dc circulating current to a specific value, the 2nd and 4th order of ac ones to zero, and the fundamental circulating current to the reference value generated by EBC. It has been proved by [79] that paralleled PI controllers, aiming at regulating multiple frequency components of circulating current, will have separate operating frequency ranges for different controllers. Thus, the performance will not be affected by each other. In this thesis, the unbalanced controller in [70] is adopted as the dc current controller. To properly control the dc current, the reference of dc current is estimated through the dc power

command, and an additional term is added to estimate losses and inaccuracies. The reference value for the dc component of phase-j is given by:

$$\begin{aligned} i_{dc,j,ref} &= \left\langle \frac{m_j i_j}{2} \right\rangle + K_{pv} (0.5 \langle v_{c,j}^\Sigma \rangle - v_{c,ref}) i_{dc,j,ref} \\ &= \left\langle \frac{m_j i_j}{2} \right\rangle + K_{pv} (0.5 \langle v_{c,j}^\Sigma \rangle - v_{c,ref}) \end{aligned} \quad (3.4)$$

where  $K_{pv}$  is the proportional controller gain and  $\langle x \rangle$  is the dc component of x. The gain  $K_{pv}$  is chosen such that the settling time of the system is an order of magnitude greater than the settling time of the filters.

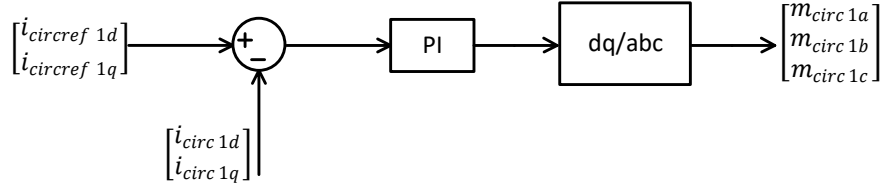


**Figure 3.4 – Control block diagram of ac components of the circulating current.**

The closed-loop control system of the circulating currents' ac components of the is summarized in Figure 3.5. The transfer function of the closed-loop control system is given by:

$$\frac{s^2 L_o + s R_o}{L_o s^2 + (R_o + K_{pc})s + K_{ic}} \quad (3.5)$$

Thus, the settling time of the closed-loop circulating current control is given by:

$$t_{s,circ} = 8 \frac{L_o}{R_o + K_{pc}} \quad (3.6)$$

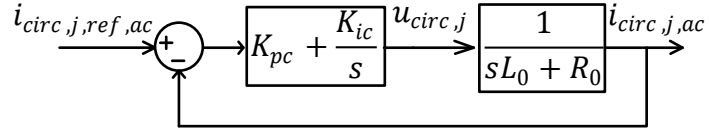


**Figure 3.5 – Control block diagram of the ac components of the circulating current.**

The design of the proportional controller gain depends upon the following constraints: (i)  $t_{s,qd} \ll t_{s,cir} \ll t_{s,EBC}$ ; This is to ensure that the qd current controller settles much faster than the internal controller and then the EBC settles down. (ii) The closed-loop control system should not attenuate the common-mode frequency components in the circulating currents.

The capacitor voltage balancing of PV SM, ESS SM, and normal SM is achieved by the EBC. The settling time of the EBC controller is investigated using the PSCAD/EMTDC MARS high-fidelity model.

### 3.1.3 Energy Balancing Control

For individual SMs within the phase arms of a traditional MMC, it is assumed that a sorting algorithm maintains the SM capacitor voltage balance. However, the analysis of an MMC with distributed PV and ESS differs from a standard MMC due to the added power injection from PV and the charging/discharging of the ESS units. The uneven power distribution in one arm leads to large steady-state power transfers within the MARS or MMC with distributed sources that do not exist in a standard MMC. The capacitor voltages of different types of SMs cannot be maintained to be balanced under various operating conditions of MARS due to the limitation of the sorting algorithms.

#### 3.1.3.1 Mechanism of Capacitor Voltage Disparity



For the MARS system, the sorting algorithm cannot guarantee that the injected power to each SM does not exceed the maximum possible power transfer under all operating conditions. Especially when dc and ac powers are small, the peak of the arm current would also be small. Thereby, the energy that the capacitor can store is relatively small. For example, under the operating condition of  $P_{ac} = 100\text{MW}$ ,  $Q_{ac} = 100\text{MW}$ ,  $P_{pv} = 100\text{MW}$ , and  $P_{ess} = 30\text{MW}$ , the upper arm current  $I_{p,a} = \frac{I_{dc}}{3} + \frac{\hat{I}^t}{2} \cos(\omega t - \varphi^t) = -25 + \frac{186}{2} \cos(\omega t - \varphi^t)$ . Thus, the negative peak upper arm current is around 118 A. Under this condition, for 111 PV SMs, the maximum energy transfer under normal operating conditions during negative current period is  $\int_{\frac{1}{4}T}^{\frac{3}{4}T} \left\{ \frac{I_{dc}}{3} + \frac{\hat{I}^t}{2} \cos(\omega t - \varphi^t) \right\} * 111 * 6 * v_{c,nominal} dt = 0.7472 \text{ MW*s}$  when assuming that the capacitor voltage at  $t = \frac{1}{4}T$  is 1600 V which is the nominal capacitor voltage ( $v_{c,nominal}$ ). The voltage at time  $\frac{3}{4}T$  is calculated as  $V_c\left(\frac{3}{4}T\right) = V_c\left(\frac{1}{4}T\right) + \frac{1}{C} \int_{\frac{1}{4}T}^{\frac{3}{4}T} \left\{ \frac{I_{dc}}{3} + \frac{\hat{I}^t}{2} \cos(\omega t - \varphi^t) \right\} dt$ . Therefore, the net energy change in the SM capacitor is  $W_c = \int_{\frac{1}{4}T}^{\frac{3}{4}T} \left\{ \frac{I_{dc}}{3} + \frac{\hat{I}^t}{2} \cos(\omega t - \varphi^t) \right\} * 111 * 6 * 1600 - \frac{1}{2} C * \left( V_c\left(\frac{3}{4}T\right)^2 - V_c\left(\frac{1}{4}T\right)^2 \right) = 0.71639 \text{ MW * s}$ . However, the energy of the PV system flowing into the capacitor is  $W_{pv} = 100\text{MW} * \frac{1}{2}T = 0.83333 \text{ MW * s}$ , which is greater than the energy that the SM capacitor can supply. To balance the input and output energy, the voltage of the PV SM capacitor needs to increase, leading to the capacitor voltage disparity of different types of SMs in one arm.

The above discussion is a rough analysis of the capacitor voltage disparities where the reactive power is not taken into consideration for simplicity. However, the reactive

power is also an essential factor that will positively influence the arm current [35] for some cases and will be showcased in the cHIL test results of chapter 4.

### 3.1.3.2 EBC Mathematical Model

In the MARS system, the upper and lower limits of the capacitor voltages are set based on the designed stability constraints. The lower limit ensures the stable operation of the L3 controller, while the upper limit is set to avoid the over-voltage stress of the switches. The operating conditions in which the SM capacitor voltages are within limits are considered stable. In addition to the voltage, the dc current ripple is limited to less than 20% of the nominal current. Both capacitor voltage limit and dc current restriction should be simultaneously met to ensure that an operating condition is stable. Circulating current can be utilized to help distribute the external power in inter-arms and intra-arms and increase the charging/discharging capability of the SMs without affecting the ac and dc terminals of the MARS system.

The SM capacitor voltage difference, which is measured and controlled to stabilize the system, is defined as:

$$\begin{aligned}
 \sum (V_{c\sigma})^2 = & \sum_{i=1}^N (v_{c,p,i,a} - \frac{v_{p,a}}{N})^2 + \sum_{i=1}^N (v_{c,n,i,a} - \frac{v_{n,a}}{N})^2 \\
 & + \sum_{i=1}^N (v_{c,p,i,b} - \frac{v_{p,b}}{N})^2 + \sum_{i=1}^N (v_{c,n,i,b} - \frac{v_{n,b}}{N})^2 \\
 & + \sum_{i=1}^N (v_{c,p,i,c} - \frac{v_{p,c}}{N})^2 + \sum_{i=1}^N (v_{c,n,i,c} - \frac{v_{n,c}}{N})^2
 \end{aligned} \tag{3.7}$$

where  $v_{cp(n),i,a}$  is the  $i$ -th SM capacitor voltage of the upper (lower) arm “ $p$ ” (“ $n$ ”) for a given phase A.  $\sum(V_{c\sigma})^2$  captures deviation of all SM capacitor voltages from the average voltage.

In Figure 1.1, the upper and lower arm currents of phase  $j$ , i.e.,  $i_{pa}$  and  $i_{na}$  are expressed by:

$$i_{p,j} = \frac{i_{gj}}{2} + i_{dj} + I_{0j} \quad (3.8)$$

$$i_{n,j} = -\frac{i_{gj}}{2} + i_{dj} + I_{0j} \quad (3.9)$$

where  $I_{0j}$  denotes the dc component and  $i_{dj}$  denotes the fundamental frequency component. The dc components transfer between the dc link and each phase arms, while the fundamental frequency circulating components enables power transfer inter-arms and inter-SMs. The second and forth order harmonic circulating currents are suppressed by the circulating current controller to increase the system efficiency.

Similarly, the upper and lower arm voltages can be expressed using  $V_{DC}$ , voltage  $v_L$  for generating ac output current, and the voltage corresponding to the circulating current  $v_d$ .

$$v_{p,j} = \frac{V_{DC}}{2} - v_{L,j} - v_{d,j} \quad (3.10)$$

$$v_{n,j} = \frac{V_{DC}}{2} + v_{L,j} + v_{d,j} \quad (3.11)$$

The phase-j load dynamic is given by:

$$v_{gj} = v_{s,j} + \left(\frac{L_o}{2} + L_s\right) \frac{di_{gj}}{dt} + \left(\frac{R_o}{2} + R_s\right) i_{gj} \quad (3.12)$$

$$v_{dj} = L_o \frac{di_{dj}}{dt} + R_o i_{dj} \quad (3.13)$$

where  $v_{gj}$  represents the ac grid output voltage.

Thus, considering the power transfer by the external sources  $P_{p,j}^{ext}$ , the average power of the upper and lower arms can be calculated as:

$$P_{p,j} = v_{p,j} i_{p,j} - P_{p,j}^{ext} \quad (3.14)$$

$$P_{n,j} = v_{n,j} i_{n,j} - P_{n,j}^{ext} \quad (3.15)$$

The circulating active power is defined as  $P_{dj} = \frac{P_{p,j} - P_{n,j}}{2}$ , which by substituting for  $P_{p,j}$  and  $P_{n,j}$ ,  $P_{dj}$  from (3.8)-(3.13) becomes:

$$P_{dj} = \frac{v_{gj} i_{dj}}{2} \cos(\gamma) \quad (3.16)$$

The circulating reactive power  $Q_{dj}$  is written as:

$$Q_{dj} = -\frac{v_{gj} i_{dj}}{2} \sin(\gamma) \quad (3.17)$$

To maintain the stability of the dc link voltage, the dc power injected along with the external power input should be equal to the ac power leaving the ac side of the MARS.

The EBC shown in Figure 3.6 generates  $P_{dj,ref}$  and  $\sum Q_{dj,ref}(j=a,b,c)$  respectively by: (1) reducing the differences between the upper and lower arm voltages. (2) controlling  $\sum |v_{c\delta}|^2$ , i. e., the summation of the absolute value of the difference between the individual capacitor voltages and the average capacitor voltages in each arm, to its reference value ( $v_{c\delta,ref}^2$ ). The circulating current references are then calculated based on the method proposed in [35] and by neglecting negative -sequence components. The formulation of the references is shown in (3.18).

$$i_{circ,1,q} = \frac{2v_{y,j}}{3} (P_{da,ref} + P_{db,ref} + P_{dc,ref}) \quad (3.18(a))$$

$$i_{circ,1,d} = \frac{2v_{y,j}}{3} (Q_{da,ref} + Q_{db,ref} + Q_{dc,ref}) \quad (3.18(b))$$

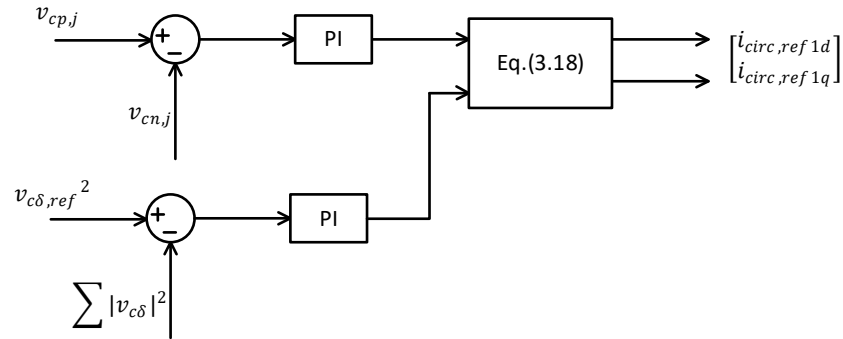


**Figure 3.6 – The EBC of the MARS.**

### 3.2 L2 control

The L2 controller receives modulation indices from L1 controller to control the arm voltage of the MARS. It also receives the measured arm currents and SMs front-end half-bridge capacitor voltages from the MARS. The L2 controller includes an updated SM capacitor voltage balancing algorithm which helps maintains the SM capacitor voltages balanced in each arm and is based on the existing SM capacitor voltage balancing algorithm [70]. It also generates the switching signals for the front-end half-bridges of all SMs through Nearest Level Modulation (NLM). The NLM brings more flexibility and more straightforward digital implementation when the number of voltage levels is high, as it avoids the use of any triangular carrier wave. Instead, it uses a rounding function to directly compute the switching states and duty cycles for each phase of the converter.

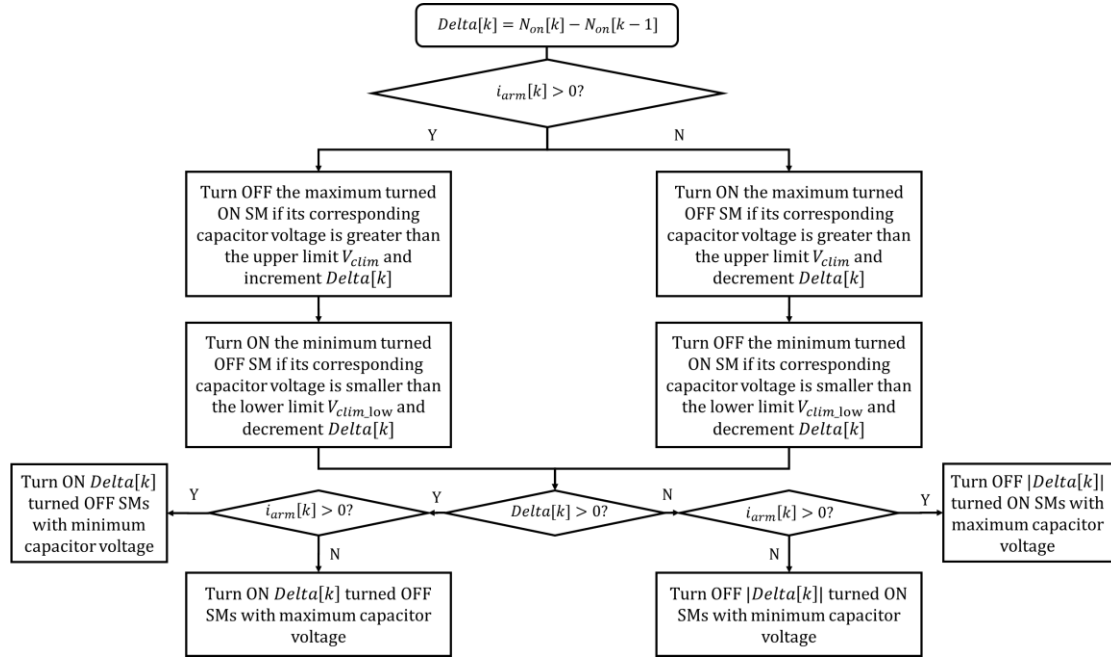


**Figure 3.7 – Block diagram of L2 controller.**

The proposed L2 controller determines the number of additional front-end half-bridges that need to be turned ON/OFF and is identified based on the already turned ON

front-end half-bridges prior to the current L1 controller timestep. The number is referred to as delta and it represents the changes that need to be made at the current time step when following the reference signal and compared with the number of inserted SMs in previous control cycles. Apart from the delta, the status of a pair of front-end half-bridges in each arm may be swapped based on the direction of arm current and if the minimum or maximum SMs front-end half-bridge capacitor voltage violates a pre-defined lower or upper limit. The previous EBC is not strong enough to deal with specific operating conditions, e.g., when PV SMs are working on the MPPT while the ESS SMs are working on charging the battery. As shown in Figure 3.7, the new voltage balancing control increases the extra switching time within a control cycle to deal with the SM voltage below the voltage limit. In addition, instead of turning the first SM on or off, which violates the voltage limit, the maximum/minimum voltages are turned on/off. The L2 controller repeats the whole process to improve the capacitor voltage ripple.

The improved efficiency of the L2 controller can be observed under some operating conditions, as shown in Figure 3.8. However, there are still a significant number of operating conditions that are not viable for the MARS.

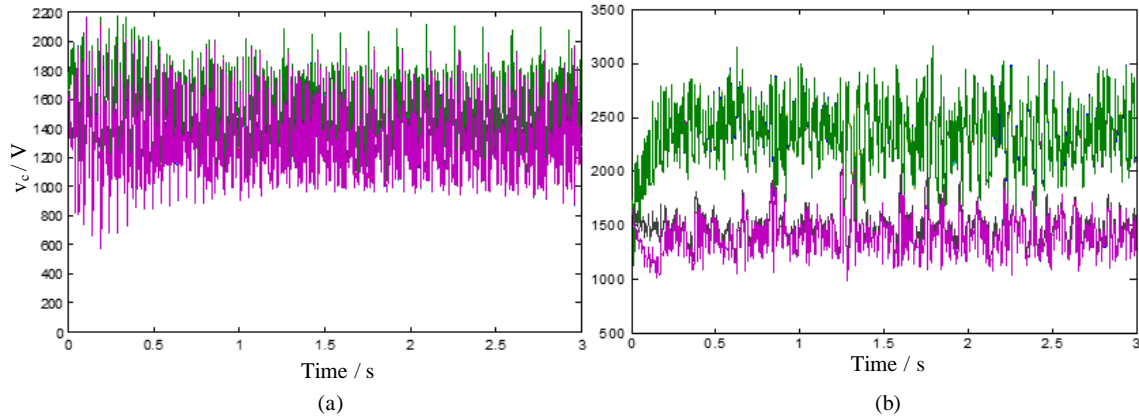


**Figure 3.8 – Upper arm phase A capacitor voltages under the operating point of  $P_{dc} = -30\text{MW}$ ,  $P_{ac} = 100\text{ MW}$ ,  $P_{pv} = 100\text{ MW}$ ,  $P_{ess} = 30\text{MW}$  (a) With the MARS current control, and (b) Without the MARS current control.**

### **3.3 L3 Control**

L3 controllers are the local controller in PV and ESS SMs, which regulate the power transferred from PV and ESS. The L3 controller in PV SM utilizes the double loop control, the outer-loop tracks the PV power reference sent by the L1 controller, while the inner-loop controls the inductor current. The L3 control block diagrams are depicted in Figure A.1 and Figure A.2. Taking into consideration the slope of the PV curve [78], the transfer function  $G_1(s)$  between inductor current and duty ratio is obtained. When inner- and outer-loop controller parameters are calculated, the interaction between the two loops must be considered. The inner-loop and outer-loop characteristic equations are derived using the multi-state closed-loop system response, and the tuning of the inner- and outer-loops is based upon the settling time. The PI controller parameter is derived such that the settling time of the inner-loop is 10 times faster than the outer-loop to ensure the stability of the double loop control. The ESS control is similarly designed with the detailed derivation in Appendix A.

### **3.4 PSCAD Offline Simulation of High-fidelity Model of the MARS**

The MARS system is developed based on the HVdc substation of the TransBay Cable project in Pittsburg, CA [80] and tested with the Western Interconnection (WECC)-based ac grid models. The 200A, 3.3kV SiC MOSFETs are used in the design. The dc link voltage in the TransBay Cable project determines the designed size of the MARS ESS, power rating of PV system, and the number of normal, ESS, and PV SMs. The parameters



of the MARS system are tabulated in Table 3.1. The communication delay has been considered in the offline model, given a more practical environment to evaluate the control algorithms of the MARS.

**Table 3.1 – MARS system parameters.**

System Parameters	Value
Simulation time-step	60 $\mu$ s
System capacity (base power rating)	400 MVA
System frequency	60 Hz
dc link voltage	$\pm 200$ kV
ac terminal voltage	220 kV
Arm inductor	30 mH
Front-end half-bridge capacitor	7.7 mF
Front-end half-bridge capacitor voltage	1.6 kV
Number of PV-SMs/arm	111
Number of ESS-SMs/arm	37
Number of normal-SMs/arm	102
Total number of SMs/arm	250

Multiple operating conditions are tested under the PE-HIL, the test results of 3 of them are presented here.

#### 3.4.1 Cyclic Test Under Various Operating Conditions

In this case study, the dispatch command steps from  $P_{ac}=300$  MW,  $Q_{ac}=0$ ,  $P_{dc}=300$  MW (EBC disabled by the EBC criteria) to  $P_{ac}=150$  MW,  $Q_{ac}=200$  MVar,  $P_{dc}=150$  MW (EBC enabled by the EBC criteria),  $P_{ac}=100$  MW,  $Q_{ac}=-50$  MVar,  $P_{dc}=60$  MW (EBC enabled by the EBC criteria), and  $P_{ac}=-50$  MW,  $Q_{ac}=0$ ,  $P_{dc}=-74$  MW (EBC

enabled by the EBC criteria), and back to the first operating condition to perform the cyclic test. The four different steady state operating conditions with operating conditions transitioning from enabling EBC to disabling EBC are simulated. The results of the cyclic test of different steady-state operating conditions with the hierarchical control are presented and shown in Figure 3.9-Figure 3.11. The results indicate that the system remains stable during the operating condition changes, with a fast and acceptable transient response. The real-time results, as shown in Figure 3.11, indicate the normal operation of the PV and ESS dc-dc converters under different sets of dispatch ac-side power commands. It can be observed from Figure 3.10 that the SM front-end half-bridge capacitor voltages are balanced within the required range, confirming the successful operation of the L2 and L3 controllers.

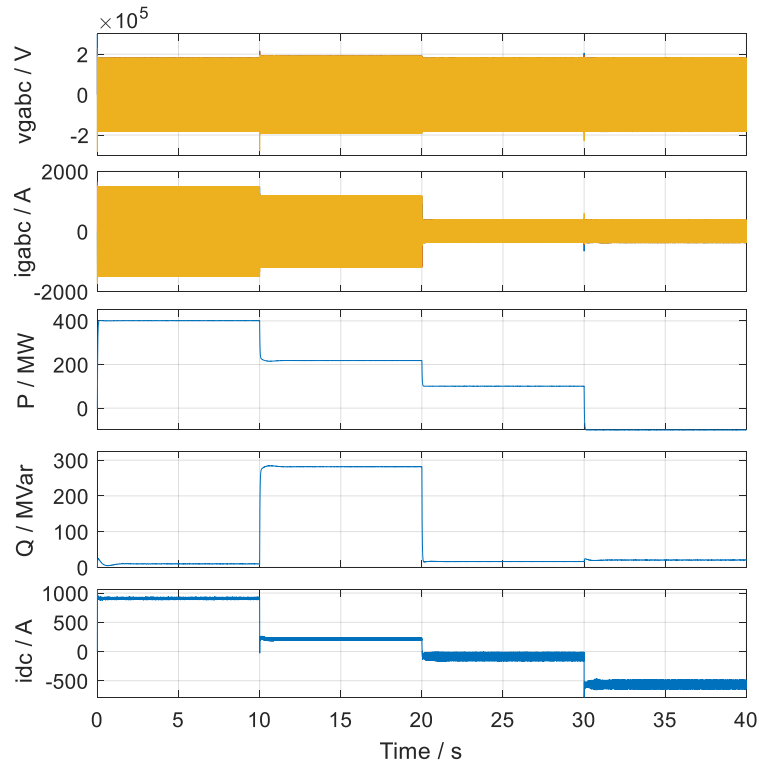


**Figure 3.9 – MARS grid-side measured three-phase voltages and currents, active and reactive powers, and dc current.**

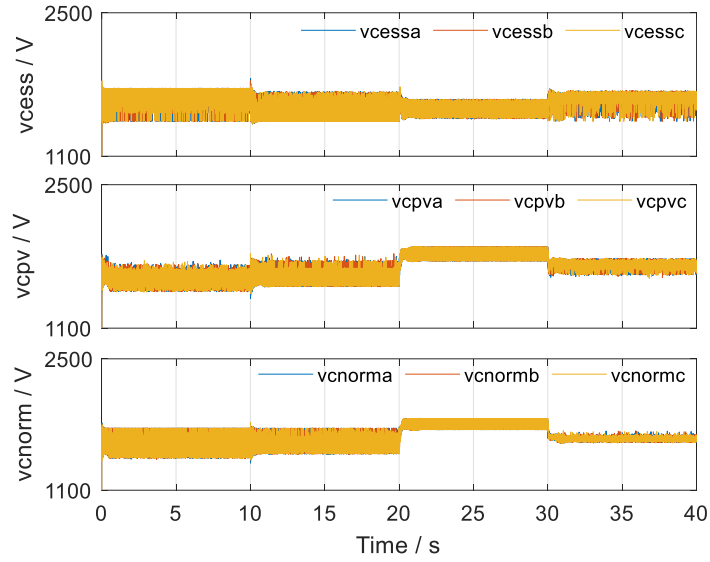


**Figure 3.10 – Capacitor voltages in representative SMs subsequent to changes in the operating condition.**

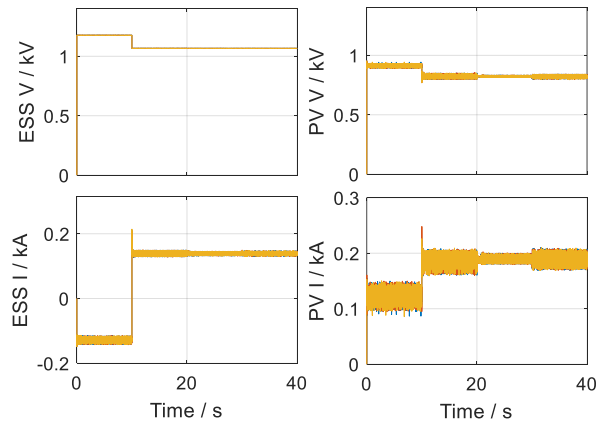


**Figure 3.11 – One PV and ESS converter outputs.**

### 3.4.2 The MARS System Under Different Grid Events

Three grid events are identified and tested for multiple operating conditions. Only the simulation results of the operating condition  $P_{ac}=300$  MW,  $Q_{ac}=0$ , and  $P_{dc}=300$  MW are presented in this section.

**Grid event 1: 3-Phase Fault.** A 3-phase fault is simulated on the transmission line between the grid and the MARS system at  $t = 4.0$  s with a fault duration of 0.2 s. After 0.2 s, the fault is self-cleared. Improvement in the voltage profiles of phase-a during the fault is shown in the Figure 3.12 with the help of the VSG support. From Figure 3.12, it can be observed that reactive power is injected to provide voltage support, thus, the MARS can provide continuity of operation successfully during the fault and operates in a stable mode during post-fault conditions.

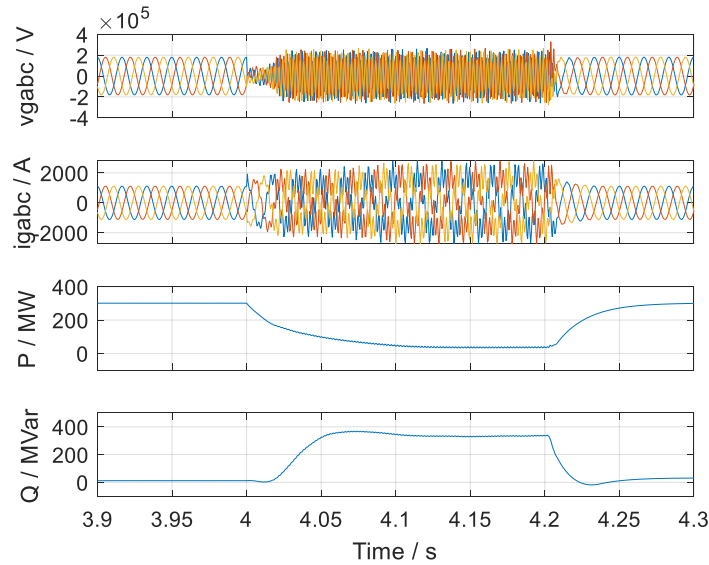


**Figure 3.12 – The MARS grid-side measured three-phase voltages and currents, active and reactive powers.**

**Grid event 2: Line to line Fault.** A line-to-line fault is simulated on the transmission line between the grid and the MARS at  $t = 8.0$  s with a fault duration of 0.2 s. After 0.2 s, the

fault is self-cleared. From Figure 3.13, it can be observed that reactive power is injected to provide voltage support. Thus, the MARS can provide continuity of operation successfully during the fault and operates in a stable mode of operation during post-fault conditions.

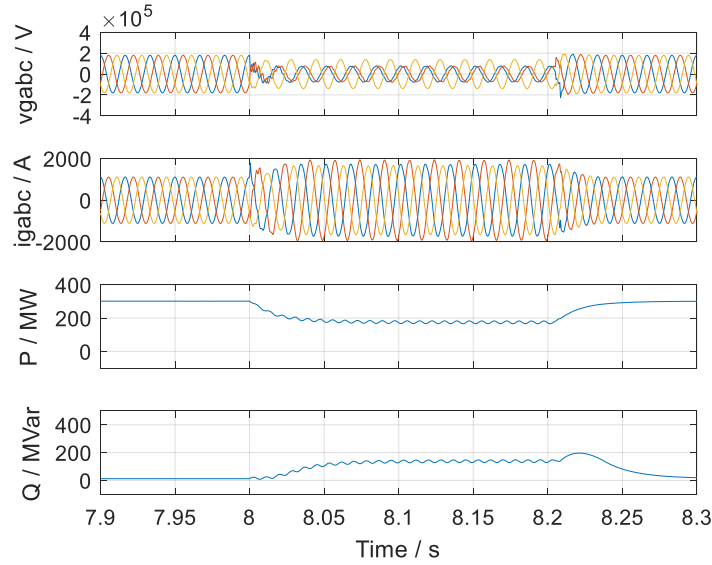


**Figure 3.13 – The MARS grid-side measured three-phase voltages and currents, active and reactive powers.**

**Grid event 3: 804.44 Loss of Generation.** An event of 804.44 MW loss of generation (LOG) in the WECC is created at  $t=12$ s. The frequency response measured at Pittsburg is shown in Figure 3.14. From Figure 3.15, it can be observed that reactive power is injected to provide frequency support. Thus, the MARS can provide continuity of operation successfully during the loss of generation event and operates in a stable mode during post-event conditions.

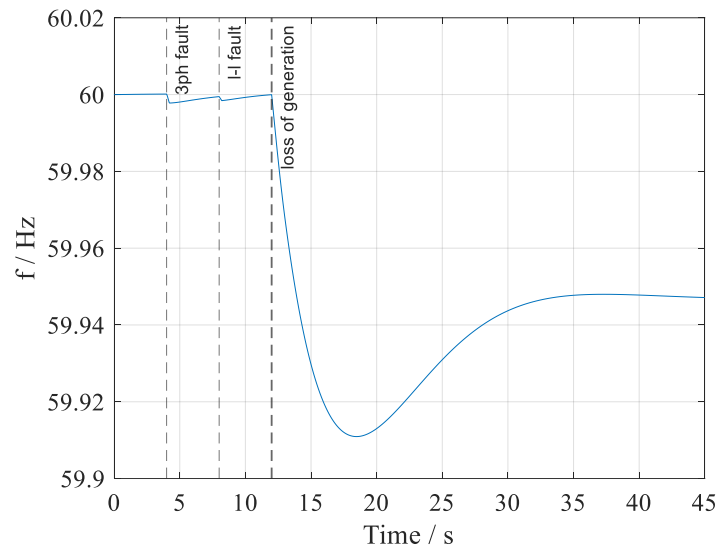


**Figure 3.14 – Ac-side grid frequency.**

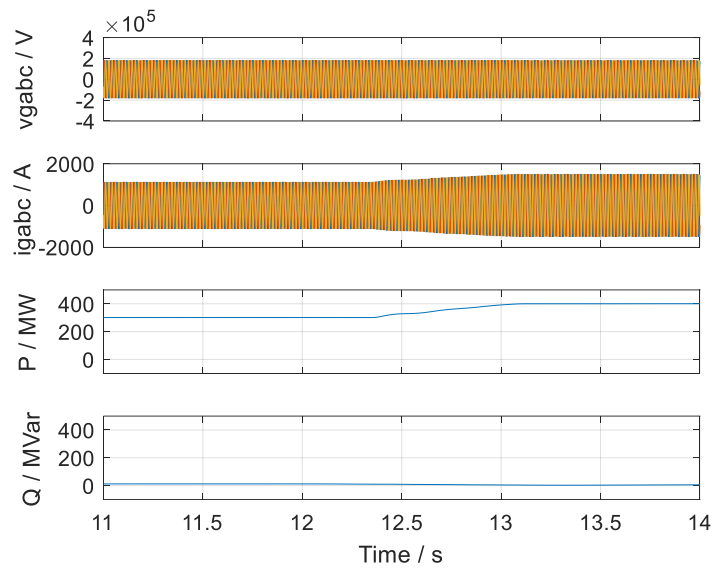


**Figure 3.15 – The MARS grid-side measured three-phase voltages and currents, and active and reactive powers.**

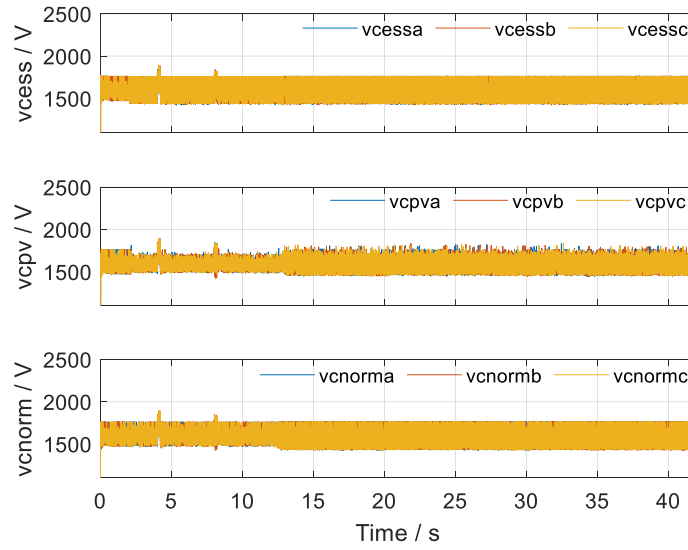


**Figure 3.16 – Capacitor voltages in the representative SMs subsequent to changes in the operating condition.**

The capacitor voltages of PV, ESS, and normal SMS are showcased in Figure 3.16. As shown, the capacitor voltages remain within the upper and lower voltage limit during all three grid events. The results of grid event tests demonstrate the robustness and stability of the hierarchical control with EBC. The ac-side currents remain to be sinusoidal and balanced without any instability issues. Similar tests were repeated under other operating conditions to examine the stability of the controller under arbitrary operating conditions and the system is observed to be stable under these different tested operating conditions.

### 3.5 Standard Compliance of the MARS

The cHIL tests are utilized to test the compliance of MARS with existing standards IEEE 1547-2018, IEEE 519-2014, and NERC PRC-024-3 about its capabilities to actively mitigate disturbances through voltage and frequency support. The detail of the test and the test results are illustrated in Appendix B. The results show MARS’s ability to provide

frequency and voltage support with improvement in frequency response and disturbance rejection.

### **3.6 Summary**

This chapter introduces the hierarchical control of the MARS and proposes a method to design the controller gains in the MARS control system. The multivariable system is decoupled using a recursive reduced-order and boundary layer system approach. The L1, L2, and L3 controller parameters can be calculated based on this approach. The EBC originated from [21] has been accommodated for the design of the MARS by neglecting the negative sequence. Results for the cyclic test were validated with pre-defined performance criteria using PSCAD/EMTDC high-fidelity model and showcased the stable operation during steady state and step change of operating conditions. The system's dynamic response under different grid events is also presented, indicating the robustness of the MARS under faults or loss of generation in the WECC system connected to the MARS; and the cHIL tests for standard compliance of MARS were experimentally performed with hierarchical control.



## CHAPTER 4. MACHINE LEARNING-BASED EBC CRITERIA OF THE MARS

In the previous chapter, we introduced the benchmark hierarchical three-level control of the MARS. However, the EBC solves the SM capacitor voltage disparity by injecting a fundamental circulating current, which increases the switching frequency and thus increases the system loss. In addition, considering operating conditions viable for the system without the EBC, EBC criteria are proposed to enable the EBC only when necessary. The first step of implementing the EBC is determining the operation region, or in other words, the stability boundary of the MARS. However, obtaining the system boundary through mathematical analysis is not trivial due to the complexity of the MARS system. Thus, a data-driven method of EBC is proposed in this chapter.

### 4.1 Dynamics of the Capacitor SM Voltage Differences

In this section, the dynamics of capacitor voltage differences ( $\sum(V_{c\sigma})^2$ ) is studied. Therefore, the SM capacitor voltages here cannot be assumed to be balanced. Let  $S_{y,i,j}$  be the switching function of the  $i$ th SM in phase  $j$  ( $j=a,b,c$ ), where  $y$  represents the upper or lower arm. Therefore, the arm voltage is  $v_{y,j} = \sum_{i=1}^N S_{y,i,j} v_{c,y,i,j}$ .

The dynamic of each SM capacitor voltage is as follows:

$$C_{sm} \frac{dv_{c,y,i,j}}{dt} = i_{y,j} S_{y,i,j} + i_{pv,i} + i_{ess,i} \quad (4.1)$$

where,

$$i_{pv,i} = \begin{cases} \frac{P_{pv,i}}{v_{c,y,i,j}} & (\text{for } PV \text{ SM}) \\ 0 & (\text{for other SMs}) \end{cases} \quad i_{ess,i} = \begin{cases} \frac{P_{ess,i}}{v_{c,y,i,j}} & (\text{for } ESS \text{ SM}) \\ 0 & (\text{for other SM}) \end{cases}$$

Combined with (4.1), the SM capacitor voltage difference  $\sum (V_{c\sigma})^2$  defined in (3.7) can be expressed by:

$$\begin{aligned} \sum (V_{c\sigma})^2 = & \sum_{i=1}^N v_{c,p,i,a}^2 - \frac{v_{p,a}^2}{N} + \sum_{i=1}^N v_{c,n,i,a}^2 - \frac{v_{n,a}^2}{N} + \dots \\ & + \sum_{i=1}^N v_{c,n,i,c}^2 - \frac{v_{n,c}^2}{N} \end{aligned} \quad (4.2)$$

Based on (4.2), the dynamics of the square of each individual SM capacitor voltage is derived as:

$$\begin{aligned} C_{sm} \frac{dv_{c,y,i,j}^2}{dt} &= 2C_{sm} v_{c,y,i,j} \frac{dv_{c,y,i,j}}{dt} \\ &= 2v_{c,y,i,j} i_{y,j} S_{y,i,j} + 2v_{c,y,i,j} i_{pv,i} + 2v_{c,y,i,j} i_{ess,i} \end{aligned} \quad (4.3)$$

Assuming that SM capacitor voltages are balanced for each type of SM, the sum of square of capacitor voltages in one arm is expressed by:

$$\begin{aligned} \sum_{i=1}^N \frac{dv_{c,y,i,j}^2}{dt} &= \sum_{i=1}^{N_{normal}} \frac{dv_{cnormal,y,i,j}^2}{dt} + \sum_{i=N_{normal}+1}^{N_{normal}+N_{pv}} \frac{dv_{cpv,y,i,j}^2}{dt} \\ &+ \sum_{i=N_{normal}+N_{pv}+1}^N \frac{dv_{cess,y,i,j}^2}{dt} \end{aligned} \quad (4.4)$$

$$= \frac{2}{C_{sm}} i_{y,j} \sum_{i=1}^N S_{y,i,j} v_{c,y,i,j} + \frac{2}{C_{sm}} P_{pv} + \frac{2}{C_{sm}} P_{ess}$$

The dynamics of  $v_{y,j}^2$  is:

$$\begin{aligned} \frac{dv_{y,j}^2}{dt} &= 2v_{y,j} \frac{dv_{y,j}}{dt} \\ &= \frac{2}{C_{sm}} v_{y,j} i_{y,j} \sum_{i=1}^N S_{y,i,j} + \frac{2}{C_{sm}} v_{p,a} \frac{P_{pv} N_{pv}}{v_{cpv,y,i,j}} \\ &\quad + \frac{2}{C_{sm}} v_{p,a} \frac{P_{ess} N_{ess}}{v_{cess,y,i,j}} \end{aligned} \tag{4.5}$$

Combining (4.2)-(4.5), the dynamic model of  $\sum(V_{c\sigma})^2$  can be simplified as

$$\begin{aligned} \sum (V_{c\sigma})^2 &= \sum_{\substack{y=p,n \\ j=a,b,c}} \frac{2}{C_{sm}} (i_{y,j} v_{y,j} - i_{y,j} \sum_{i=1}^N S_{y,i,j} v_{c,y,i,j} + P_{pv} \\ &\quad - \frac{P_{pv} v_{p,a} N_{pv}}{v_{p,a,pv}} + P_{ess} - \frac{P_{ess} v_{p,a} N_{ess}}{v_{p,a,ess}}) \end{aligned} \tag{4.6}$$

The switching status increases the complexity of the formulation. Thus, mapping the relationship between  $\sum(V_{c\sigma})^2$  and  $P_{ac}$ ,  $Q_{ac}$ ,  $P_{dc}$  becomes challenging and time-consuming.

## 4.2 EBC Criteria

In practice, the presence of the circulating currents leads to increased current stress on the components, the magnitude of the SM capacitor voltage fluctuation, and the conduction losses, and need to be suppressed. Therefore, a criterion to disable or enable

the EBC control based on whether the system is capable of maintaining intra-arm power balance by itself is desired. The detailed of the proposed EBC criteria are presented and depicted in Figure 4.1.

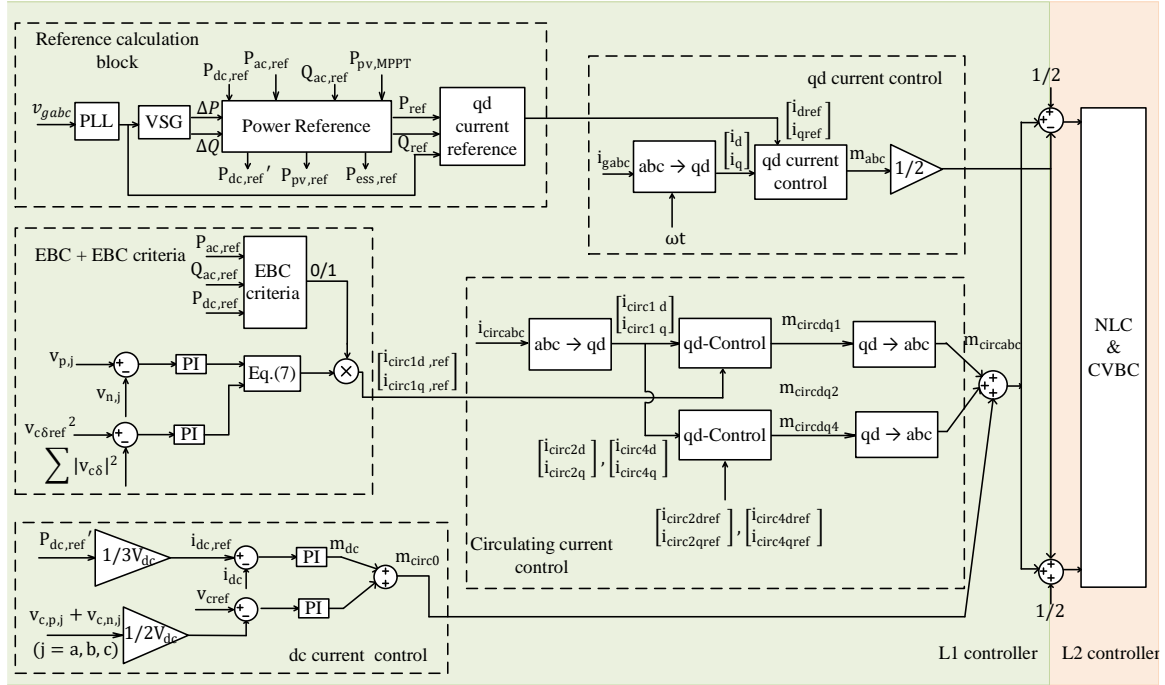


**Figure 4.1 – Block Diagram of L1 and L2 controllers with EBC criteria.**

#### 4.2.1 Impact of Capacitor Voltage Balancing Algorithms

Apart from the intrinsic parameters such as the SM capacitance, which will affect the power charging/discharging capability, the sorting efficiency also critically influences the power disparity limit and cannot be neglected when analyzing the EBC criteria. However, the existing literature discussing the inherent operational constraints of the MMC converter rarely considers the switching frequency and assumes it is ideal. The importance of sorting efficiency is examined in this section.

Different capacitor voltage balancing algorithms have been proposed in the literature aiming at improving the sorting efficiency (reducing the computational burden and thus simulation time) while maintaining a low switching frequency. To highlight the relationship between the capacitor voltage balancing algorithms and the operating region of the system, a conventional capacitor voltage balancing algorithm in [8], [82] is simulated with different sorting frequencies. The simulation time step is set at  $h$  while different sorting frequencies of  $h$ ,  $10h$ ,  $16h$ , and  $20h$  are compared (any limit on the maximum switching frequency of the switches is neglected here). The relationship between the sorting frequency and the stable operating condition ratio is shown in Figure 4.2. It is evident that the sorting frequency is positively correlated with the percentage of stable operating conditions. Consequently, the derivation of the operation boundary needs to consider the capacitor voltage balancing algorithm used.

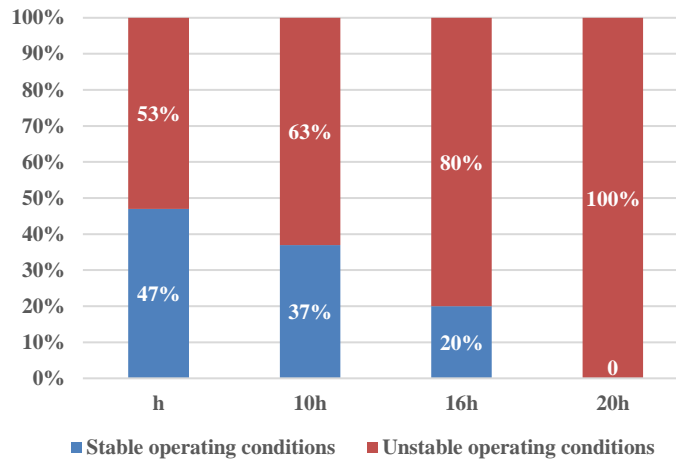


**Figure 4.2 – Ratio of stable operating conditions and unstable operating conditions vs sorting frequency of capacitor voltage balancing algorithm**

Analysis of the sorting process through analytical derivation is not trivial due to its nonlinearity. To avoid complicated analytical computation for mapping  $(V_{c\sigma})^2$  to the EBC

criteria, machine learning algorithms such as the random forest and NN pattern recognition are introduced to map between the stability of the operating condition with the input dc power and ac active/reactive powers.

#### 4.2.2 *ML-Based EBC Criteria*

The implementation of the EBC criteria requires a non-linear classifier, thus, the logistic regression and support vector machines are not suitable for the application. Other widely used non-linear classifiers such as k-nearest-neighbors and decision tree have considerable running time or relatively low accuracy respectively. Therefore, this thesis compares the implementation of the EBC criteria with the RF and ANN. Both ANN and RF perform much better than the traditional method and have fast running time. As shown later in this section, ANN performs slightly better than the RF.

##### 4.2.2.1 Data Acquisition

The data is extracted from the simulation of the MARS high-fidelity model developed in [70]. With the high-fidelity model, the improvement of the simulation speed is 18,000 times as compared to the model built based upon PSCAD/EMTDC library. The 4 s simulation time duration for each run only needs to take about 10 mins for this system with 250 SMs per arm. In the simulation, the input parameters  $P_{ac}$ ,  $P_{dc}$  and  $Q_{ac}$  are swept from [-400, 400] MW, [-400, 400] MW, and [-300, 300] MVar, respectively, and are restricted by  $P_{pv\_mppt}$ ,  $P_{ess\_rating}$  and Pmars\_calculation block. For the sake of simplicity,  $P_{pv\_mppt}$  is considered as a fixed value. The total number of operating conditions considered as the sample data is 6158, which all are divided into three different types of samples: training samples (70%), validation samples (15%), and testing samples (15%).

The MATLAB neural pattern recognition toolbox performs the training process using the scaled conjugate gradient backpropagation. And the well-tuned network is compiled to the MATLAB function and applied with the high-fidelity model in the PSCAD through the MATLAB-PSCAD interface.

The stability of all 6158 simulated operating conditions is visualized in the graph of Figure 4.3, in which the operating conditions with positive dc active power and positive high ac active power are more prone to be stable. The operating conditions with non-zero ac reactive also help with the stability. The results coincide with the previous analysis since positive  $P_{dc}$  and highly positive  $P_{ac}$  lead to a higher arm current and can increase the charging and discharging capability of each SM capacitor, thus improving the system's stability. Figure 4.3 also shows the nonlinearity between the input and the output of the EBC criteria and justifies using the machine learning algorithms as an optimal way to map the input and the output.

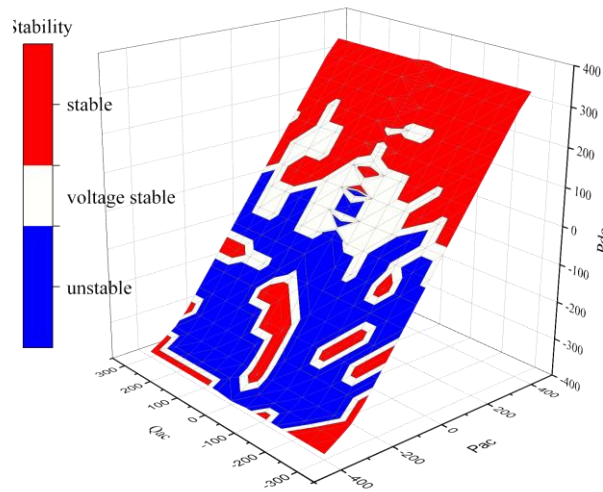


**Figure 4.3 – Visualization of the stability for all 6158 operating conditions.**

#### 4.2.2.2 Random Forest Based EBC Criteria

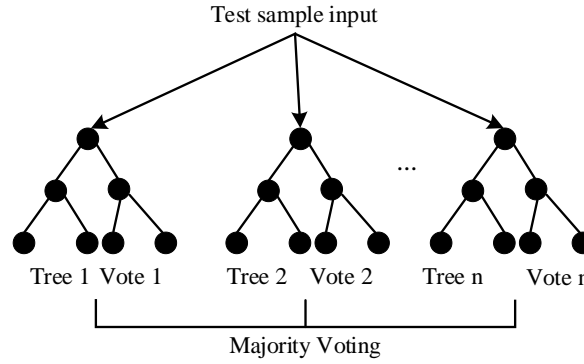


**Figure 4.4 – Random Forest algorithm.**

The RF algorithm shown in Figure 4.4 is a group of decision trees that operate as an ensemble and is used here for the classification and judgment of the EBC necessity; each decision tree will give a class prediction where the class with the highest votes will be the final classification result. The parameters of the RF are tuned to avoid overfitting and to get optimal accuracy. The optimal number of estimators is 7, the max depth is 8, and the max features are 3. With 70% of the data used for training, 15% used for validation, and 15% for testing, two evaluation metrics have been used to compute the accuracy of the RF algorithm. The accuracy score gives 96.37% testing accuracy, the Area Under the Receiver Operating Characteristic Curve score (ROC AUC score) for testing is 95.93%, and the testing accuracy of the confusion matrix is around 96.05%. The ROC is the curve having False Positive Rate on the x-axis and True Positive Rate on the y-axis at all classification thresholds. In order to get one number that quantifies how suitable the curve is, one can calculate the Area Under the ROC Curve or ROC AUC score.

The RF algorithm is able to provide the feature importance (variable importance), which describes the relevance of each feature to the output. The most informative feature shown in Figure 4.5 is  $P_{dc}$ . This validates the analysis in chapter 3.1.3, i.e., the instability



is prone to happen when  $P_{dc}$  is small, thereby leading to low arm current as the charging/discharging capability of each SM capacitor will be weakened under these circumstances.  $Q_{ac}$  is the second important variable in Figure 4.5, indicating that increasing  $Q_{ac}$  can usually help reducing the SM capacitor voltage disparity.

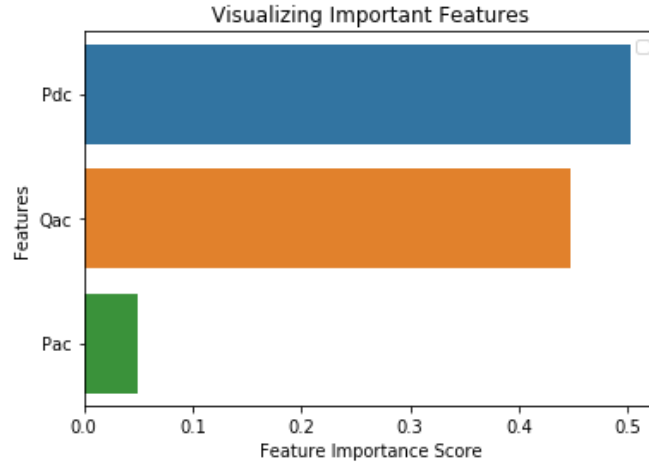


**Figure 4.5 – Feature importance.**

#### 4.2.2.3 ANN-Based EBC Criteria

It is known that NNs can be used to recognize patterns. Thus, the network can be trained to predict future behavior based on past information. Through trial and error, the model used in this thesis is constructed by a 2-layers forward network with a sigmoid activation function (4.7) and softmax activation function (4.8) in the output layer. Nine neurons are the optimal number considered in the hidden layer by running through multiple numbers of neurons. The network is trained using scaled conjugate gradient backpropagation and depicted in Figure 4.6.

$$S(x) = \frac{1}{1 + e^{-x}} \quad (4.7)$$

$$\sigma(z)_i = \frac{e^{z_i}}{\sum_{j=1}^K e^{z_j}} \text{ for } i = 1, \dots, K \text{ and } z = (z_1, \dots, z_K) \in \mathbb{R}^K \quad (4.8)$$

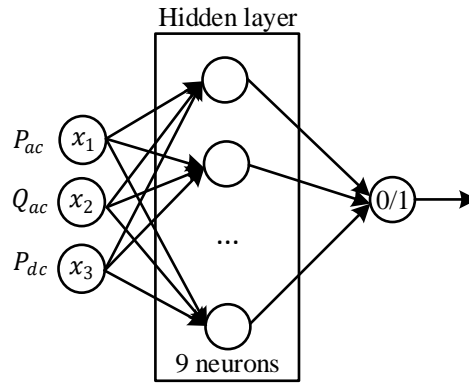


Figure 4.6 – Diagram of ANN algorithm.

Output Class	0	1	Total
	2452 56.9%	66 1.5%	97.4% 2.6%
1	55 1.3%	1736 40.3%	96.9% 3.1%
Total	97.8% 2.2%	96.3% 3.7%	97.2% 2.8%
	0	1	Total
	Target Class		

Output Class	0	1	Total
	536 58.0%	20 2.2%	96.4% 3.6%
1	11 1.2%	357 38.6%	97.0% 3.0%
Total	98.0% 2.0%	94.7% 5.3%	96.6% 3.4%
	0	1	Total
	Target Class		

Output Class	0	1	Total
	539 58.3%	17 1.8%	96.9% 3.1%
1	15 1.6%	353 38.2%	95.9% 4.1%
Total	97.3% 2.7%	95.4% 4.6%	96.5% 3.5%
	0	1	Total
	Target Class		

Output Class	0	1	Total
	3527 57.3%	103 1.7%	97.2% 2.8%
1	81 1.3%	2446 39.7%	96.8% 3.2%
Total	97.8% 2.2%	96.0% 4.0%	97.0% 3.0%
	0	1	Total
	Target Class		

Figure 4.7 – Confusion matrix of ANN training.

The confusion matrix from Figure 4.7 shows the number of cases that were correctly classified in the diagonal green cells, and the off-diagonal red cells show the misclassified cases. The number in the grey diagonal cells indicates a 97.2% training accuracy, 96.6% of validation accuracy, and testing accuracy of 96.5%. The results show very good recognition.

#### 4.2.2.4 Comparison of Two Proposed ML algorithms

Both RF and ANN algorithms train their models offline. The RF requires the parameter tuning of  $N_{estimators}$ , max-depth, and max-features by sweeping those parameters and using evaluation metrics to find the optimum number of each parameter. As for the ANN, the number of layers and the number of neurons, activation function, and learning rate are the parameters that need to be determined before training the network for the optimum weighing factors. Assisted by the MATLAB toolbox, training the NN is much easier than tuning the RF parameters, which is an advantage of using the NN. The utilization of the RF and ANN algorithms in the cHIL is compared in Table 4.1. Compared with no EBC criteria test cases, the increase in CPU utilization for adding the RF and ANN algorithm is negligible, and the difference between the RF and ANN is also small. Thus, the only difference is the accuracy. The overall accuracy of the NN is higher than the RF accuracy as shown in Table 4.2. The details of the benchmark method in Table 4.2 is illustrated in Algorithm 1, and it is a simple user-defined if-else statement. The value of  $P_{ac\_limit}$  and  $P_{dc\_limit}$  used in the benchmark method is obtained through pattern recognition from the data generated under various operating conditions. Even though the statement is summarized from 2500 data points, which is less than the data point used to train the machine learning algorithms, it gives the least accurate results of 80.57% which

is far lower than the accuracy of the RF and ANN. The NN also has the advantage of the trained model that is easier to compile with the MATLAB Simulink model using the MATLAB nprtool. The compiled model is then integrated with both the PSCAD high-fidelity model and the real-time simulation model.

---

Algorithm 1: EBC criteria benchmark method	
1.	<b>If</b> $P_{ac} > P_{ac\_limit}$ and $P_{dc} > P_{dc\_limit}$
2.	Disactivate EBC
3.	<b>end If</b>

---

**Table 4.1 – Utilization in real-time simulation**

	w/o EBC criteria	RF	ANN
Utilization	12.7%	13.4%	13.2%

**Table 4.2 – Testing accuracy of the confusion matrix**

	Benchmark method	RF	ANN
Accuracy	80.57%	96.05%	96.5%

### 4.3 Simulation Results

The MARS system, with its parameters listed in Table 4.3, is an upgrade based on the Trans Bay Cable project in Pittsburg, California [80]. Since the power loss calculation block is implemented using PSCAD/EMTDC, the high-fidelity model of MARS introduced in chapter 2 is used for the simulation. The communication delay is considered when modeling so that the simulation results are congruent with their cHIL results.

**Table 4.3 – The MARS system parameters.**

System Parameters	Value
Simulation time-step	60 $\mu$ s
System capacity (base power rating)	400 MVA
System frequency	60 Hz
dc link voltage	$\pm 200$ kV
ac terminal voltage	220 kV
Arm inductor	30 mH
Front-end half-bridge capacitor	7.7 mF
Front-end half-bridge capacitor voltage	1.6 kV
Number of PV-SMs/arm	111
Number of ESS-SMs/arm	37
Number of Normal-SMs/Arm	102
Total number of SMs/Arm	250

One main advantage of introducing the EBC criteria is reducing the losses, so the power losses of 2500 operating conditions with and without EBC criteria are calculated online and compared to validate the performance. The power loss is calculated using the real-time analytical calculation model and is not discussed in this thesis. The average switching frequency of the MARS system with and without the EBC criteria is also compared since the switching frequency reduction leads to a decrease in power losses. The loss calculation of MARS is embedded in the real-time simulation. For each specified time period of 100h ( $h=4\mu$ s is the simulation time step) in each time-step, based on the current status of the MOSFET and the diode, the turned-on or turned-off losses or the conduction losses will be calculated and added up with the turned-on or turned-off losses or the conduction losses at previous time-steps. The calculation of the SM capacitor voltage is using a similar manner. In this specified time period, the power loss calculation for arm

inductor, including the inductor winding loss and the core loss, is also performed using real-time arm current waveform. The switching power losses, conduction power loss, capacitor power loss, and the inductor power loss over the 100h time period can be calculated, and when those power losses reach steady state, they will be our final value of power losses under this operating condition.

Out of the 2500 operating conditions, 1,396 of them require a turn-on EBC to meet the designed stability constraints. Thus, for those operating conditions, the power loss and switching frequency w/wo EBC criteria have no difference. The loss reduction percentage  $(P_{loss}^{with\ EBC\ criteria} - P_{loss}^{without\ EBC\ criteria}) / P_{loss}^{with\ EBC\ criteria} * 100\%$  and the frequency reduction percentage  $(f_{avg}^{with\ EBC\ criteria} - f_{avg}^{without\ EBC\ criteria}) / f_{avg}^{with\ EBC\ criteria} * 100\%$  of the rest 1104 operating conditions are listed in Figure 4.8. With the EBC criteria, the operating conditions within the operation boundary do not have injected circulating current, which in turn results in less power loss. Table 4.4 illustrates some statistics of the switching frequency reduction  $(f_{avg}^{with\ EBC\ criteria} - f_{avg}^{without\ EBC\ criteria})$  and the power loss reduction  $(P_{loss}^{with\ EBC\ criteria} - P_{loss}^{without\ EBC\ criteria})$ . It can be observed that the total power saved for all 1104 test cases is significant and has an average power loss reduction of 550kW, the results validate the importance of the EBC criteria.

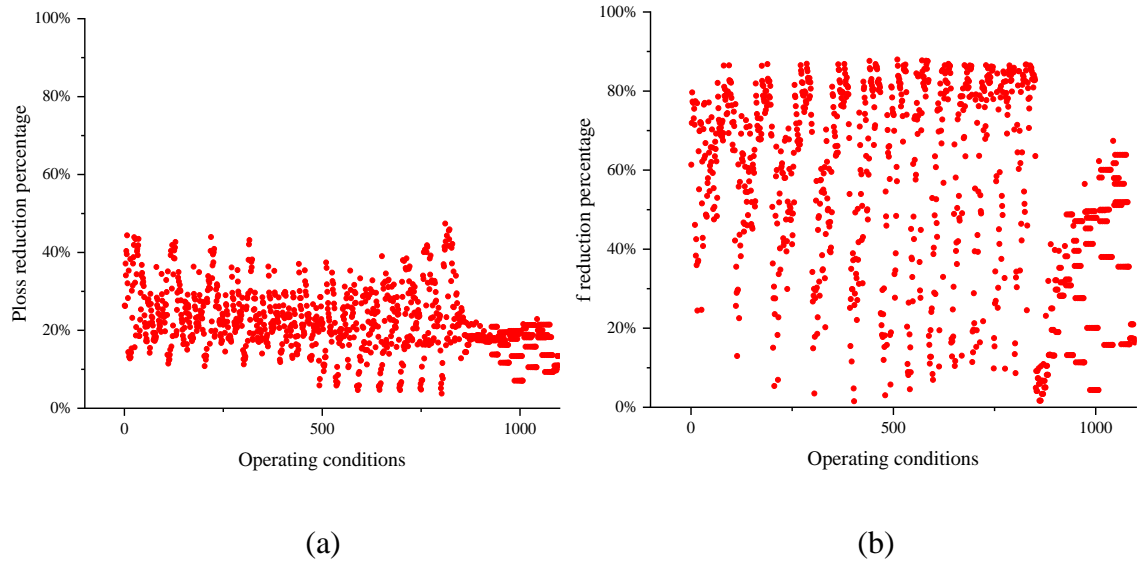


**Figure 4.8 – (a) Ploss reduction percentage for 1104 operating conditions (b) The average frequency reduction percentage for 1104 operating conditions.**

**Table 4.4 – Statistics of the data w/wo EBC criteria.**

	Switching frequency reduction (Hz)	Power loss reduction (W)
Average	356	550,319
Medium	227	489,870
Maximum	1,376	1,582,270
Minimum	2	91,415
Standard derivation	328	306,060

## 4.4 cHIL Results

### 4.4.1 cHIL System Setup

The MARS cHIL platform is developed using MARS control system connected to a real-time simulator. As shown in Figure 4.9, the MARS, including the front-end half-bridge

converter, along with the normal, PV, and ESS SMs and their L3 controllers are implemented in the Xilinx Virtex-7 FPGA of OPAL-RT's OP5707 platform while the ac grid model is implemented in the CPU of OP5707. This forms the real-time simulator. The ac grid model of MARS is based on the high-fidelity electromagnetic transient (EMT) model of the grid developed in [83]. The MARS control platform consists of L2 controller implemented in FPGA and the L1 controller in CPU. A large number of signals needs to be exchanged between the real-time simulator and the control platform. The small form-factor pluggable (SFP) communication medium is used to transfer the voltage and power references of the L3 controller from L1 controller in the control platform and mapping the data between the real-time simulation of the dynamics of MARS hardware and the control platform. To send the grid measurements from the real-time simulator to the control platform, the copper I/Os are utilized to replicate the real-world communication. The different modes of data exchange are designed according to the signal size and latencies. The real-time simulator and the control platform as well as the communication cables are displayed in Figure 4.10.

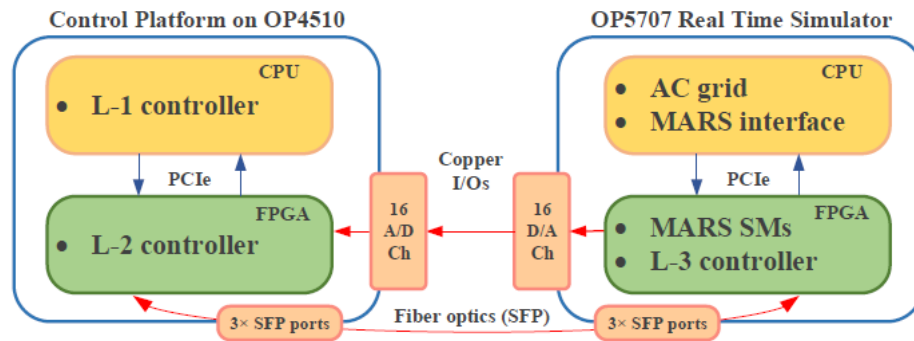


**Figure 4.9 – Diagram for cHIL system setup.**



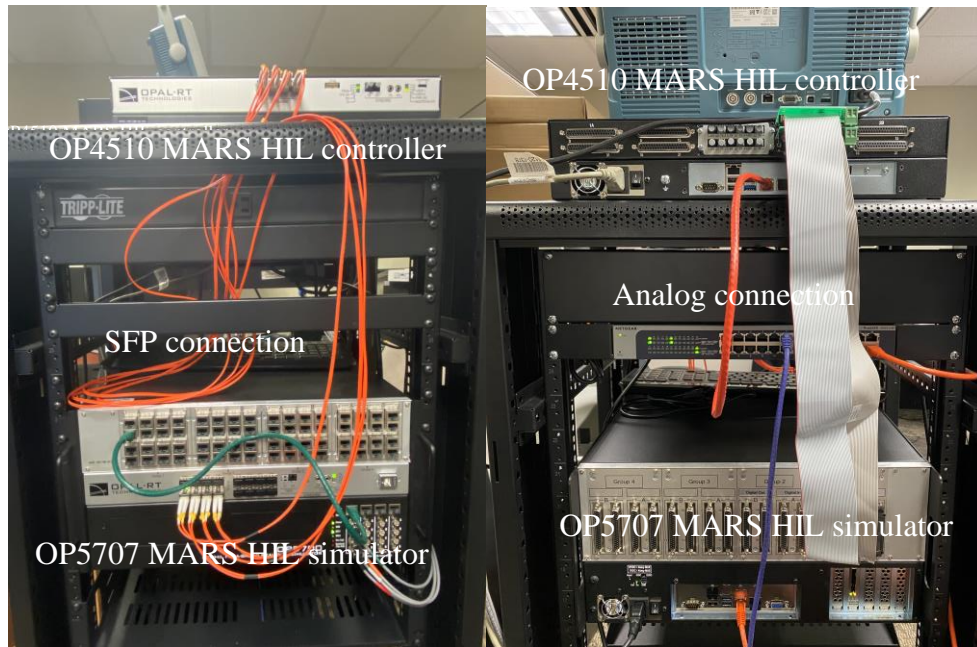


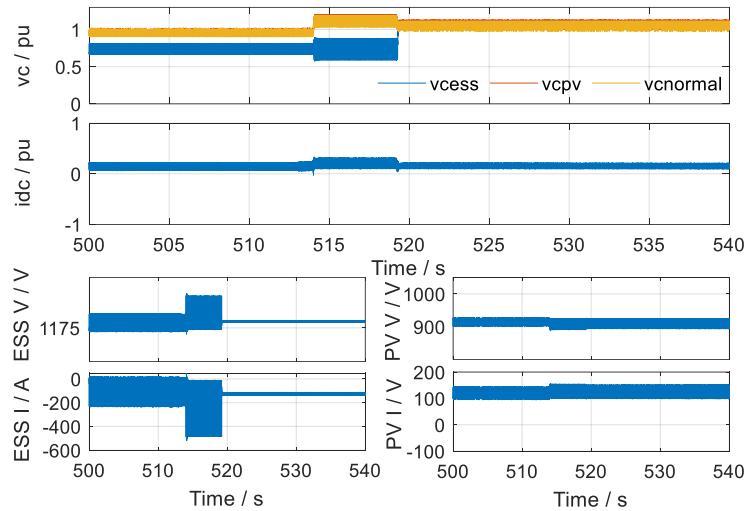
**Figure 4.10 – Connection set up for OP4510 and OP5707 (a) Front-side connection; (b) Back-side connection.**

#### 4.4.2 *cHIL Test Results*

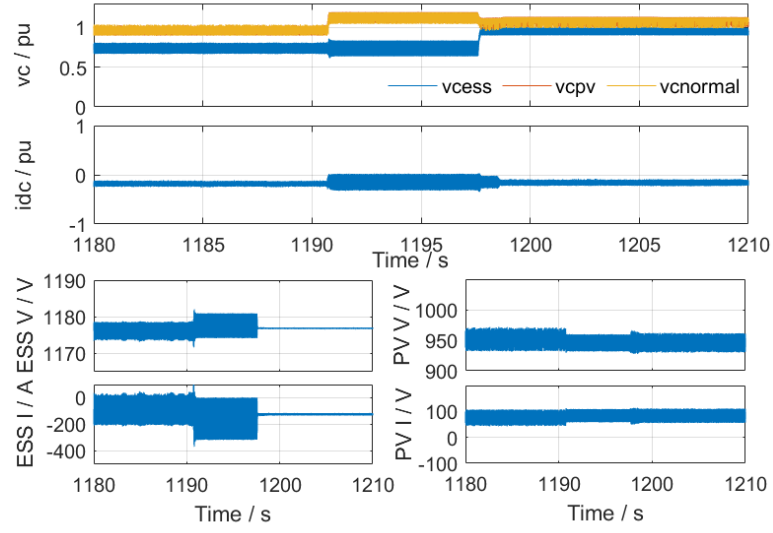
##### 4.4.2.1 EBC Transition from Enabled to Disabled Under Unstable Operating Condition.

In this case study, the MARS real-time simulation model is executed initially without the EBC criteria. Subsequently, the EBC criteria are activated under multiple unstable operating conditions. The presented results are per unitized with the system base power rating of 400 MW and the base L-L voltage of 220 kV. The results for the first operating condition are shown in Figure 4.11 (a), where the dispatch ac-side power command is 100 MW active power, 0 reactive power, and 60 MW dc power. The PV and ESS dc-dc converters are enabled and connected to the MARS system with a PV reference voltage of 810 V and ESS reference discharging power of -150 kW. It can also be observed from Figure 4.11 (a) that the SM front-end half-bridge capacitor voltages are initially unbalanced

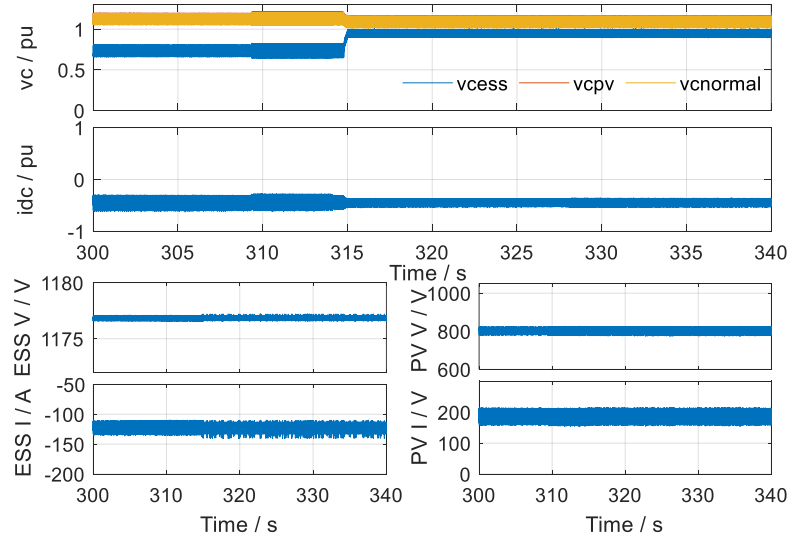
and lie outside the specified range of 1.36 kV to 1.84 kV ( $\pm 15\%$  of front-end half-bridge capacitor nominal voltage). The unbalanced SM capacitor voltages cause instability for the L3 ESS controller. However, the SM capacitor voltages become stable after enabling EBC, showcasing the successful operation of the EBC. The results for the second operating condition are shown in Figure 4.11 (b), in which a negative power reference is sent to the MARS, and the capacitor voltage disparity happens. However, the EBC effectively brings the ESS capacitor voltage back within the limit range. The third operating condition has a non-zero reactive power reference, which happens when the MARS is required to provide grid support. Similar to the previous two operating conditions, the EBC is functioning well under this operating condition and can help maintain the balanced capacitor voltages among different types of SMs.



(a)



(b)

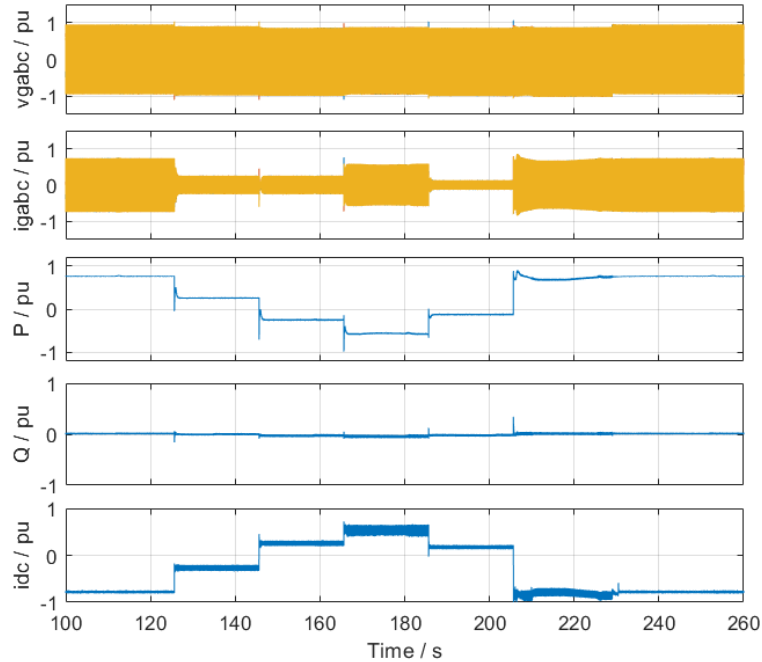


(c)

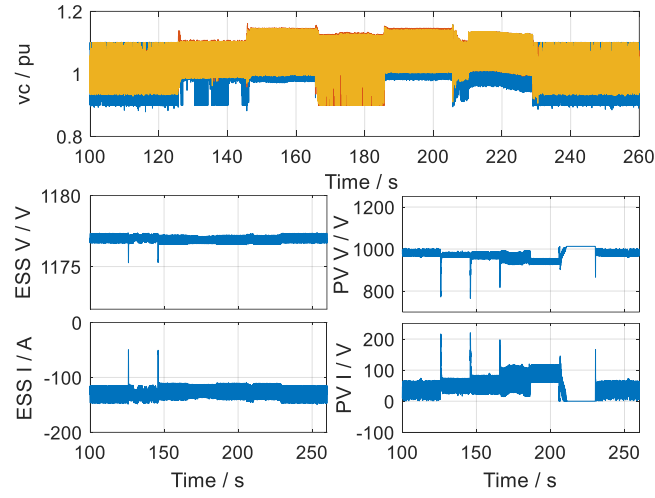
**Figure 4.11 – Capacitor voltages in representative SMs subsequent to changes in the EBC criteria; ESS and PV side capacitor voltages and inductor current under three operating conditions in which capacitor voltage balancing cannot be maintained without the EBC. (a)  $P_{ac}=100$   $P_{dc}=60$   $Q_{ac}=0$ ; (b)  $P_{ac}=-100$   $P_{dc}=-170$   $Q_{ac}=0$ ; (c)  $P_{ac}=-150$   $P_{dc}=-220$   $Q_{ac}=50$ .**

#### 4.4.2.2 Operating Condition Changes When EBC Criteria are Presented.

This case study presents the results of the cyclic test of different steady-state operating conditions with the NN-based EBC criteria included in the control. The dispatch command steps form  $P_{ac}=300\text{MW}$   $Q_{ac}=0$   $P_{dc}=300\text{MW}$  (EBC disabled by EBC criteria) to  $P_{ac}=150\text{MW}$   $Q_{ac}=200\text{MVar}$   $P_{dc}=150\text{MW}$  (EBC enabled by EBC criteria),  $P_{ac}=100\text{MW}$   $Q_{ac}=-50\text{MVar}$   $P_{dc}=60\text{MW}$  (EBC enabled by EBC criteria),  $P_{ac}=-50\text{MW}$   $Q_{ac}=0$   $P_{dc}=-74\text{MW}$  (EBC enabled by EBC criteria), and  $P_{ac}=-300\text{MW}$   $Q_{ac}=0$   $P_{dc}=-300\text{MW}$  (EBC enabled by EBC criteria) and back to the first operating conditions. The simulation results shown in Figure 4.12 indicate that the system remains stable during the operating condition changes; in addition, the transition is fast and with acceptable overshoot. The real-time results, as shown in Figure 4.12 (b) indicate that the PV and ESS dc-dc converter work as expected under the new set of dispatch ac-side power commands, and the SM's front-end half-bridge capacitor voltages are balanced in the required range which shows the successful operation of the hierarchical controller.



(a)



(b)

**Figure 4.12 – (a) The MARS grid-side measured three-phase voltages and currents, active and reactive powers, and dc current. (b) Capacitor voltages in representative SMs subsequent to changes in operating condition; one PV and ESS converter outputs.**

#### 4.4.2.3 Impact of $P_{dc}$ to Capacitor Voltage Disparity in One Arm.

As discussed in Section 3.1.3,  $P_{dc}$  is an important factor that impacts the capacitor voltage disparity. Since  $i_{dc}$  is proportional to  $P_{dc}$ , larger values of  $P_{dc}$  lead to higher arm currents, thereby contributing to higher charging/discharging rates of the SM capacitors. This is demonstrated in Figure 4.13. The system is initially in operating condition  $P_{ac}=100$  MW,  $P_{dc}=60$  MW, and  $Q_{ac}=0$ , where the capacitor voltages of different types of SMs are not well balanced. Subsequent to changing  $P_{dc}$  command to 80 MW and 100 MW, the SM capacitor voltage differences for different types of SMs gradually reduce. However, increasing  $P_{dc}$  is not linearly related to the capacitor voltage disparity as  $P_{dc}$  is dependent

on  $P_{pv}$  and  $P_{ess}$ . Thus, different combinations of  $P_{pv}$  and  $P_{ess}$  will also affect the capacitor voltages.

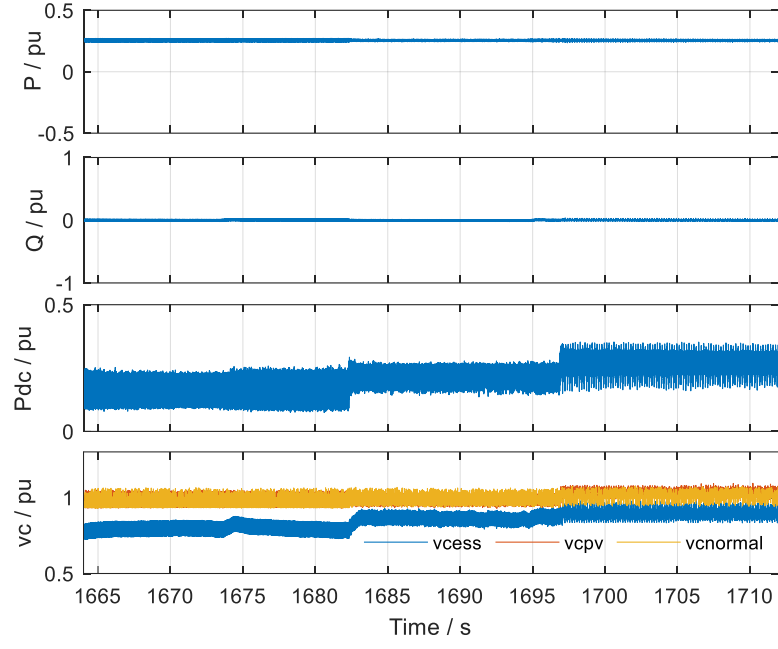


**Figure 4.13 – The MARS grid-side measured active and reactive powers, dc power, and capacitor voltages of different types of SMs.**

#### 4.4.2.4 Effect of $Q_{ac}$ to Capacitor Voltage Disparity in One Arm.

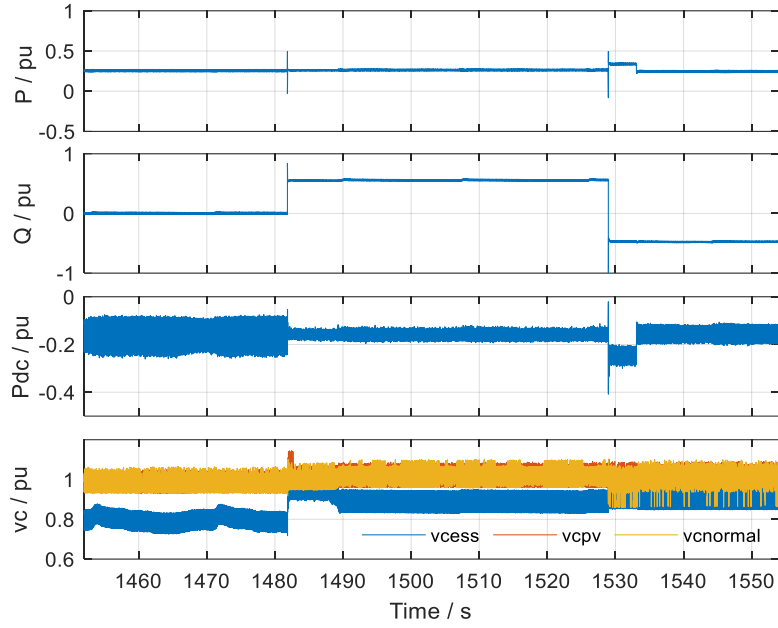


**Figure 4.14 – The MARS grid-side measured active and reactive powers, dc power, and capacitor voltages of different types of SMs.**

Reference [21] states that increasing the reactive power can help stabilize unstable operating conditions. Figure 4.14 showcase the impact of  $Q_{ac}$  on SM capacitor voltage disparity. The system is tested under constant  $P_{ac}=100$  MW with  $Q_{ac}$  stepping up from 0 to 200 MVar and subsequently to -200 MVar. The results in Fig. 18 show that the SM capacitor voltage balancing, i.e., intra-arm power balance, is improved with none-zero  $Q_{ac}$ . Different operating conditions are tested in which  $Q_{ac}$  has a positive effect on most of the cases. However, there are also some cases that do not follow this regulation.

## 4.5 Summary

In this chapter, the SM capacitor voltage disparity of a modular converter system with multiple external sources is discussed and explored. In such a system, the capacitor voltage disparity under some of the operating conditions originates from the limited capability of the capacitor voltage balancing algorithm, low dc power, and low reactive

power. This issue of capacitor voltage disparity is addressed by the EBC through injecting a fundamental circulating current. However, implementing the EBC introduces extra power losses and increases the switching frequency for the set of operating conditions that are viable for the system without the EBC. Thus, in this paper, the operation boundary of stable/unstable operating conditions is assessed by two machine learning algorithms. The machine learning algorithms can avoid complicated analytical derivation and achieve around 97% accuracy in determining whether the EBC is necessary under certain operating conditions. The RF and ANN algorithms are compared from training, utilization in cHIL test, and accuracy perspectives. The ANN algorithm outperforms the RF and is implemented in both the PSCAD software and cHIL platform.

The PSCAD/EMTDC simulation results showcase the power and switching frequency reduction obtained under 2500 operating conditions assisted by the EBC criteria. The cHIL tests demonstrate the capacitor voltage disparity under some operating conditions and how the operating condition becomes viable for the system by enabling the EBC. The mechanism of the capacitor voltage disparity has been further verified by the cHIL test and the relationships between the system stability, reactive power, and dc power are investigated. In addition, the cyclic test fully illustrates the stable operation of the system under different power references with the implementation of the EBC and the EBC criteria in the MARS control.

The proposed EBC method along with the EBC criteria are applicable to a modular converter system with any size in which a number of SMs in each arm are integrated with external power sources/inputs such as ESS, PV, etc., or a combination of them. With the



help of EBC, the operating region of the system can be extended while improved efficiency and reduced switching frequency can be achieved by implementing the EBC criteria.

## **CHAPTER 5. NN-BASED EBC OF THE MARS AND POWER MISMATCH ELIMINATION STRATEGY**

In the previous chapter, a PI-based EBC with EBC criteria is proposed to address the capacitor voltage disparity problem with improved power efficiency. However, due to the lack of mathematical basis, the traditional PI-based EBC is hard to justify the effectiveness or stability of its design parameters. Thus, tuning the PI gains requires thousands of simulations under various operating conditions to ensure the operating condition is stable with the set of gains used and, simultaneously, has a relatively low fundamental circulating current. In addition, the EBC criteria also require a large dataset to train the data-driven EBC criteria. Thus, an NN-based EBC is proposed in this chapter to simplify the design process and minimize the system loss. A power mismatch elimination strategy is also proposed to address the inter-phase and inter-arm power mismatch when partial shading happens.

The above-mentioned discussion underlies the need for developing simple, efficient, and easily generalizable control methods for a MARS-type system that integrates multiple power sources. To bridge this research gap, this thesis proposes an accurate and computationally efficient NN-based power mismatch elimination (NNPME) technique. The power mismatch elimination strategy is proposed to address the inter-phase and inter-arm power mismatch when PV partial shading happens. The NN trained offline acts as a surrogate model mapping the relationship between the circulating-current references and the SM capacitor voltage ripples once it learns the dynamics of the system. The proposed NN-based EBC calculates the circulating current reference according to the SM capacitor

voltage difference and the arm capacitor voltage mismatch. The L1 control in hierarchical control with NN-based EBC is depicted in Figure 5.1.

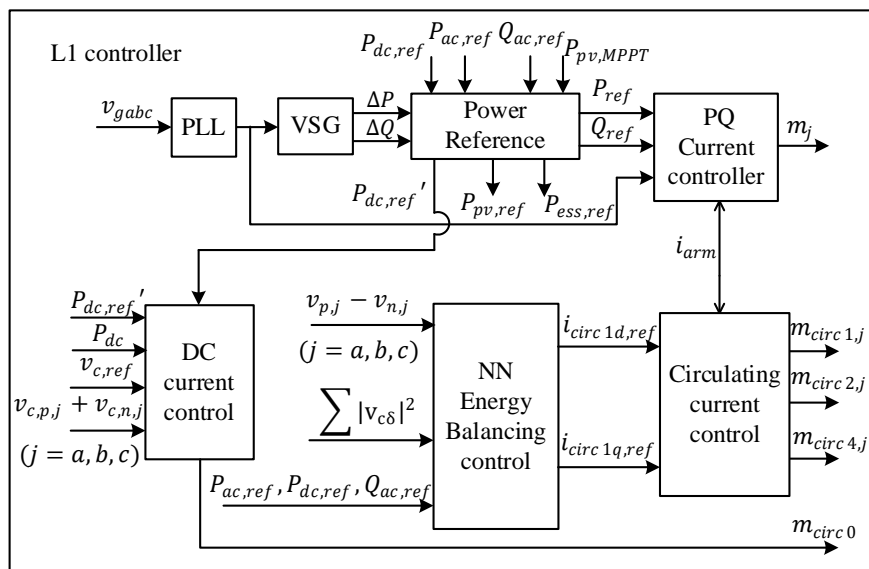


**Figure 5.1 – L1 controller diagram with NN EBC.**

## 5.1 Power Mismatch Elimination Strategy of the MARS

The existence of multiple PV panels in the MARS PV SMs increases the risk of power imbalance. The power imbalance may arise from different power being generated by PV connected to each PV SM in the MARS that may arise as a result of partial shading in the plant or a few faulty panels. In the case of partial shading, the shaded PV SMs may cause power imbalance between different PV SMs within an arm, between different arms, or even between different phase legs. The different types of SMs (PV SMs, ESS SMs, normal SMs) in one arm are the inherent power imbalance source causing unbalanced capacitor voltages under various operating conditions. In order to handle the power mismatch that may occur not only between different types of SMs of one arm of the MARS

but also between the arms and the three-phase legs, the NNPM control strategy is proposed and analyzed

### 5.1.1 Inter-SM Power Mismatch Elimination

The three types of SMs in one arm, with different external power inputs, lead to inter-SM power mismatch in an arm. The SM capacitor voltage disparity is the major effect of inter-SM power mismatch under some operating conditions that have low or negative dc currents. The MARS-type systems with multiple energy power inputs to individual SMs may not have balanced capacitor voltages only by using a capacitor voltage balancing algorithm based on a sorting algorithm, which works in a conventional MMC. Similar to section 3.1.3.2, the upper and lower limits of the capacitor voltages are set based on the designed stability constraints. The lower limit is set to ensure the stable operation of the L3 controller due to the needs of the connected dc-dc converter. The upper limit is set to avoid the over-voltage stress on the switches. The operating conditions in which the SM capacitor voltages are within limits are considered stable. In addition to the voltage, the dc current ripple is also limited to less than 20% of the nominal current for stable operations. To ensure that an operating condition is stable, both capacitor voltage limit and dc current restriction should be simultaneously met. The capacitor voltage difference is quantified using  $\sum(V_{c\sigma})^2$ , and is defined in (3.7).

Analytical equations have been derived in the literature to model the dynamics of the capacitor voltage ripples. However, when analyzing the capacitor voltage differences, the assumption that capacitor voltages are balanced will not be valid, which increases the complexity of mapping the relationship between  $\sum(V_{c\sigma})^2$  and the circulating current. Thus,

the design of a PI-based EBC would not only be non-trivial; but also may not guarantee stable operation of the converter under all scenarios. This thesis proposed an NN-based EBC control to address such shortcomings.

### 5.1.2 Inter-Phase Power Mismatch Elimination

Differences in the power processed between the phases will affect the operation of the MARS and cause capacitor voltage disparity and distorted grid current. To solve this, the power reference generator in the L1 controller will rearrange the dc reference power for each phase (thereby generating a dc circulating current). The dc reference power will be fed to the dc current controller, forcing the dc circulating current to cancel the power mismatch effect and deliver balanced currents to meet the grid code requirements. In the meantime, the required dc circulating currents are minimized with the help of the ESS system, which increases the system efficiency while eliminating the power mismatch.

The basics of the power reference generator is illustrated in the flow chart of Figure 5.2. When  $\text{Avg}(P_{pv,MPPT,j})(k)$  becomes larger after shedding, the ac and dc power commands can be maintained. In addition, the PV power will be curtailed when  $\text{Avg}(P_{pv,MPPT,j})(k)$  is too large to be compensated by the ESS. When  $\text{Avg}(P_{pv,MPPT,j})(k)$  goes below  $\text{Avg}(P_{pv,MPPT,j})(k-1)$ , depending on the regulations of different grid markets, the MARS system will be controlled by the proposed power mismatch elimination algorithm and operated at (1) fixed  $P_{ac}$  mode; (2) fixed  $P_{dc}$  mode; (3) synergized proportional adjustment of  $P_{ac}$  and  $P_{dc}$  mode (SPA mode). The three algorithms are presented in Table 5.1. Assume that at  $t = t_1$ , the solar irradiation undergoes intermittent

changes due to partial cloud coverage over part of the PV plant. Subsequently, the phase power mismatch occurs and for phase  $j$  ( $j=a,b,c$ ), we have

$$\text{Avg}(P_{pv,MPPT,j})(k) \neq \text{Avg}(P_{pv,MPPT,j})(k-1) \quad (5.1)$$

where

$$\text{Avg}(P_{pv,MPPT,j})(k) = \frac{1}{3} \sum_{k=a,b,c} P_{pv,MPPT,j}(k)$$

The operation of the power reference generator can be summarized as follows

- 1) If  $\text{Avg}(P_{pv,MPPT,j})(k-1) \leq \text{Avg}(P_{pv,MPPT,j})(k) \leq \text{Avg}(P_{pv,MPPT,j})(k-1) + \text{Avg}(P_{ess,ref,j})(k-1) + P_{ess,rating}$ , the ac and dc power reference generation will remain the same. However, the internal dc circulating current and the ESS power will be used to compensate for the phase power mismatch.
- 2) If  $\text{Avg}(P_{pv,MPPT,j})(k) \geq \text{Avg}(P_{pv,MPPT,j})(k-1) + \text{Avg}(P_{ess,ref,j})(k-1) + P_{ess,rating}$ , the ESS power will not be capable of compensating for the increased PV power. Thus, the PV power will be curtailed to maintain the ac and dc power commands sent from the grid operator. The updated ESS and PV power reference for each phase are shown in Figure 5.2.
- 3) If  $\text{Avg}(P_{pv,MPPT,j})(k) \leq \text{Avg}(P_{pv,MPPT,j})(k-1)$ , the system may operate at fixed  $P_{ac}$  mode, fixed  $P_{dc}$  mode, or the mode that  $P_{ac}$  and  $P_{dc}$  will change proportionally. It can be observed from Table 5.1 that under all modes, the updated dc power reference will be sent to the dc-current controller, and a dc circulating current will be issued to transfer power between the phases. In

addition, the ESS will operate at its maximum capacity to minimize the required circulating current. The details of the dc-current control are discussed in chapter 3.1. The active power reference, ESS power reference for each phase, and the dc reference power are updated and shown in Table 5.1.

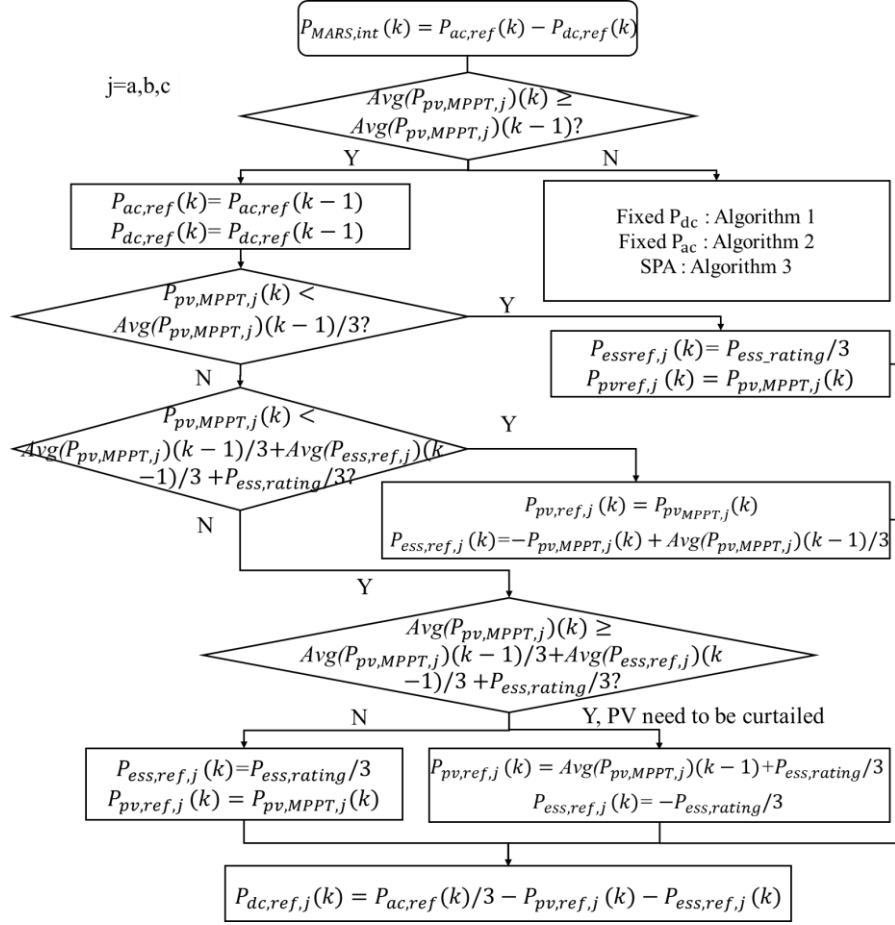


**Figure 5.2 – Flowchart to evaluate the power reference of the dc power, PV and ESS power.**

**Table 5.1 – Algorithm 1& 2& 3: Power mismatch elimination algorithm**

---

Solve the power mismatch problem between phases and obtain proper ac, dc power references for each phase, PV, and ESS power references for each phase.

---

---

```

1. For  $j=a,b,c$ 
2.    $P_{pv,ref,j}(k) = P_{pv,MPPT,j}(k)$ 
3.   Algorithm selection:  $\text{alg}=1$ (fixed  $P_{dc}$ ) or  $\text{alg}=2$ (fixed  $P_{ac}$ ) or  $\text{alg}=3$ (SPA)
4.   If  $\text{alg}=1$ 
5.      $P_{dc,ref}(k) = P_{dc,ref}(k-1)$ 
6.   Else If  $\text{alg}=2$ 
7.      $P_{ac,ref}(k) = P_{ac,ref}(k-1)$ 
8.   end If
9.    $\Delta = \text{Avg}(P_{pv,MPPT,j})(k-1) - \text{Avg}(P_{pv,MPPT,j})(k)$ 
10.  If  $P_{pv,MPPT,j}(k) < \text{Avg}(P_{pv,MPPT,j})(k-1)/3$ 
11.    Set  $P_{ess,ref,j} = P_{ess,rating}/3$ 
12.    Set  $\Delta = \Delta - \left( \frac{P_{ess,ref,j}(k) - P_{ess,ref,j}(k-1)}{3} \right)$ 
13.  Else If  $P_{pv,MPPT,j}(k) < \text{Avg}(P_{pv,MPPT,j})(k-1)/3 + \text{Avg}(P_{ess,ref,j})(k-1)/3 + P_{ess,rating}/3$ 
14.    Set  $P_{ess,ref,j}(k) = -P_{pv,MPPT,j}(k) + \text{Avg}(P_{pv,MPPT,j})(k-1)/3$ 
15.    Set  $\Delta = \Delta - \left( \frac{P_{ess,ref,j}(k) - P_{ess,ref,j}(k-1)}{3} \right)$ 
16.  Else If  $P_{pv,MPPT,j}(k) > \text{Avg}(P_{pv,MPPT,j})(k-1)/3 + \text{Avg}(P_{ess,ref,j})(k-1)/3 + P_{ess,rating}/3$ 
17.    Set  $P_{ess,ref,j} = -P_{ess,rating}/3$ 
18.    Set  $\Delta = \Delta - \left( \frac{P_{ess,ref,j}(k) - P_{ess,ref,j}(k-1)}{3} \right)$ 
19.  end If
20.  If  $\text{alg}=1$ 
21.     $P_{ac,ref}(k) = P_{dc,ref}(k) + \text{Avg}(P_{pv,MPPT,j})(k) + P_{ess,ref,a}(k)/3 + P_{ess,ref,b}(k)/3 + P_{ess,ref,c}(k)/3$ 
22.     $P_{dc,ref,j}(k) = P_{ac,ref}(k)/3 - P_{pv,ref,j}(k) - P_{ess,ref,j}(k)$ 
23.  Else If  $\text{alg}=2$ 
24.     $P_{dc,ref,j}(k) = P_{ac,ref}(k)/3 - P_{pv,ref,j}(k) - P_{ess,ref,j}(k)$ 
25.  Else If  $\text{alg}=3$ 
26.     $P_{ac,ref}(k) = P_{ac,ref}(k-1) + \frac{\Delta * P_{dc,ref}(k-1)}{P_{ac,ref}(k-1) + P_{dc,ref}(k-1)}$ 
27.     $P_{dc,ref,j}(k) = P_{ac,ref}(k)/3 - P_{pv,ref,j}(k) - P_{ess,ref,j}(k)$ 
28.  end If
29. end For

```

---

### 5.1.3 Inter-Arm Power Mismatch Elimination

Whenever inter-arm power mismatch occurs, if inter-phase power mismatch as well, the inter-phase power mismatch will follow the power mismatch elimination algorithm shown in Figure 5.2 first, and the inter-arm power mismatch within an arm will



be solved by fundamental circulating current and ESS power. This section addresses partial fulfillment of arm power balancing. The strategy discussed in the phase mismatch elimination section and the NN-based EBC complete the fulfillment. The operation of the power reference generator can be summarized as follows when  $P_{pv,MPPT,j,p} \neq P_{pv,MPPT,j,n}$ .

If  $P_{pv,MPPT,j,p} \geq P_{pv,MPPT,j,n}$ , The ESS reference power for SMs in each arm will be updated according to an optimization algorithm:

$$\begin{aligned}
& \text{Max } P_{ess,ref,j,p} - P_{ess,ref,j,n} \\
& \text{s.t. } \Delta_{arm} = P_{pv,MPPT,j,p} - P_{pv,MPPT,j,n} \\
& \frac{P_{ess,ref,j}}{3} = P_{ess,ref,j,p} + P_{ess,ref,j,n} \\
& -P_{ess,rating} \leq P_{ess,ref,j,y} \leq P_{ess,rating} \quad y \in \{p, n\} \\
& P_{ess,ref,j,p} - P_{ess,ref,j,n} \leq \Delta_{arm}
\end{aligned}$$

The  $P_{ess,ref,j}$  is obtained from inter-phase power mismatch elimination, which is shown in Figure 5.2.

## 5.2 NN-Based EBC Control

### 5.2.1 Introduction of NN

Since the MARS is a switching model, it generates multivariate data with non-linear relationships. The PI-based EBC, with limited capability of eliminating mismatched power, lacks a mathematical basis to justify the stability and effectiveness of the designed

parameters. The traditional PI-based EBC is designed through induction from simulation results; it is heuristic, without any mathematical basis derived to justify the effectiveness or stability of its design parameters. Thus, it suffers from gain tuning, and the optimum control design is hard to obtain. Tuning the gains of each operating condition is an optimization problem. To ensure all operating conditions are viable for the MARS system and, in the meantime, minimize the injected circulating current, this multi-objective optimization problem is hard to solve manually. In addition, the control variable, which is the gain of the PI controller, provides a limited dimension to satisfy all the objectives. In chapter 4, where PI-based EBC is implemented, each set of gains has been tested under at least 2,000 operating conditions to ensure it is appropriately designed. Even if the optimum gains are found for a given operating condition, it may not be the optimum for others in terms of suppressing circulating current. In other words, when guaranteeing all operating conditions are stable, some of them may have unnecessary high circulating currents. Thus, to address this issue, an NN method is proposed. It can be trained over various operating conditions to understand the system's dynamic and therefore be able to predict optimal circulating current references. Based on the Komogorov's theorem, one hidden layer forward NN is capable of approximating uniformly any continuous multivariate function to any desired degree of accuracy.

The network represents the following relation:

$$\begin{aligned}
 (i_{circ,d,ref}, i_{circ,q,ref}) &= y = F(x) \\
 &= F(P_{ac}, P_{dc}, Q_{ac}, \sum |v_{c\delta}|^2, v_{p,j} - v_{n,j})
 \end{aligned} \tag{5.2}$$

where  $P_{ac}, P_{dc}, Q_{ac}$  are the power dispatch commands and  $v_{p,j} - v_{n,j}$  denotes the arm capacitor voltage mismatch. The control variable  $i_{circ,d,ref}, i_{circ,q,ref}$  are the fundamental circulating current references based on qd reference frame.

### 5.2.2 Data Acquisition and Model Training

The data used for training is obtained through the simulation of the high-fidelity MARS model discussed in chapter 2. With this high-fidelity model, the improvement of the simulation speed is 18,000 times faster than the model built with PSCAD/EMTDC library. The 2s simulation duration for each run only takes about 5 minutes for this 250 SMs per arm system. The input of the NN model is  $P_{ac}, P_{dc}, Q_{ac}$  as well as  $i_{circ,d,ref}, i_{circ,q,ref}$ ; they are swept to obtain the output of the model, which are  $\sum |v_{c\delta}|^2$ , and  $v_{p,j} - v_{n,j}$ . The active reference power  $P_{ac}$  is sampled from a range [-400, 400] MW,  $P_{dc}$  sweeps from [-300, 300] MW,  $Q_{ac}$  sweeps from [-300, 300] MW, and the circulating current references  $i_{circ,d,ref}$  and  $i_{circ,q,ref}$  are sampled from [-1000, 1000] A, and [-1000, 1000] A, respectively. Data samples are generated from the simulations to extract  $\sum |v_{c\delta}|^2, v_{p,j} - v_{n,j}$  for every input combination of  $P_{ac}, P_{dc}, Q_{ac}$  and  $i_{circ,d,ref}, i_{circ,q,ref}$ . The process of sample data acquisition is presented in Figure 5.3. The sample data is filtered to realize the functionality of the EBC. Only data with stable operations and comparatively low circulating current magnitudes are fed into the training process. In total, 30,624 samples are used in the training process.

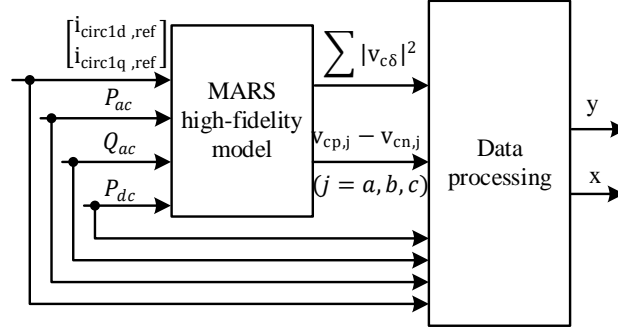


**Figure 5.3 – Data acquisition process.**

### 5.2.3 ANN vs NARX

ANN is the first selected NN algorithm since the numbers of input and output are small, which is also easy to implement. In addition, it is rather simple to perform the hyperparameter tuning. The number of hidden layers, number of neurons in the hidden layer, optimizer, learning rate, as well as the activation function are treated as a bound constrained optimization problem and employ a grid search algorithm for fine-tuning. The optimum model is a 3-layer fully connected network with sigmoid activation function; it has 12 neurons in the hidden layer as depicted in Figure 5.4.

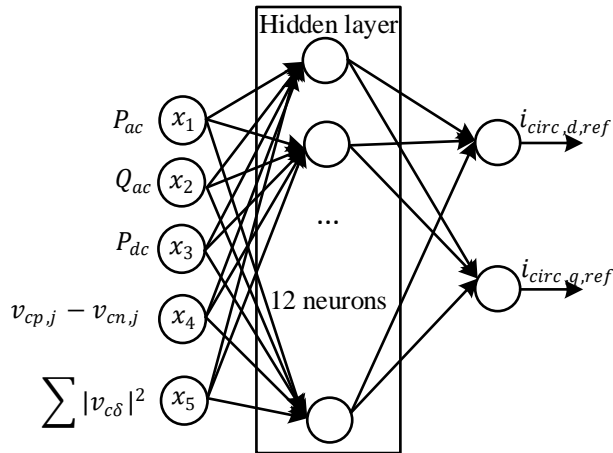


**Figure 5.4 – Diagram of ANN algorithm.**

Considering that, on the one hand, the circulating current is a time series variable and that, on the other hand, the nonlinear autoregressive exogenous (NARX) NN is a good predictor of time series, the NARX NN algorithm is also implemented and compared with the ANN algorithm. Moreover, NARX models can be used to model an extensive variety of nonlinear dynamic systems, with the dynamics at both the input layer and output feedback.

A parallel architecture of NARX is utilized, given by (5.3).

$$\hat{y}(t+1) = F(y(t), y(t-1), \dots, y(t-n_y), x(t+1), x(t), \dots, x(t-n_x)) \quad (5.3)$$

where  $n_y$  is the number of output delays,  $n_x$  is the number of input delays.

Grid search is also employed in the hyperparameter tuning of NARX model; the optimum model is a 3-layer fully connected network with sigmoid activation function; it has 9 neurons in the hidden layer, with no delays in the input and 2-time delays in the output. The model is depicted in Figure 5.5.

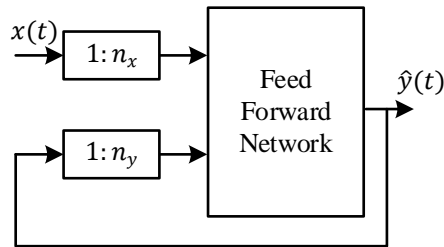


**Figure 5.5 – The architecture of NARX NN.**

Both ANN and NARX models are trained using Levenberg-Marquardt algorithms. The training performance of proposed NN algorithms is showcased using the learning

curve in Figure 5.6 and Figure 5.7, respectively. It is easy to observe that NARX gained lower MSE than the ANN model.

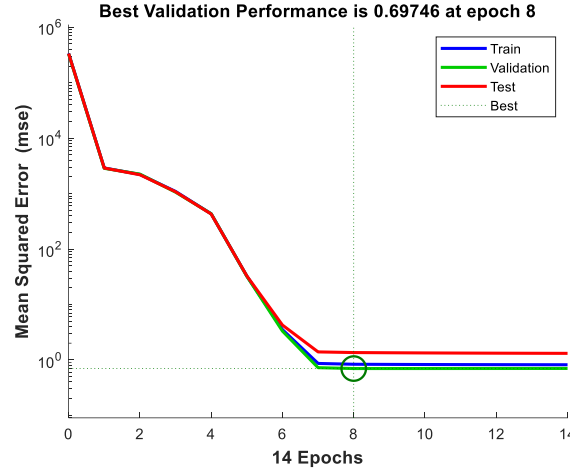


**Figure 5.6 – Learning curve of ANN model.**

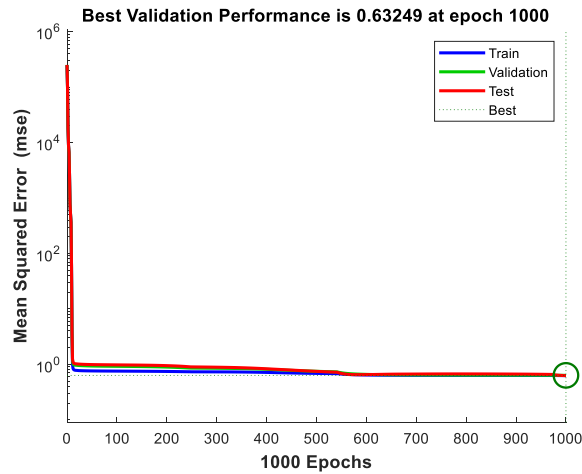


**Figure 5.7 – Learning curve of NARX model.**

#### 5.2.4 Comparison of Existing EBC Methods

The PI-based EBC and the proposed two NN-based EBCs are compared through utilization for cHIL test (Table 5.2), testing MSE (Table 5.3), the number of simulations

required for controller design, and the efficiency of the control algorithms (Table 5.4). The efficiency is defined as the number of operating conditions that have a smaller circulating current magnitude than the PI-based EBC controller out of a total of 2,500 operating conditions. The operating condition is chosen such that the system is unstable without EBC controller. It can be observed that the utilization for all three types of EBC is similar to each other; the NARX-based EBC possesses slightly higher utilization. While in terms of accuracy, NARX is better than ANN-based EBC. The overall number of simulations needed for the controller design is similar. In order to guarantee that the set of gains for the PI-based EBC can balance all operating conditions, each set of gains needs to be tested with 2,500 operating conditions until the system is stable under all 2,500 operating conditions.

From Table 5.4, the advantage of the data-driven methods can be seen. For NARX based-EBC, 1,602 out of 2,500 operating conditions have lower circulating currents compared with the PI-based EBC. Similarly, ANN-based EBC performed better than PI-based EBC in 1,589 operating conditions. Both NN-based EBC methods show better efficiency compared with PI-based EBC, since a lower circulating current can increase the system efficiency and reduce the switching frequency.

**Table 5.2 – Utilization in real-time simulation**

	L1 control with PI-based EBC	L1 control with ANN- based EBC	L1 control with NARX- based EBC
Utilization	12.7%	13.2%	13.5%

**Table 5.3 – Testing accuracy of the confusion matrix**

	PI-based EBC	ANN-based EBC	NARX-based EBC
Accuracy	None	96.05%	97%

**Table 5.4 – Comparison of the EBC controller performance**

PI based EBC (base case)	Number of operating conditions (out of 2,500) that have a smaller circulating current magnitude than the base case
ANN based EBC	1,589
NARX based EBC	1,602

### 5.3 Simulation Results

The effectiveness of the proposed NN-based EBC to handle the phase and arm power mismatch is demonstrated by PSCAD/EMTDC offline simulations. The high fidelity of the Pittsburgh MARS model has 250 SMs in each arm. Among them, 111 are PV SMs, and 37 are ESS SMs. The power rating of the PV plant and ESS is 100MW and 32.8MW, respectively. The MARS circuit is designed based on the ESS and PV plant size. The Pittsburgh MARS rating and component rating are shown in Table 3.1. The predefined range of the SM capacitor voltage is from 0.8pu to 1.2pu. The NN-based EBC control is implemented using MATLAB codes and is utilized by the offline MARS PSCAD model through the MATLAB/PSCAD interface.

#### 5.3.1 Arm Power Mismatch Balanced

All three operation modes have been tested under the event of arm power mismatch and phase power mismatch; since the SPA mode is most likely to happen in the real world, simulation results for the SPA mode are presented first.



This section aims at showcasing the continuity and stable operations of the MARS when an arm power mismatch happens. The system is initially operating at  $P_{ac}=130$  MW  $Q_{ac}=0$ , and  $P_{dc}=70$  MW, with the PV system operating at  $P_{PV,MPPT}=30$  MW, and ESS is charging at 30MW. The PV system is not curtailed and operates at  $P_{PV,MPPT}$ . The NN-based EBC injects a circulating current to make the operating condition viable for the MARS system. At  $t=5$  s, the solar irradiance for the PV generators of phase A's is reduced. Subsequently, considering an extreme case, the MPPT power of Phase A changes from 30MW/3 to 20MW/3, and the MPPT power of Phase B increases from 30MW/3 to 100/3MW. To create the inter-arm power mismatch event, the  $P_{PV,MPPT,a,p}$  of upper arm phase A is reduced to 0, while the  $P_{PV,MPPT,a,n}$  is increase to 40MW/6. Thus, both inter-phase mismatch and inter-arm power mismatch exist in this case. Since  $Avg(P_{PV,MPPT,j})(k-1) \leq Avg(P_{PV,MPPT,j})(k) \leq Avg(P_{PV,MPPT,j})(k-1) + P_{ess,rating}$ , the reference power for  $P_{ac}$  and  $P_{dc}$  remains unchanged. Following the P-V curve of the PV panel, the PV-side capacitor voltages of phase an upper arm increase to 1012.9V, and the lower arm reduced to 964.7V. The PV side capacitor voltage of phase b increase to 839.4V. The PV side capacitor voltage changes of all six arms can be observed in Figure 5.8 (d). In Figure 5.8 (e), the inductor current of phase A upper arm reduces, corresponding to the reduction of  $P_{PV,MPPT}$ . In contrast with the upper arm, the inductor current of phase A lower arm increases. Similar patterns can be observed for the inductor current of phase B PV SMs. The PV-side capacitor voltages and inductor current of phase C remain intact. At  $t=6$ s, the operating condition changes to  $P_{ac}=200$  MW  $Q_{ac}=0$ , and  $P_{dc}=70$  MW, with the PV system operating at  $P_{PV,MPPT}=100$  MW and ESS is charging at 30MW. The power mismatch happens again at  $t=7$ s, the  $P_{PV,MPPT,a}$  and  $P_{PV,MPPT,b}$  reduces to 10/3MW and

70/3MW respectively. To simulate the inter-arm power mismatch, the MPPT power of phase B upper arm is set to be 20/6MW, and the lower arm is set to 120/6MW. Since  $Avg(P_{PV,MPPT,j})(k) \leq Avg(P_{PV,MPPT,j})(k-1)$ , the dispatch command needs to be changed according to the operation mode. The operation mode tested here is the SPA mode and receiving the change of  $P_{PV,MPPT}$  from the L3 controller, the power reference generator of the L1 will respond accordingly; as a result, the ac power output of the MARS to the grid is reduced to 171.75 MW while the dc power of the MARS increases from 70MW to 98.25MW as shown in Figure 5.8 (a). Additionally, the power reference generator will update the dc power reference for three phases and thus inject the dc circulating current to balance the phase power mismatch caused by the arm power mismatch. The arm power mismatch is then handled by the NN-based EBC through injecting a fundamental circulating current. Figure 5.8 (c) shows the change in the circulating currents before and after the power mismatch. Figure 5.8 (e) shows that the currents injected into the grid remain sinusoidal and balanced, but their magnitudes decline since the overall PV power generation is dropped.

The performance of the MARS system under SPA mode with and without NN-based EBC control to an arm power mismatch is illustrated in Figure 5.9 and Figure 5.10. Without NN-based EBC, the phase A normal SM capacitor voltage goes below 1280V, which is the value of the lower limit. According to the definition of stable operating condition, the system is unstable without NN-based EBC. However, with the presence of the proposed EBC, all capacitor voltages lie within the range of capacitor voltage limits.

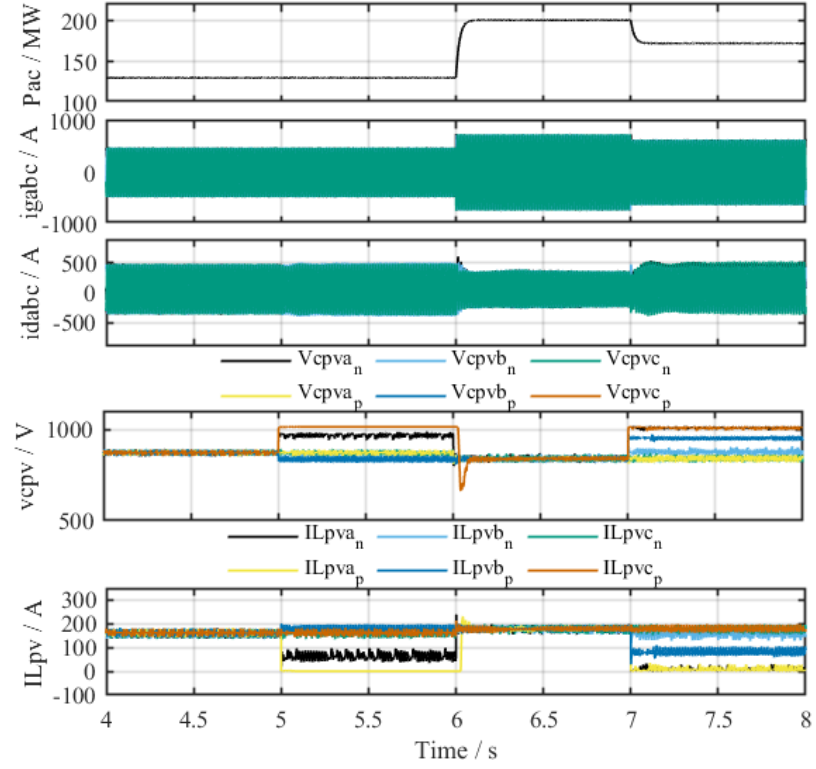


**Figure 5.8 – Response to arm power mismatch under SPA mode: active power measured at grid side, grid side current, circulating current, capacitor voltage, and inductance current at PV side of random PV SMS in the upper arm of three phases.**

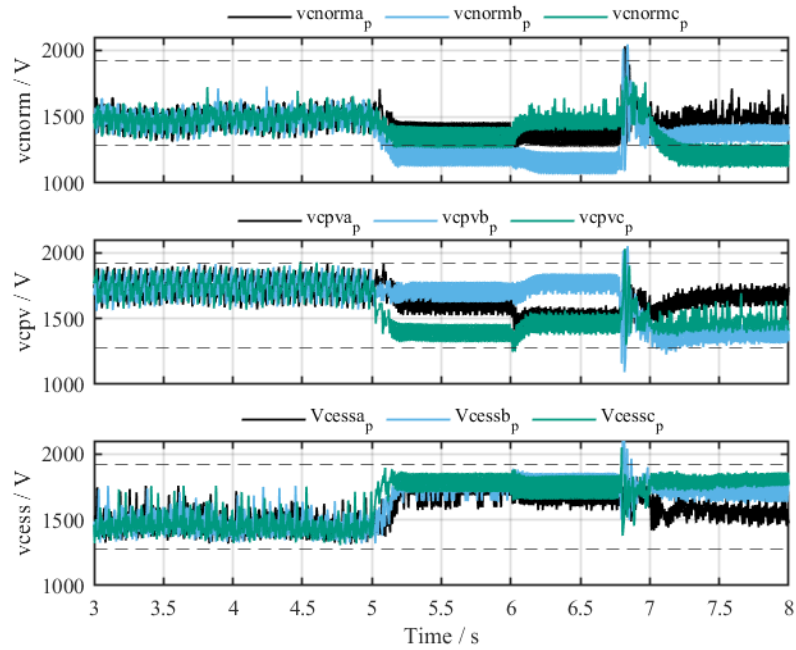


**Figure 5.9 – Response to arm power mismatch under SPA mode: the capacitor voltages of three phases Normal, PV, and ESS SM in upper arm phase A without NN-based EBC.**

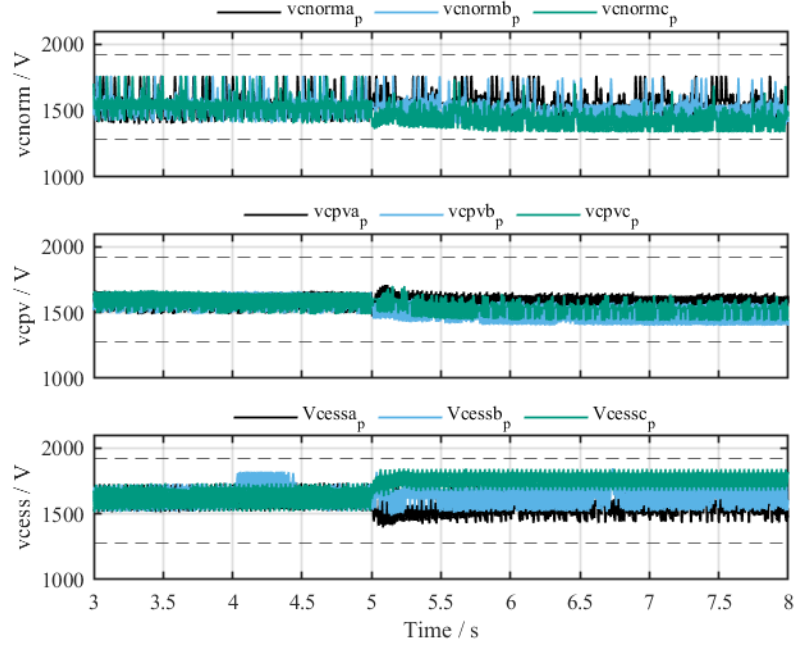


**Figure 5.10 – Response to arm power mismatch under SPA mode: the capacitor voltages of three phases Normal, PV, and ESS SM in upper arm phase A with NN-based EBC.**

The simulation results for fixed  $P_{dc}$  and fixed  $P_{ac}$  are presented in Figure 5.11 to Figure 5.13. Since the simulation results of grid side currents, circulating currents, PV side capacitor voltages, and PV side currents are similar under fixed  $P_{dc}$  mode and fixed  $P_{ac}$  mode, only the results of fixed  $P_{dc}$  mode are illustrated in Figure 5.11. At  $t=5s$ , the arm power mismatch happens, and the mismatch is not cleared until  $t=8s$ . At  $t=7s$ , the EBC is disabled to showcase the necessity of the EBC to balance the SM capacitor voltages. It can be observed from Figure 5.12 and Figure 5.13 that all types of SM capacitor voltages maintain to be balanced with the help of the EBC. The SM capacitor voltages exceed limits (dashed line) after disabling the EBC.

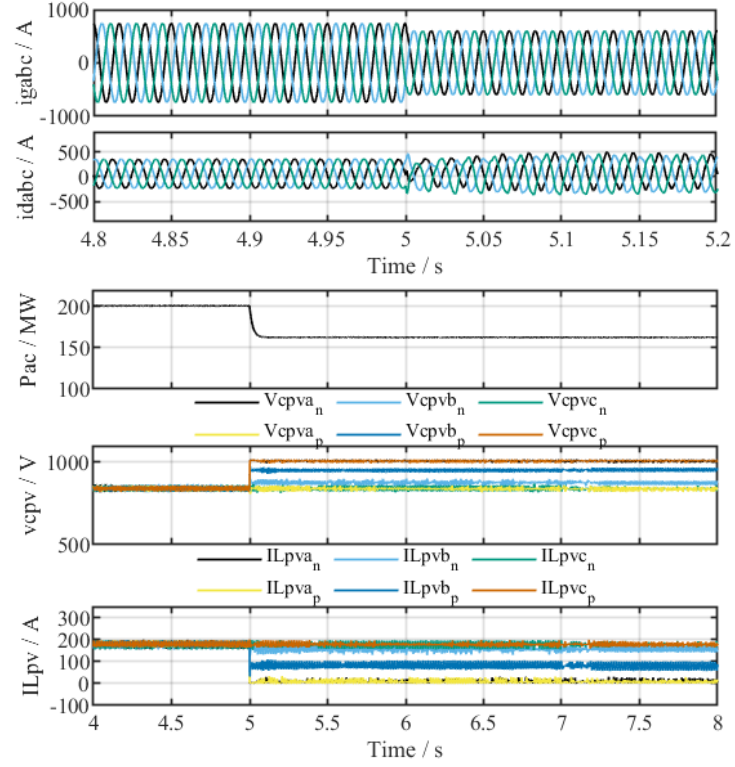


**Figure 5.11 – Response to the arm power mismatch: active power measured at the grid side, grid-side current, circulating current, capacitor voltages, and inductor current at the PV side of random PV SMs in the upper arm of the three phases.**

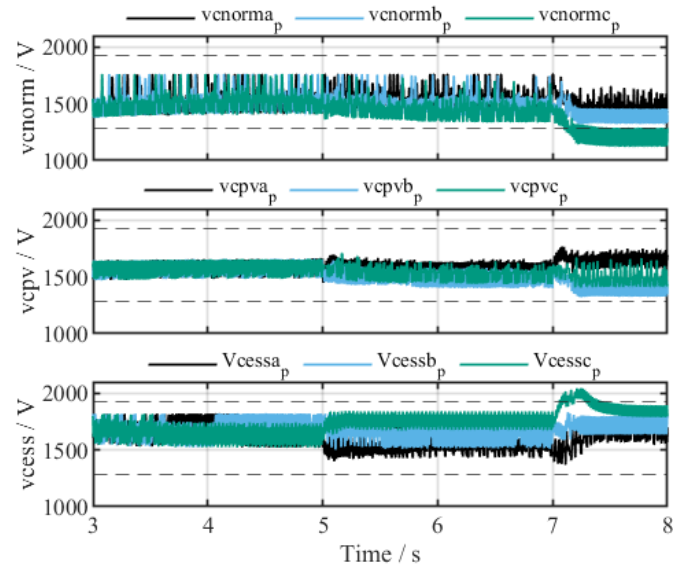


**Figure 5.12 – Response to the arm power mismatch under fixed  $P_{ac}$  mode: the capacitor voltages of the three-phase normal, PV, and ESS SMs in the upper arm phase a without the NN-based EBC.**

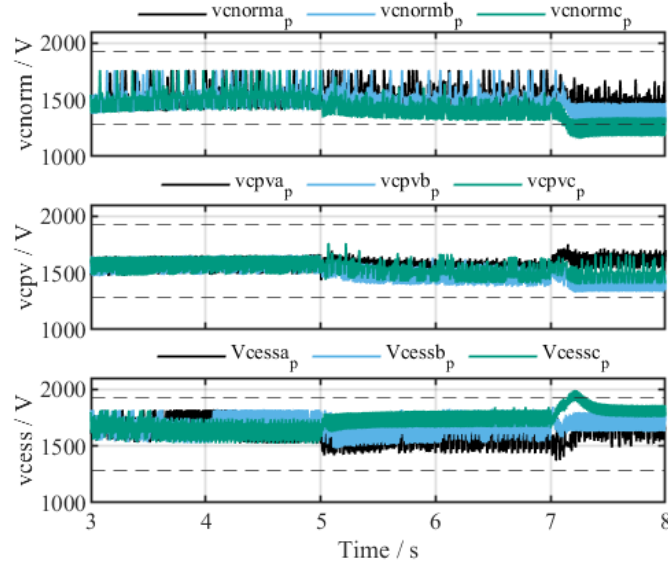


**Figure 5.13 – Response to the arm power mismatch under fixed  $P_{dc}$  mode: the capacitor voltages of the three-phase normal, PV, and ESS SMs in the upper arm phase a without the NN-based EBC.**

### 5.3.2 Phase Power Mismatch Balanced

This test case presents the performance of the MARS in the presence of a power mismatch between the phases. Similar to the arm power mismatch test case, the MARS system initially operates at  $P_{ac}=130$  MW  $Q_{ac}=0$ , and  $P_{dc}=70$  MW. Then, at  $t=5$ s, an extreme case phase power mismatch is created for phase A, by decreasing the irradiation of the PV panel in phase A and increasing that of Phase B, thus reducing its  $P_{PV,MPPT}$  of phase A and increasing the  $P_{PV,MPPT}$  of phase B. The power generated by the PV of phase A is reduced from 30/3 MW to 10/3 MW. At  $t=6$ s, the system starts to operate at  $P_{ac}=200$  MW  $Q_{ac}=0$ , and  $P_{dc}=70$  MW, and one of the extreme case phase power mismatch is created at  $t=7$ s. The MPPT power of phase A and Phase B changes from 100/3MW to

10/3MW and 70/3MW, respectively. Figure 5.14 (d) and (e) show the capacitor voltages of PV SMs and inductor currents of phase A in response to the phase power mismatch. The change of  $P_{PV,MPPT}$  received by the power reference generator in the L1 controller and the output active power of the MARS as well as the d-power references for the three phases are updated, which produce the dc circulating current to balance the power of the three phases. Figure 5.14 (c) shows the waveforms of the circulating currents. As Figure 5.14 (a) shows, due to the solar irradiation drop for the PV generation in phase A, the real power output of the MARS decreases from 200 MW to 170 MW, whereas the grid side currents in Figure 5.14 (c) retain their balanced situation with reduced magnitudes.

Similar to the arm power mismatch test case, the unbalanced SM capacitor voltages are observed without EBC when there is a phase power mismatch, as shown in Figure 5.15. In Figure 5.16, with the presence of EBC, all capacitor voltages are balanced, and the system is stable during the event.

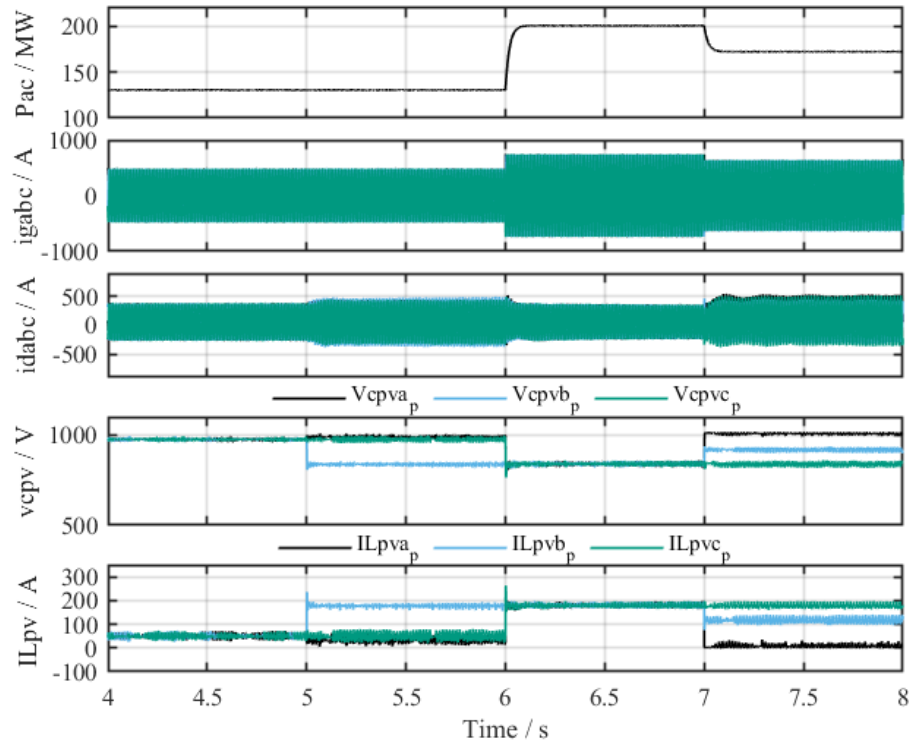


**Figure 5.14 – Response to the phase power mismatch under SPA mode: active power measured at grid side, grid side current, circulating current, capacitor voltage, and inductance current at PV side of random PV SMS in the upper arm of three phases.**

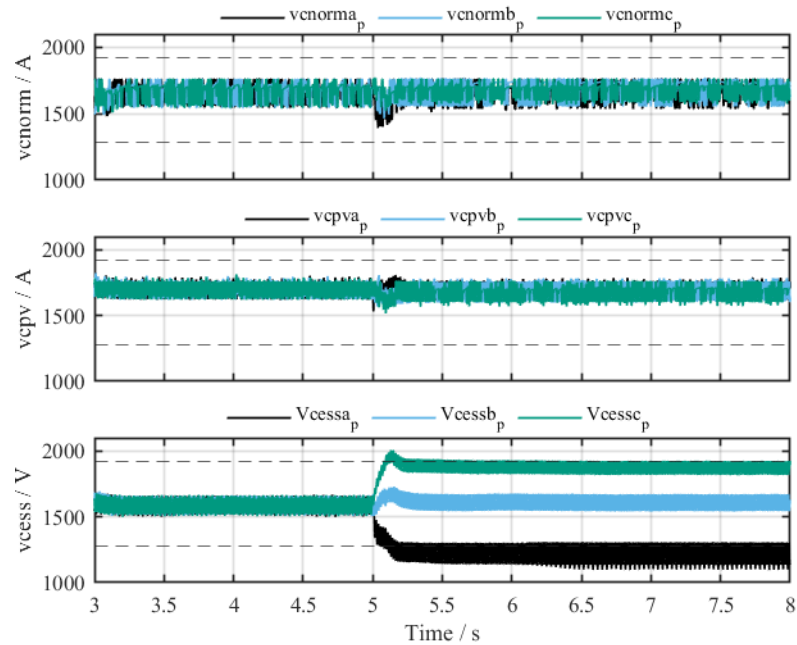




**Figure 5.15 – Response to the phase power mismatch under SPA mode: the capacitor voltages of three phases Normal, PV, and ESS SM in upper arm phase A without NN-based EBC.**

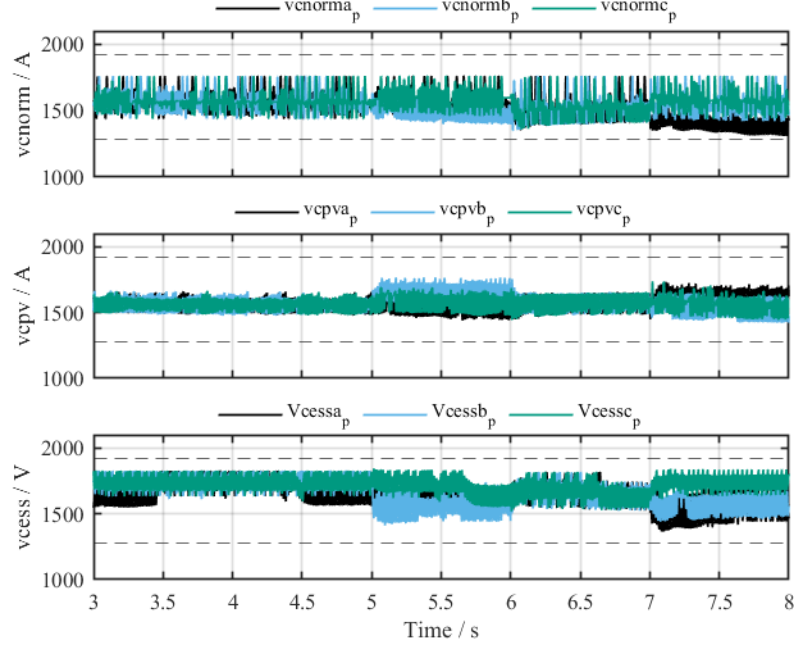


**Figure 5.16 – Response to the phase power mismatch under SPA mode: the capacitor voltages of three phases Normal, PV, and ESS SM in upper arm phase A with NN-based EBC.**

The simulation results for fixed  $P_{dc}$  and fixed  $P_{ac}$  are presented in Figure 5.17- Figure 5.19. Since the simulation results of grid side currents, circulating currents, PV side capacitor voltages, and PV side currents are similar under fixed  $P_{dc}$  mode and fixed  $P_{ac}$  mode, only the results of fixed  $P_{dc}$  mode are illustrated in Figure 5.17. At  $t=5$  s, the phase power mismatch happens, and the mismatch is not cleared until  $t=8$  s. At  $t=7$  s, the EBC is disabled to showcase the necessity of the EBC to balance the SM capacitor voltages. It can be observed from Figure 5.18 and Figure 5.19 that all types of SM capacitor voltages maintain to be balanced with the help of the EBC. The SM capacitor voltages exceed limits (dashed line) after disabling the EBC.

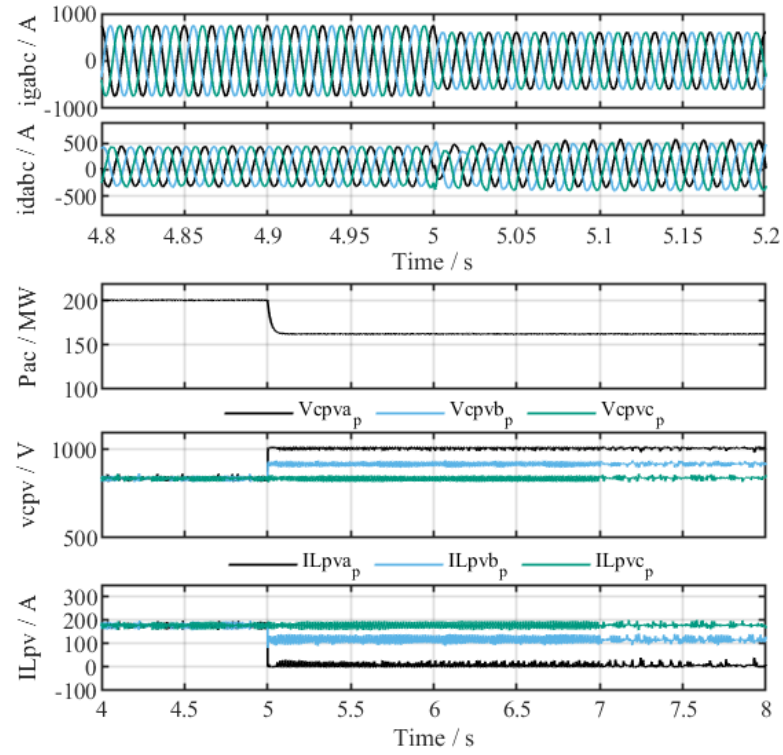


**Figure 5.17 – Response to the phase power mismatch under fixed  $P_{dc}$  mode: active power measured at grid side, grid side current, circulating current, capacitor voltage, and inductance current at PV side of random PV SMS in the upper arm of three phases.**

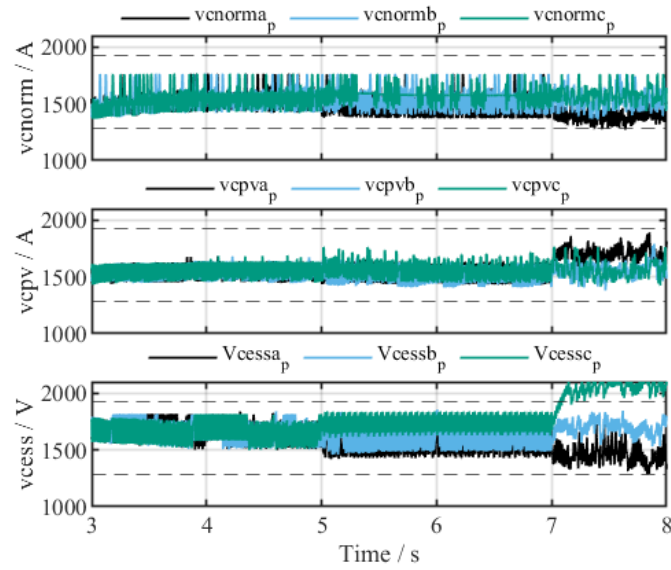


**Figure 5.18 – Response to the phase power mismatch under fixed Pac mode: the capacitor voltages of the three-phase normal, PV, and ESS SMs in the upper arm phase a without the NN-based EBC.**

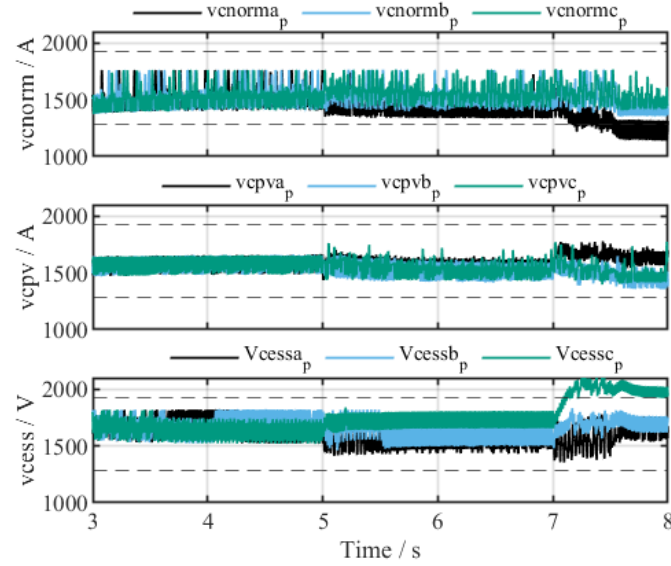


**Figure 5.19 – Response to the phase power mismatch under fixed Pac mode: the capacitor voltages of the three-phase normal, PV, and ESS SMs in the upper arm phase a without the NN-based EBC.**

#### 5.4 cHIL Results

The NN EBC tested in PSCAD offline simulations is also tested in the cHIL experiments. The experiment results will be used to evaluate the robustness of NN-based EBC under stable operating conditions, dynamic operating conditions, and grid events, considering the communication delay and data processing in the cHIL experiment.

The experiment is carried out in a MARS cHIL platform developed using OPAL-RT's real-time simulators. A detailed description of the system is provided in chapter 4.4.

##### 5.4.1 EBC Transition from Disabled to Enabled under Unstable Operating Conditions

In this case study, the MARS real-time simulation model is disabled first and then enabled the EBC under 2 operating conditions. The results for the first operating condition are shown in Figure 5.20, where the dispatch ac-side power command is 100 MW active power, 50MVar reactive power, and 60 MW dc power. The PV and ESS dc-dc converters are enabled and connected to the MARS system with a PV reference voltage of 810 V and ESS reference discharging power of -150 kW. It can also be observed from Figure 5.20 that the SMs' front-end half-bridge capacitor voltages are initially unbalanced, and the ESS SM capacitor voltages lie outside the specified range of 0.8~1.2 time of front-end half-bridge capacitor nominal voltage. The diverging SM capacitor voltages cause instability for the L3 ESS controller. The presented results are per unitized where the base power rating of the system is 400MW, and the base L-L voltage is 220kV. The capacitor voltages turn out to be balanced after the EBC is on, which showcases the successful operation of the NN EBC. The result for the second operating condition is shown in Figure 5.21. A negative power reference is sent to the MARS under operating conditions  $P_{ac}=-100\text{MW}$   $P_{dc}=-170\text{MW}$   $Q_{ac}=0$ , and the capacity voltage disparity also happens first, however, the activation of EBC effectively brings the ESS capacitor voltage back to the limit range. Thus, the EBC is functioning well under these operating conditions and can help maintain the capacitor voltages among different types of SMs.

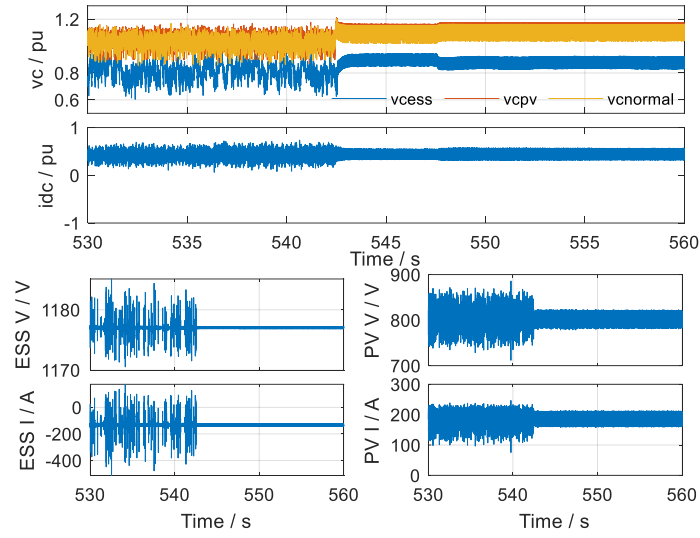


**Figure 5.20 – SM capacitor voltages; ESS, PV capacitor voltages and inductor current under operating condition which capacitor voltage balancing cannot be maintained without the EBC.  $P_{ac}=100\text{MW}$   $P_{dc}=60\text{MW}$   $Q_{ac}=50\text{ MVar}$ .**

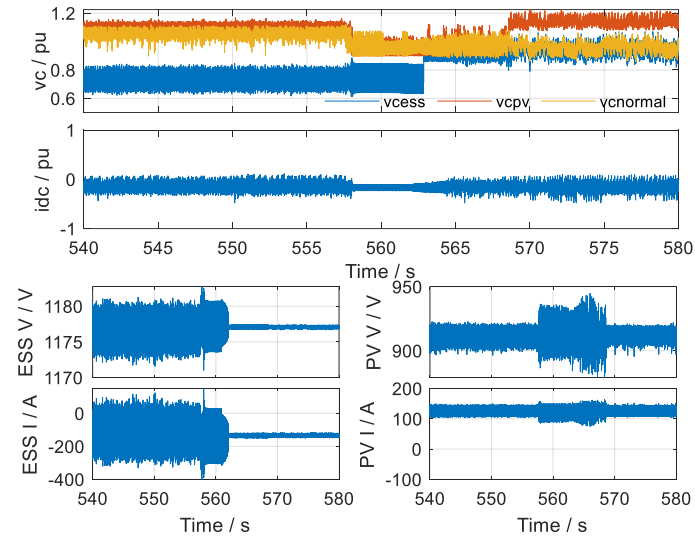


**Figure 5.21 – SM capacitor voltages; ESS, PV capacitor voltages and inductor current under operating condition which capacitor voltage balancing cannot be maintained without the EBC.  $P_{ac}=-100\text{MW}$   $P_{dc}=-170\text{MW}$   $Q_{ac}=0$ .**

#### 5.4.2 Dynamic Operation with NN Based EBC

The steady-state performance of the proposed NN-based EBC under various operating conditions is presented in Figure 5.22. A cyclic test has been performed with the dispatch command steps from  $P_{ac}=300\text{MW}$ ,  $Q_{ac}=0$ ,  $P_{dc}=300\text{MW}$  (stable without EBC) to  $P_{ac}=150\text{MW}$ ,  $Q_{ac}=200\text{MVar}$ ,  $P_{dc}=150\text{MW}$  (unstable without EBC),  $P_{ac}=100\text{MW}$ ,  $Q_{ac}=-50\text{MVar}$ ,  $P_{dc}=60\text{MW}$  (unstable without EBC),  $P_{ac}=-50\text{MW}$ ,  $Q_{ac}=0$ ,  $P_{dc}=-74\text{MW}$  (unstable without EBC) and back to the first operating conditions. The results of the cyclic test of different steady state operating conditions with the NN-based EBC criteria included in the control are presented. The measured grid side active and reactive power are controlled to the references. The grid side current remains stable during the changes of the operating conditions. All three types of SM's front-end half-bridge capacitor voltages are balanced and lie within the required range, which shows the successful operation of NN-based EBC control.

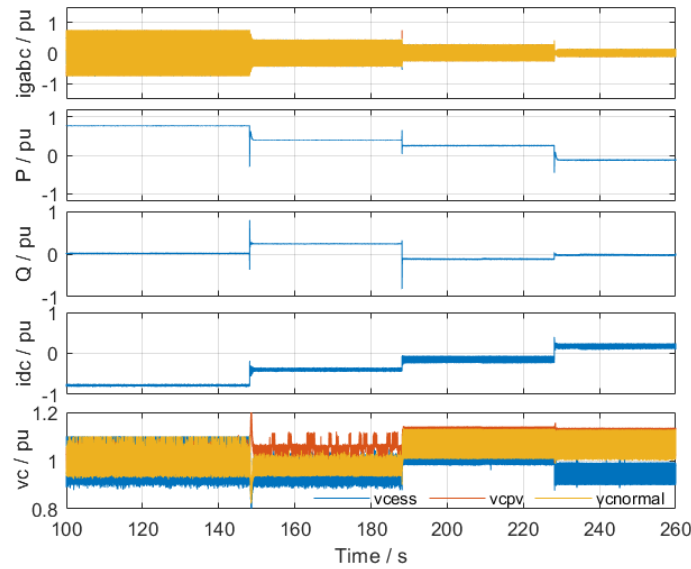


**Figure 5.22 – The MARS grid-side measured three-phase currents, active and reactive powers, dc current, capacitor voltages in representative SMs subsequent to changes in operating condition**

### 5.4.3 Robustness of NN-Based EBC Evaluated under Different Grid Events

Three grid events are identified and tested for multiple operating conditions. Only simulation results of operating condition  $P_{ac} = -50\text{MW}$ ,  $Q_{ac} = 0$ , and  $P_{dc} = -74\text{MW}$  is illustrated in this chapter. Through these tests, the stability and the robustness of NN-based EBC have been evaluated under different operating conditions, and the real-time calculation capability has been verified. The three event includes (a) 804.44 MW loss of generation based on Haynes3 generator in WECC grid, (b) a balanced three-phase fault with a duration of 0.2s, and (c) a line-to-line fault with a duration of 0.2s. The VSG in the L1 controller will provide both frequency and voltage support and enable continuity operating of the MARS under grid events. Testing the loss of generation and the grid fault event is to test the system's robustness under various operating conditions and the EBC under extreme cases like high grid current or unbalanced grid current.

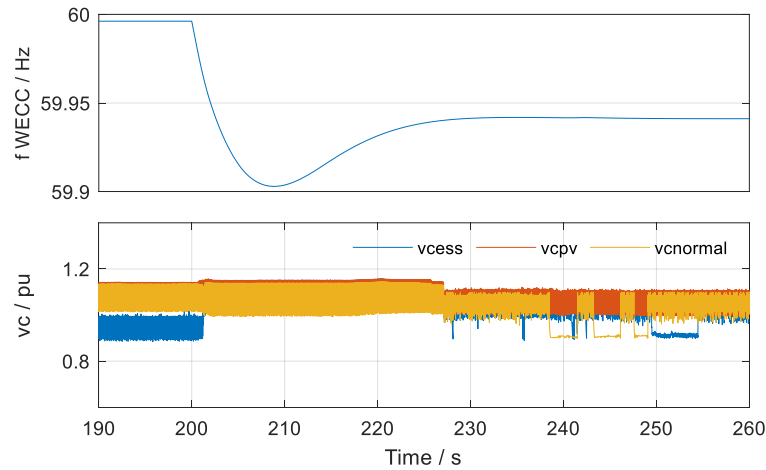


**Figure 5.23 – The MARS L1 cHIL test results: ac-side grid frequency, capacitor voltages of different types of SM during loss of generation event.**

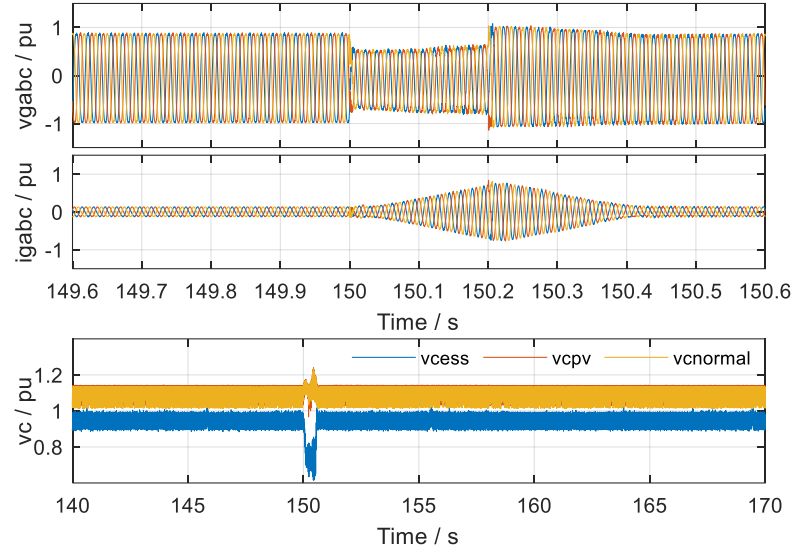


**Figure 5.24 – The MARS L1 cHIL test results: ac-side current, voltage, capacitor voltages of different types of SM during three-phase to ground fault.**

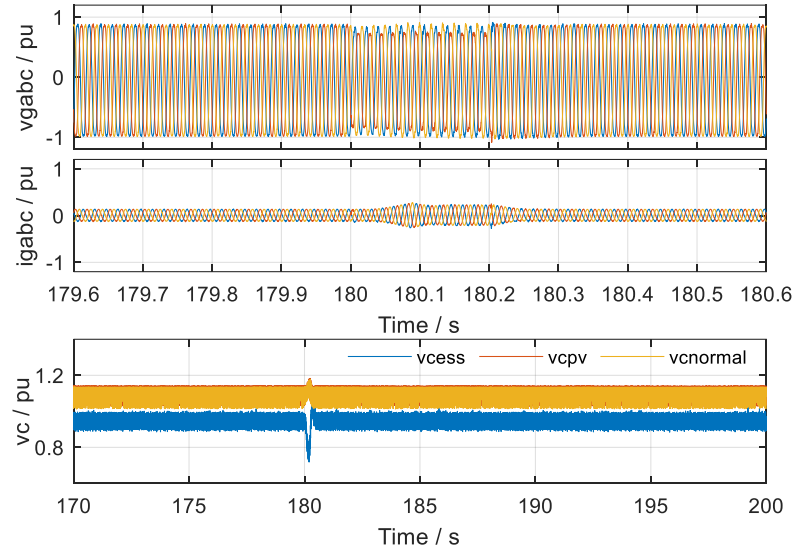


**Figure 5.25 – The MARS L1 cHIL test results: ac-side current, voltage, capacitor voltages of different types of SM during a line-to-line phase fault event.**

It can be observed from Figure 5.23, Figure 5.24, and Figure 5.25 that the capacitor voltages of different types of SMs remain within the upper and lower limits under all three events. The results demonstrate the robustness and stability of the NN-based EBC under



grid events. The ac-side current remains to be sinusoid and balanced without any instability issues. The observed increased current magnitude accounts for the drop in voltage during the fault events and the reactive power support provided by the VSG controller. The stability of the control algorithms under these events is observed. Similar tests were repeated under other operating conditions to examine the stability of the controller. The L1 controller is observed to be stable under these different tested operating conditions.

## **5.5 Summary**

In this chapter, a power mismatch elimination control consisting of a power reference generator and a NN-based EBC is proposed for the MARS system to ensure stable operation under different operating conditions. The NN-based EBC acts as an alternative method to calculate the circulating current references is compared with the traditional PI-based control. It avoids the complicated tuning process and efficiently eliminates the power mismatch and balances the SM capacitor voltages under different conditions. Two different NN-based EBC algorithms based on ANN and NARX are developed to learn the dynamics of the system and map the relationship between the circulating current references and the SM capacitor voltage difference. An analytical analysis has been performed for inter-phase power mismatch elimination and inter-arm power mismatch elimination. The ESS is employed in the power mismatch control strategy to smooth the output power, compensate for the power mismatch, and avoid unnecessary system losses caused by the circulating current.

The inter-arm and inter-phase power mismatches have been tested based on the PSCAD/EMTDC simulations with the PSCAD/MATLAB interface to implement the NN-

based EBC in the MATLAB. Simulation results showcase the successful operation of the proposed NN-based EBC method under PV partial shading. cHIL experimental results show that the proposed method can achieve SM capacitor voltage balancing and improve the system efficiency compared to the traditional PI control. In addition, the performance of the NN-based EBC control under different grid events and different operating conditions using cHIL tests is verified, which further demonstrates the stability and feasibility of the proposed NN-based EBC.

## **CHAPTER 6. MODEL PREDICTIVE CONTROL OF THE MARS**

The two proposed advanced control methods in the previous chapters are data-driven methods that require a large dataset to train the ML models. In this chapter, an MPC strategy that does not require any dataset is proposed to control the MARS's grid-side current, circulating current, and balancing the SM capacitor voltages. The MPC is a model-based control. The mathematical process models in model-based control are usually difficult and expensive to obtain due to the complexity of the system and poor understanding of the underlying physics. However, the implementation of the model-based control can significantly improve the control quality compared to the simple multi-loop SISO controllers that are still widely used in the industry. Note that the control challenges of the MARS are fundamentally different from a conventional MMC since it has multiple types of external sources that connect to the SMs. In this way, the assumption that all SM capacitor voltages are balanced is invalid. In this chapter, these challenges are addressed, and an MPC strategy is proposed. The proposed strategy significantly improves the system's dynamic performance and explicitly controls the capacitor voltages within the upper and lower limit.

### **6.1 Nonlinear Model of the MARS**

As shown in Figure 6.1, the system is represented by an average model, in which each set of identical SMs is modeled by an equivalent capacitor. This type of modeling is initially proposed by [35] for an MMC whose SMs are connected to a renewable energy source. However, it was further exploited by [84] for analyzing an MMC-based ESS system. In this chapter, each arm is partitioned into three parts, where the subscripts of the

variables  $N_{norm}$ ,  $N_{pv}$ , and  $N_{ess}$  correspond to the normal SMs, SMs with PV input power, and SMs with ESS input/output power, respectively. Taking the phase A upper arm, for example, the different types of SMs in series can be equivalent to three voltage sources  $m_{npa}v_{npa}$ ,  $m_{pvpa}v_{pvpa}$ , and  $m_{esspa}v_{esspa}$  controlled by the external circuit composed of the controlled current source  $i_{pa}$ , external current source  $i_{pv}$ ,  $i_{ess}$  and the arm equivalent capacitor C.  $v_{npa}$ ,  $v_{pvpa}$ ,  $v_{esspa}$  are the sum of the SM capacitor voltages of normal SM, PV SM, and ESS SM.

The relationship among these variables can be expressed as follows:

$$v_{p,a} = m_{npa}v_{npa} + m_{pvpa}v_{pvpa} + m_{esspa}v_{esspa} \quad (6.1)$$

$$V_{dc} = v_{p,a} + L_o \frac{d i_{p,a}}{dt} + R_o i_{p,a} + v_{n,a} - L_o \frac{d i_{n,a}}{dt} - R_o i_{n,a} \quad (6.2)$$

$$\frac{V_{dc}}{2} = v_{p,a} + L_o \frac{d i_{p,a}}{dt} + R_o i_{p,a} + L_s \frac{d i_{ga}}{dt} + R_s i_{ga} + v_{ga} \quad (6.3)$$

$$\frac{V_{dc}}{2} = v_{n,a} - L_o \frac{d i_{n,a}}{dt} - R_o i_{n,a} - L_s \frac{d i_{ga}}{dt} - R_s i_{ga} - v_{ga} \quad (6.4)$$

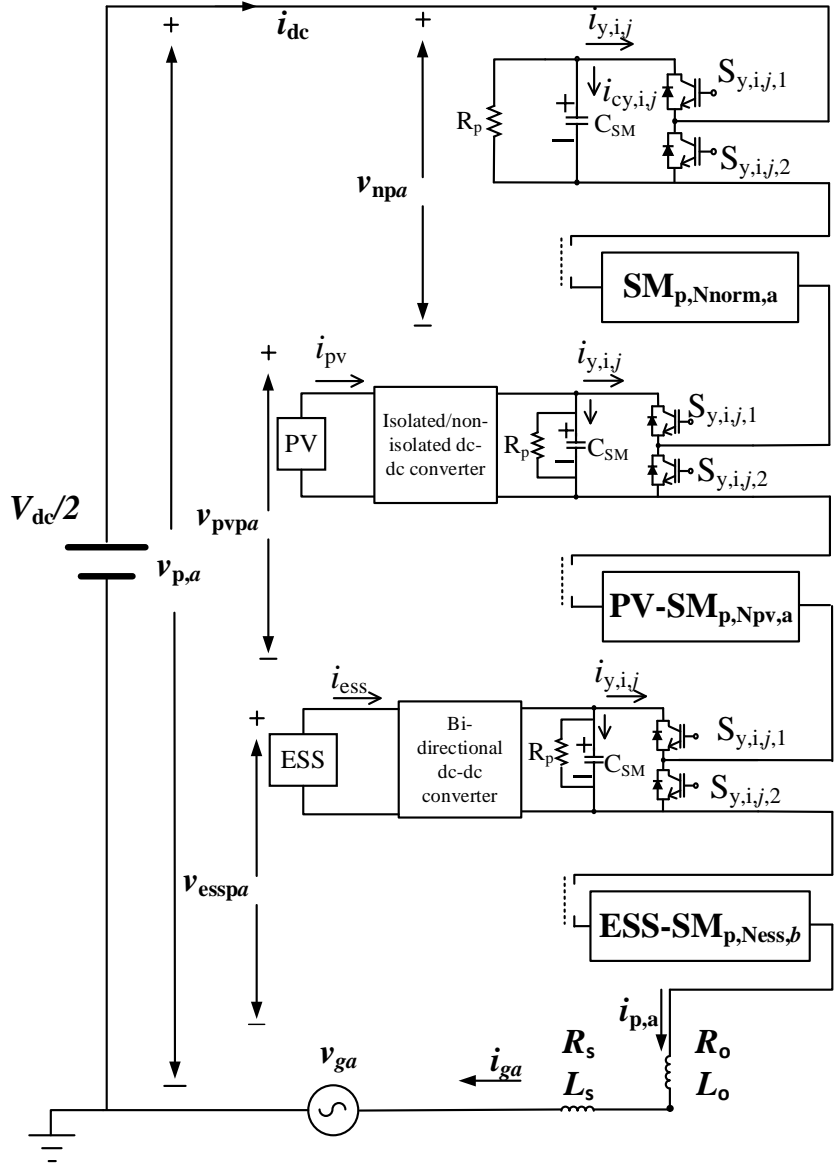


**Figure 6.1 – Schematic diagram of one arm of the MARS**

The corresponding variables in the lower arm can be obtained by replacing the subscript p with n. The subscript a can also be replaced by phases b and c.  $m_{npa}$ ,  $m_{pvpa}$ , and  $m_{esspa}$  are defined here as the modulation ratio of normal SMs, PV SMs, and ESS SMs, respectively. In Figure 6.1, we see  $i_{p,a} = \frac{i_{ga}}{2} + i_{da}$  and  $i_{n,a} = -\frac{i_{ga}}{2} + i_{da}$ , where  $i_{La}$  represent the phase a grid side current and  $i_{da}$  represent the phase a circulating current.

The differential equation of  $i_{da}$  can be expressed as

$$L_o \frac{d i_{da}}{dt} = \frac{V_{dc}}{2} - v_{p,a} - v_{n,a} - R_o i_{da} \quad (6.5)$$

Similarly, the differential equation of  $i_{ga}$  can be described as

$$(L_o + 2L_s) \frac{d i_{ga}}{dt} = v_{n,a} - v_{p,a} - (R_o + 2R_s) i_{ga} \quad (6.6)$$

The dynamics of sum of capacitor voltages of normal SM s PV SMs and ESS SMs in phase A upper arm are expressed as:

$$C \frac{d v_{npa}}{dt} = \frac{m_{npa}}{c} \left( \frac{i_{ga}}{2} + i_{da} \right) \quad (6.7(a))$$

$$C \frac{d v_{pvpa}}{dt} = \frac{m_{pvpa}}{c} \left( \frac{i_{ga}}{2} + i_{da} \right) + \frac{1}{C} * \frac{P_{pv}}{6} * \frac{N_{pv}}{v_{pvpa}} \quad (6.2(b))$$

$$C \frac{d v_{esspa}}{dt} = \frac{m_{esspa}}{c} \left( \frac{i_{ga}}{2} + i_{da} \right) + \frac{1}{C} * \frac{P_{ess}}{6} * \frac{N_{ess}}{v_{esspa}} \quad (6.2(c))$$

Assuming the dynamics of the current components are identical for each phase, and the capacitor voltages for each type of SMs are balanced, each phase leg of the system is modeled separately using a per-phase modeling philosophy. Modeling phase j (j=a, b, c) of the MMC, the load current ( $i_{gj}$ ), circulating current ( $i_{dj}$ ), and the sum of PV, ESS, normal SM are taken as the state variable. Hence, the state vector  $x(t)$  is defined as:

$$x(t) := [i_{gj} \ i_{dj} \ v_{npj} \ v_{pvpj} \ v_{esspj} \ v_{nnj} \ v_{pvnj} \ v_{essnj}]^T \quad (6.8)$$

The control input vector  $u(t)$  is composed of the modulation index for different types of SMs. Hence, the control inputs vector is defined as

$$u(t) := [m_{npj} \ m_{pvpj} \ m_{esspj} \ m_{nnj} \ m_{pvnj} \ m_{essnj}]^T \quad (6.9)$$

The 24th-order state space representation of the MMC is obtained as:

$$\dot{x}(t) = A(u(t)) \cdot x(t) + D\omega(t) \quad (6.10)$$

where

$$A := \begin{bmatrix} \frac{R_o + 2R_s}{L_o + 2L_s} & 0 & -\frac{m_{npj}}{L_o + 2L_s} & -\frac{m_{pvpj}}{L_o + 2L_s} & -\frac{m_{esspj}}{L_o + 2L_s} & \frac{m_{nnj}}{L_o + 2L_s} & \frac{m_{pvnj}}{L_o + 2L_s} & \frac{m_{essnj}}{L_o + 2L_s} \\ 0 & -\frac{R_o}{L_o} & -\frac{m_{npj}}{2L_o} & -\frac{m_{pvpj}}{2L_o} & -\frac{m_{esspj}}{2L_o} & -\frac{m_{nnj}}{2L_o} & -\frac{m_{pvnj}}{2L_o} & -\frac{m_{essnj}}{2L_o} \\ \frac{1}{2C}m_{npj} & \frac{1}{C}m_{npj} & 0 & 0 & 0 & 0 & 0 & 0 \\ \frac{1}{2C}m_{pvpj} & \frac{1}{C}m_{npj} & 0 & 0 & 0 & 0 & 0 & 0 \\ \frac{1}{2C}m_{esspj} & \frac{1}{C}m_{npj} & 0 & 0 & 0 & 0 & 0 & 0 \\ -\frac{1}{2C}m_{nnj} & \frac{1}{C}m_{nnj} & 0 & 0 & 0 & 0 & 0 & 0 \\ -\frac{1}{2C}m_{pvnj} & \frac{1}{C}m_{pvnj} & 0 & 0 & 0 & 0 & 0 & 0 \\ -\frac{1}{2C}m_{essnj} & \frac{1}{C}m_{essnj} & 0 & 0 & 0 & 0 & 0 & 0 \end{bmatrix} \quad (6.11)$$

$$\omega(t) := [v_{DC}(t) \ i_{pv}(t) \ i_{ess}(t) \ i_{pv}(t) \ i_{ess}(t) \ v_s(t)]^T \quad (6.12)$$

and

$$D := \begin{bmatrix} \frac{1}{2L_o} & 0 & 0 & 0 & 0 & -\frac{2}{L_o + 2L_s} \\ 0 & 0 & 0 & 0 & 0 & 0 \\ 0 & 0 & 0 & 0 & 0 & 0 \\ 0 & \frac{N_{pv}}{C} & 0 & 0 & 0 & 0 \\ 0 & 0 & \frac{N_{ess}}{C} & 0 & 0 & 0 \\ 0 & 0 & 0 & 0 & 0 & 0 \\ 0 & 0 & 0 & \frac{N_{pv}}{C} & 0 & 0 \\ 0 & 0 & 0 & 0 & \frac{N_{ess}}{C} & 0 \end{bmatrix} \quad (6.13)$$

It can be observed that (6.10) is a bilinear model due to the multiplication of the inputs and the states variable. The nonlinearity here introduces heavy computation burden and complexity to the MPC. In this chapter, the non-linear state space model is linearized using first-order Taylor series expansion.

At time  $t = t_0$ , first-order Tylor series expansion around the current operating point can be performed to linearize the model. To further linearized the model, the injecting PV and ESS current instead of the ESS and PV power are controlled in the dc-dc converter. Thus, the linear state space model is

$$\dot{x}(t) = A_l(t_0) \cdot x(t) + B_l(t_0) \cdot u(t) + D\omega(t) \quad (6.14)$$

with the state matrix  $A_l$  defined as



$$A_l(t_0) := \begin{bmatrix} -\frac{R_o + 2R_s}{L_o + 2L_s} & 0 & -\frac{m_{npj}(t_0)}{L_o + 2L_s} & -\frac{m_{pvpj}(t_0)}{L_o + 2L_s} & -\frac{m_{esspj}(t_0)}{L_o + 2L_s} & \frac{m_{nnj}(t_0)}{L_o + 2L_s} & \frac{m_{pvnj}(t_0)}{L_o + 2L_s} & \frac{m_{essnj}(t_0)}{L_o + 2L_s} \\ 0 & -\frac{R_o}{L_o} & -\frac{m_{npj}(t_0)}{2L_o} & -\frac{m_{pvpj}(t_0)}{2L_o} & -\frac{m_{esspj}(t_0)}{2L_o} & -\frac{m_{nnj}(t_0)}{2L_o} & -\frac{m_{pvnj}(t_0)}{2L_o} & -\frac{m_{essnj}(t_0)}{2L_o} \\ \frac{1}{2C}m_{npj}(t_0) & \frac{1}{C}m_{npj}(t_0) & 0 & 0 & 0 & 0 & 0 & 0 \\ \frac{1}{2C}m_{pvpj}(t_0) & \frac{1}{C}m_{pvpj}(t_0) & 0 & 0 & 0 & 0 & 0 & 0 \\ \frac{1}{2C}m_{esspj}(t_0) & \frac{1}{C}m_{esspj}(t_0) & 0 & 0 & 0 & 0 & 0 & 0 \\ -\frac{1}{2C}m_{nnj}(t_0) & -\frac{1}{C}m_{nnj}(t_0) & 0 & 0 & 0 & 0 & 0 & 0 \\ -\frac{1}{2C}m_{pvnj}(t_0) & -\frac{1}{C}m_{pvnj}(t_0) & 0 & 0 & 0 & 0 & 0 & 0 \\ -\frac{1}{2C}m_{essnj}(t_0) & -\frac{1}{C}m_{essnj}(t_0) & 0 & 0 & 0 & 0 & 0 & 0 \end{bmatrix} \quad (6.15)$$

The control input variable is reformulated as

$$\Delta u(t) := [\Delta m_{npj} \ \Delta m_{pvpj} \ \Delta m_{esspj} \ \Delta m_{nnj} \ \Delta m_{pvnj} \ \Delta m_{essnj}]^T \quad (6.16)$$

where  $\Delta m = m(t) - m(t_0)$

Thus, the input matrix becomes

$$B_l(t_0) := \begin{bmatrix} -\frac{v_{npj}(t_0)}{L_o + 2L_s} & -\frac{v_{pvpj}(t_0)}{L_o + 2L_s} & -\frac{v_{esspj}(t_0)}{L_o + 2L_s} & \frac{v_{nnj}(t_0)}{L_o + 2L_s} & \frac{v_{pvnj}(t_0)}{L_o + 2L_s} & \frac{v_{essnj}(t_0)}{L_o + 2L_s} \\ -\frac{v_{npj}(t_0)}{L_o + 2L_s} & -\frac{v_{pvpj}(t_0)}{L_o + 2L_s} & -\frac{v_{esspj}(t_0)}{L_o + 2L_s} & -\frac{v_{nnj}(t_0)}{L_o + 2L_s} & -\frac{v_{pvnj}(t_0)}{L_o + 2L_s} & -\frac{v_{essnj}(t_0)}{L_o + 2L_s} \\ \frac{1}{2C}i_{gj}(t_0) + \frac{1}{C}i_{dj}(t_0) & 0 & 0 & 0 & 0 & 0 \\ 0 & \frac{1}{2C}i_{gj}(t_0) + \frac{1}{C}i_{dj}(t_0) & 0 & 0 & 0 & 0 \\ 0 & 0 & \frac{1}{2C}i_{gj}(t_0) + \frac{1}{C}i_{dj}(t_0) & 0 & 0 & 0 \\ 0 & 0 & 0 & -\frac{1}{2C}i_{gj}(t_0) + \frac{1}{C}i_{dj}(t_0) & 0 & 0 \\ 0 & 0 & 0 & 0 & -\frac{1}{2C}i_{gj}(t_0) + \frac{1}{C}i_{dj}(t_0) & 0 \\ 0 & 0 & 0 & 0 & 0 & -\frac{1}{2C}i_{gj}(t_0) + \frac{1}{C}i_{dj}(t_0) \end{bmatrix} \quad (6.17)$$

Using the forward euler method, the model is discretized over the sampling time  $T_s$ ,

yields the corresponding discrete-time models

$$x(k+1) = A_{dl}(t_0) \cdot x(k) + B_{dl}(t_0) \cdot u(k) + D_{dl}\omega(k), \quad k \in \mathbb{Z}_+ \quad (6.18)$$

## 6.2 Mathematical Modelling

### 6.2.1 Predictive Model of the MMC

In model predictive control, the predictive plant output will be calculated with the future control signal to minimize the designed cost function. The prediction is carried out within the optimization window, which includes the prediction horizon  $N_p$  and control horizon  $N_c$ . Define vectors  $X$ ,  $\Delta U$ , and  $W$  as:

$$X = [x(k+1|k) \ x(k+2|k) \ x(k+3|k) \ \dots \ x(k+N_p|k)]^T \quad (6.19)$$

$$\Delta U = [\Delta u(k) \ \Delta u(k+1) \ \Delta u(k+2) \ \dots \ \Delta u(k+N_c-1)]^T \quad (6.20)$$

$$W = [\omega(k) \ \omega(k+1) \ \omega(k+2) \ \dots \ \omega(k+N_p-1)]^T \quad (6.21)$$

where  $x(k+m|k)$  is the predicted future state variables at  $k+m$  with given current state information  $x(k)$ . The relationship between the future control movement and the predicted future state variables has been derived and can be expressed as:

$$X = Fx(k) + \phi U + \gamma W \quad (6.22)$$

where

$$F = \begin{bmatrix} A \\ A^2 \\ \vdots \\ A^{N_p} \end{bmatrix}_{24N_p \times 24}$$

$$\phi = \begin{bmatrix} B & \dots & 0 \\ \vdots & \ddots & \vdots \\ A^{N_p-1}B & \dots & A^{N_p-N_c}B \end{bmatrix}_{24N_p \times 18N_c}$$

$$\gamma = \begin{bmatrix} I & 0 & \cdots & 0 \\ \vdots & \vdots & \ddots & \vdots \\ A^{N_p-1}I & A^{N_p-2}I & \cdots & I \end{bmatrix}_{24N_p \times 18N_c}$$

### 6.2.2 Cost Function Minimization

To guarantee a proper and safe functioning of the MARS, the cost function addresses four control objectives in terms of active power tracing, reactive power tracking, circulating current reduction, and SM capacitor voltage balancing. Thus, the first part of the objective function penalizes the tracking error of the state variables over the prediction horizon through manipulating the control variable. It yields

$$J_1 = (R - X)^T Q (R - X) \quad (6.23)$$

where R denotes the time varying reference matrix.

$$R = [r(k+1|k) \ r(k+2|k) \ r(k+3|k) \ \dots \ r(k+N_p|k)]^T$$

$$r(k+m|k) = [i_{gj}^*(k+m) \ i_{dj}^*(k+m) \ v_{cref}N_n \ v_{cref}N_{pv} \ v_{cref}N_{ess} \ v_{cref}N_n \ v_{cref}N_{pv} \ v_{cref}N_{ess}],$$

$$m = 1, \dots, N_p$$

$i_{dj}^*(k+m)$  is set to be  $\frac{1}{3}I_{dc}$  to minimize the harmonics of the circulating current.

The second part of the cost function is to penalize the change of input variables with the matrix  $Q_U$ .

$$J_2 = \Delta U^T Q_U \Delta U \quad (6.24)$$

$$J = J_1 + J_2 = (R - X)^T Q (R - X) + \Delta U^T Q_U \Delta U \quad (6.25)$$

Substitute (6.22) into (6.25) and neglecting constant terms yields:

$$J = (\phi \Delta U)^T Q \phi \Delta U + (\Delta U)^T Q_U \Delta U + (-2R^T + 2(Fx_k)^T + 2(\gamma W)^T) Q \phi \Delta U \quad (6.26)$$

Constraints for both input control variables and state variables are taken into account. The modulation indexes have hard constraints due to the physical limitations of the MARS system (6.27). Similarly, the current constraints for both grid side current and circulating current are proposed (6.28) and (6.29).

$$0 \leq m_{xyj}(k+t) \leq \frac{N_y}{N}, \quad \forall x = \{n, pv, ess\}, \forall y = \{n, p\}, \forall j = \{a, b, c\} \quad \forall t = \{0, \dots, N_c - 1\}, \quad (6.27)$$

$$i_{gmin} \leq i_{gj}(k|k+m) \leq i_{gmax}, \quad \forall j = \{a, b, c\} \quad \forall m = \{1, \dots, N_p\} \quad (6.28)$$

$$i_{dmin} \leq i_{dj}(k|k+m) \leq i_{dmax}, \quad \forall j = \{a, b, c\} \quad \forall m = \{1, \dots, N_p\} \quad (6.29)$$

Since  $U = [u(k) \ u(k+1) \ u(k+2) \ \dots \ u(k+N_c-1)]^T$  satisfy

$$\begin{aligned} u(k+N_c-1) &= \Delta u(k+N_c-1) + \Delta u(k+N_c-2) + \dots + \Delta u(k) \\ &+ u(k-1) \end{aligned} \quad (6.30)$$

Thus,  $U = M_1 \Delta U + M_2 u(k-1)$

where

$$M_1 = \begin{bmatrix} I_{18 \times 18} & 0 & \cdots & 0 \\ I_{18 \times 18} & I_{18 \times 18} & 0 & 0 \\ \vdots & \vdots & \ddots & \vdots \\ I_{18 \times 18} & I_{18 \times 18} & \cdots & I_{18 \times 18} \end{bmatrix}_{18N_c \times 18N_c}$$

$$M_2 = \begin{bmatrix} I_{18 \times 18} & 0 & \cdots & 0 \\ 0 & I_{18 \times 18} & 0 & 0 \\ \vdots & \vdots & \ddots & \vdots \\ 0 & 0 & \cdots & I_{18 \times 18} \end{bmatrix}_{18N_c \times 18N_c}$$

Rewriting (6.27) into matrix form yields:

$$\begin{bmatrix} -M_1 \\ M_1 \end{bmatrix} \Delta U \leq \begin{bmatrix} (-U_{min} + u(k-1))M_2 \\ (U_{max} - u(k-1))M_2 \end{bmatrix} \quad (6.31)$$

The capacitor voltage of each type of SMs per arm is limited as follows:

$$0.75 \frac{N_x}{N} V_{dc} \leq v_{xyj}(k+m|k) \leq 1.25 \frac{N_x}{N} V_{dc}, \quad (6.32)$$

$$\forall x = \{n, pv, ess\} \quad \forall y = \{n, p\}, \forall j = \{a, b, c\} \quad \forall m$$

$$= \{1, \dots, N_p\}$$

The constraints can be rewritten as:

$$X_{min} \leq X \leq X_{max} \quad (6.33)$$

Substitute (6.22) into (6.33) leads:

$$X_{min} \leq Fx(k) + \phi \Delta U + \gamma W \leq X_{max} \quad (6.34)$$

$$\begin{bmatrix} -M_1 \\ M_1 \\ -\phi \\ \phi \end{bmatrix} U \leq \begin{bmatrix} (-U_{min} + u(k-1))M_2 \\ (U_{max} - u(k-1))M_2 \\ Fx(k) + \gamma W - X_{min} \\ X_{max} - Fx(k) + \gamma W \end{bmatrix} \quad (6.35)$$

Thus, the quadratic optimization problem (6.26) with the linear constraints (6.35) can be solved using quadratic optimization solver.

### 6.2.3 CVBC

Different types of SMs in the MARS system are operated with conventional NLC methods respectively and followed with individual CVBC. Applying the NLC strategy, each sampling time, the number of the switched-on Normal, PV, or ESS SMs in each arm (or the so-called insertion index) is easily determined by rounding its reference voltage as follows:

$$N_{xyj} = \text{round}\left(\frac{v_{xyj}}{V_{dc}/N}\right), \quad (6.36)$$

$$\forall x = \{n, pv, ess\} \quad \forall y = \{n, p\}, \forall j = \{a, b, c\}$$

where  $v_{xyj}$  is the sum of x types of SMs in arm y of phase j.

The proposed MPC with the modified capacitor voltage balancing algorithms is illustrated in Figure 6.2.

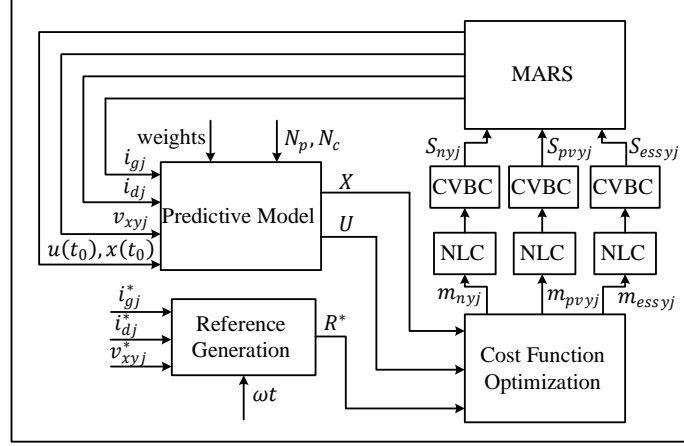


**Figure 6.2 – Schematic diagram of the proposed MPC method.**

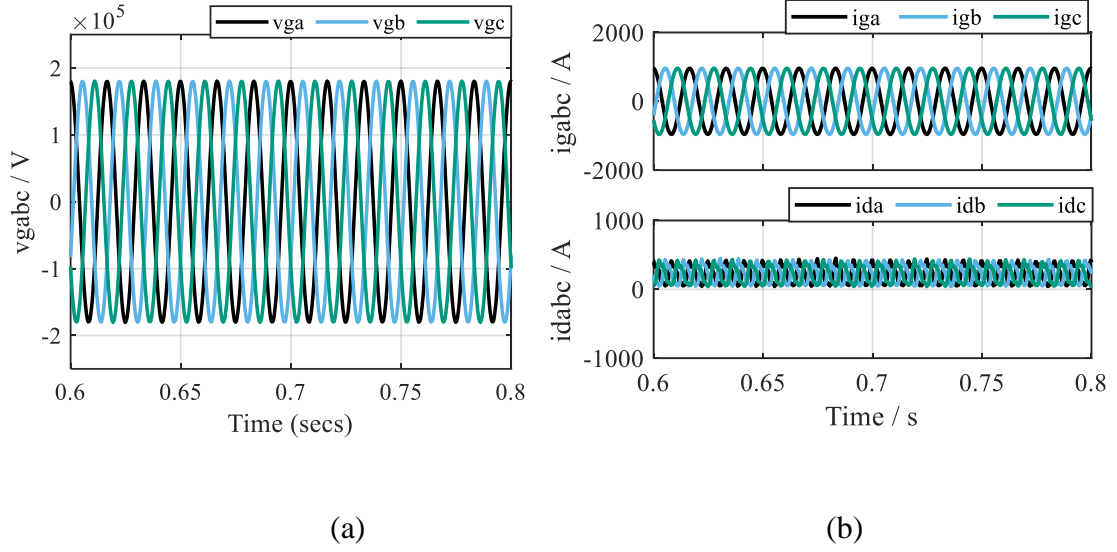
### 6.3 Performance Evaluation

The high-fidelity model of MARS constructed in PSCAD/EMTDC is used to demonstrate the proposed MPC method. Figure 4.3 gives the parameters of the scaled simulation prototype. The several combinations of predictive horizon and control horizon are tested, and the combination of  $N_p = N_c = 2$  gives the best performance without being unsolvable. The first scenario presented shows the steady state performance of the MPC. The second scenario showcases the dynamic performance of the proposed MPC. Finally, the third scenario offers insightful information about the behavior of the MARS under different grid events. The predefined range of the SM capacitor voltages is from 0.75 pu to 1.25 pu.

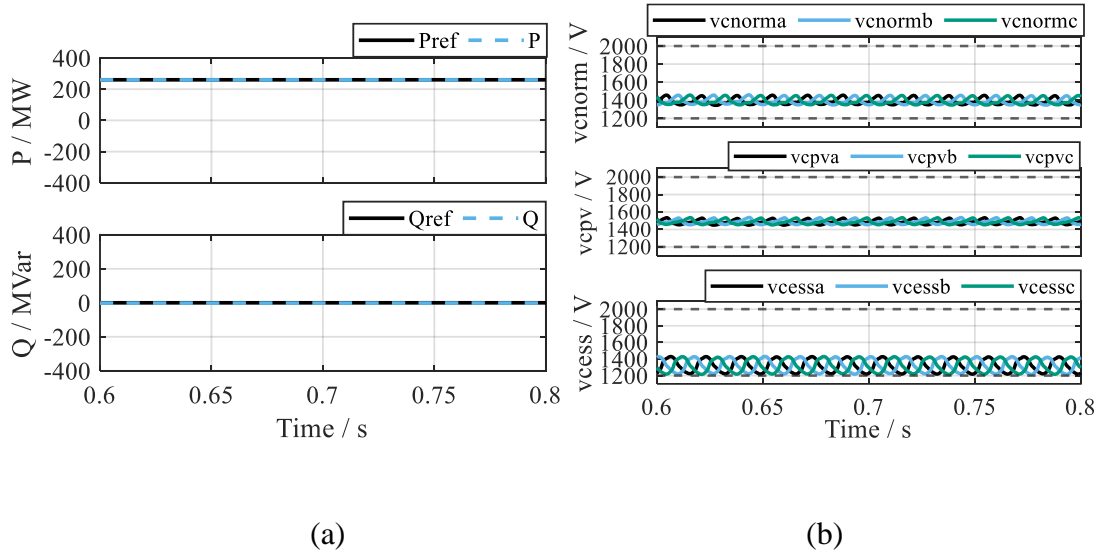
#### 6.3.1 Steady-State Performance

Figure 6.3 and Figure 6.4 show the simulation results regarding the steady state characteristics of the MARS with the proposed MPC method. The MARS system is operated under the operating condition:  $P_{ac}=260\text{MW}$ ,  $Q_{ac}=0$ , and  $P_{dc}=260\text{MW}$ . As can

be seen, the MARS system operates properly with a low THD of the grid side current and grid side voltage. The accuracy of the grid side current tracking its reference is controlled by the weight, and it is adjustable according to the desired performance of the system.



**Figure 6.3 – (a)The MARS grid-side measured three-phase voltages. (b) The MARS grid-side measured three-phase currents and circulating currents.**

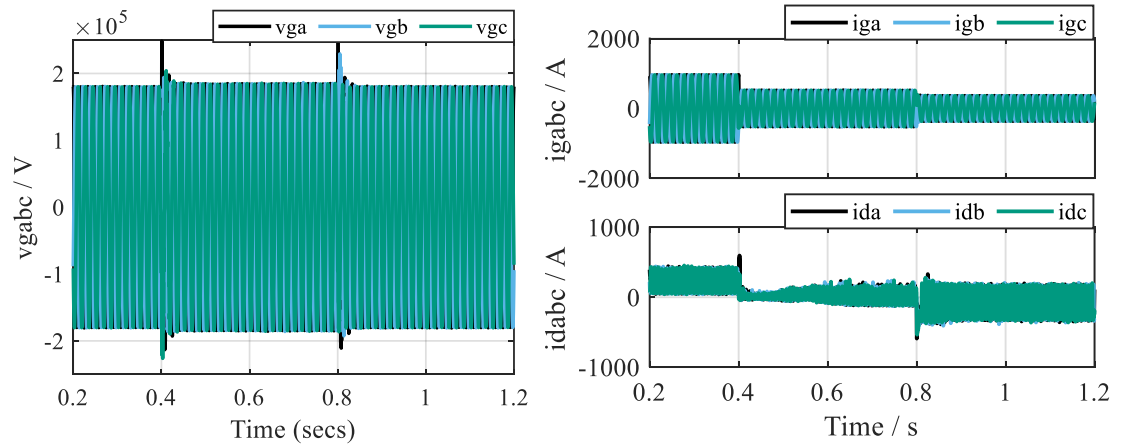


**Figure 6.4 – (a)The MARS grid-side active and reactive powers. (b) Capacitor voltages in representative SMs.**



### 6.3.2 Dynamic Performance

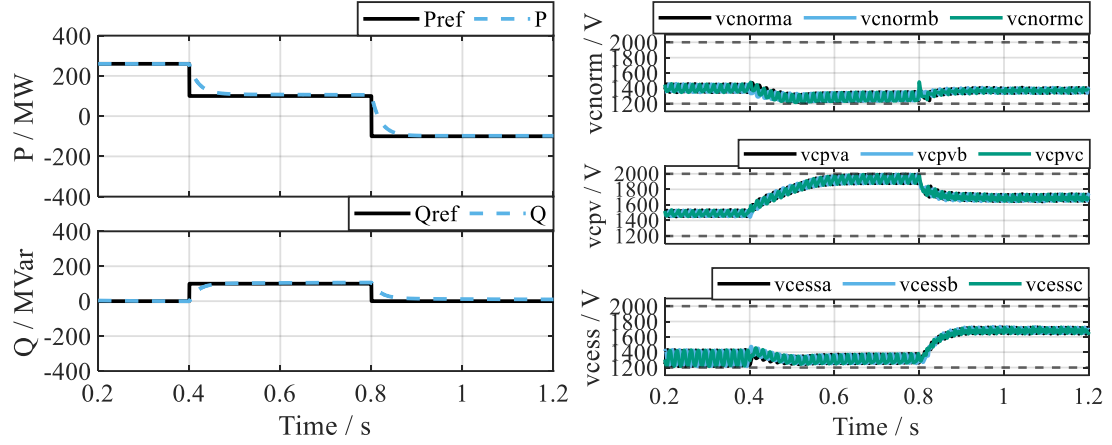
The test results for dispatch command steps from  $P_{ac}=260\text{MW}$ ,  $Q_{ac}=0$ , and  $P_{dc}=260\text{MW}$  to  $P_{ac}=100\text{MW}$ ,  $Q_{ac}=100\text{MVar}$ , and  $P_{dc}=-10\text{MW}$ , and  $P_{ac}=-100\text{MW}$ ,  $Q_{ac}=0$ , and  $P_{dc}=-230\text{MW}$  are shown in Figure 6.5 to Figure 6.7. The dynamic tests involve the operating condition changing from positive active power to negative active power, from operating condition that is viable for the system to operating condition which is not stable without the MPC. The results reinforce the successful operation of MARS system under various operating conditions and the dynamic performance in transitioning of different operating conditions. From Figure 6.6, it can be observed that the dispatch commands for  $P_{ac}$ , and  $Q_{ac}$  are being accurately followed. In addition, it can be observed that the grid side currents, different front-end half-bridge SM voltages are stable and within their respective limits. Figure 6.7 shows that the capacitor voltage at the PV side of the PV SM in the MARS real-time simulator follows its reference (which is sent to the L3 controller from the MARS L1-L2 controller) closely during steady state and step change of operating conditions. Similarly, the power of the ESS SM tracks the reference, and both the capacitor voltage at the ESS side and the inductor current are stable.



(a)

(b)

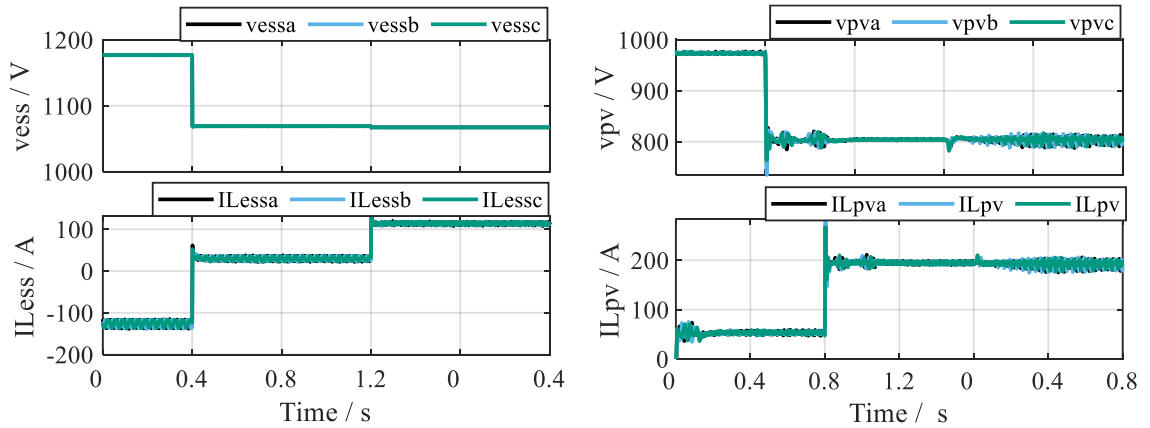
**Figure 6.5 – (a)The MARS grid-side measured three-phase voltage under various operating conditions. (b) The MARS grid-side measured three-phase currents and circulating current under various operating conditions.**



(a)

(b)

**Figure 6.6 – (a)The MARS grid-side active and reactive powers under various operating conditions. (b) Capacitor voltages in representative SMs under various operating conditions.**



(a)

(b)

**Figure 6.7 – One PV and ESS converter outputs.**

The total harmonic distortion (THD) of the grid current  $i_{gabc}$  is illustrated in Figure 6.8, where the step change in the reference power is applied. Due to the fact that the PI-based EBC combined with EBC criteria and NN-based EBC have similar performance regarding the grid current harmonic under system dynamics, only the THD ( $i_{gabc}$ ) of NN-based EBC is shown here. Since the NN-based EBC requires a longer time for initialization, different x-axis is used in Figure 6.8. It can be observed from Figure 6.8, the THD under steady state for both control methods is similar and is around 1.5%. The reference powers change from  $P_{ac}=260\text{MW}$ ,  $Q_{ac}=0$ , and  $P_{dc}=260\text{MW}$  to  $P_{ac}=100\text{MW}$ ,  $Q_{ac}=100\text{MVar}$ , and  $P_{dc}=-10\text{MW}$  at  $t=0.4\text{s}$  (MPC). And the expatiating condition changes from  $P_{ac}=100\text{MW}$ ,  $Q_{ac}=100\text{MVar}$ ,  $P_{dc}=-10\text{MW}$  to  $P_{ac}=-100\text{MW}$ ,  $Q_{ac}=0$ ,  $P_{dc}=-230\text{MW}$  at  $t=0.8\text{s}$  (MPC).it can be observed that the output grid current harmonic distortions are reduced by more than 50%, though using MPC. The transient recovery time is further reduced by a factor of ten for MPC compared with the NN-EBC. The comparisons in Figure 6.8 confirm the superior of the proposed MPC strategy to other advanced controls in terms of improving the dynamic response of the system.

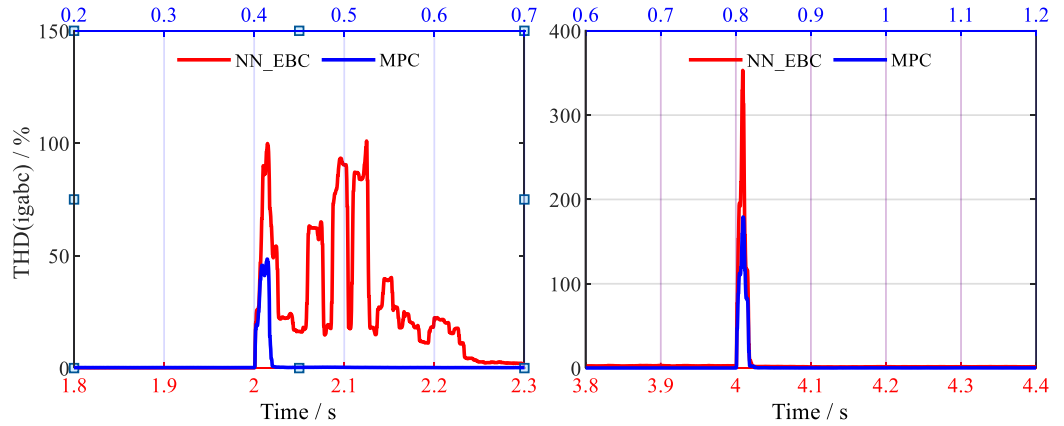


**Figure 6.8 – (a) THD of grid side current during change of the reference power :  $P_{ac}=260\text{MW}$ ,  $Q_{ac}=0$ ,  $P_{dc}=260\text{MW}$  to  $P_{ac}=100\text{MW}$ ,  $Q_{ac}=100\text{MVar}$ ,  $P_{dc}=-10\text{MW}$ ; (b) THD of grid side current during change of the reference power  $P_{ac}=100\text{MW}$ ,  $Q_{ac}=100\text{MVar}$ ,  $P_{dc}=-10\text{MW}$  to  $P_{ac}=-100\text{MW}$ ,  $Q_{ac}=0$ ,  $P_{dc}=-230\text{MW}$ .**

### 6.3.3 Robustness Performance Analysis

In order to further quantify the robust performance of the proposed methodology, a thorough analysis of the effect of different grid events is illustrated in Figure 6.9 to Figure 6.12, corroborating the effectiveness of the proposed MPC. Meanwhile, the THD of two different control methods is also investigated and given in Figure 6.13. As depicted, it can be observed that the proposed solution allows significantly better (>50% improvement) grid-side current THD than that of the state-of-the-art PI-based EBC scheme in chapter 4 and NN based EBC in chapter 5 under different grid events. However, it presents a relatively higher circulating current magnitude than the NN-based EBC leading to a higher system loss. This is expected to be further improved with the optimum weight tuning of the MPC. Consequently, this test proves the capability of the proposed MPC strategy to enhance the system robustness under system dynamics.

#### 6.3.3.1 Three Phase to Ground Fault

The dynamic response of the MARS system and the performance of the proposed MPC are studied under a temporary three-phase to ground fault. Initially, the system operates in a steady state condition, with operating condition  $P_{ac}=100\text{MW}$ ,  $Q_{ac}=100\text{MVar}$ ,  $P_{dc}=-10\text{MW}$ , a three-phase to ground fault is imposed at WECC system connected to the MARS at  $t=0.5\text{s}$  and lasts for  $0.2\text{s}$ . After  $0.2\text{s}$ , the fault is self-cleared. Figure 6.9 shows the corresponding changes in the ac-side currents and voltage. It can be observed that the

MARS system with MPC can provide continuity of operation successfully during the fault and operates in a stable mode of operation during post-fault conditions.

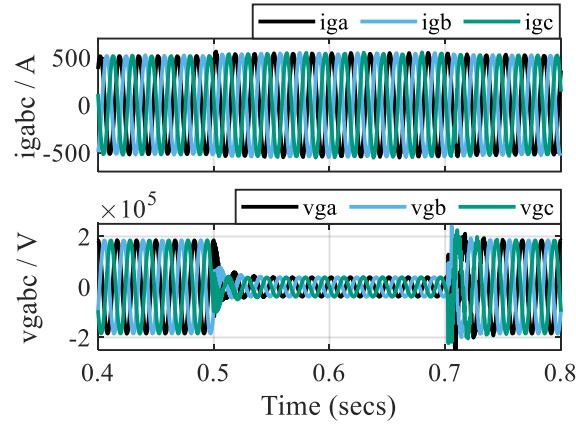


**Figure 6.9 – The MARS grid-side measured three-phase voltages and currents under three-phase to ground fault.**

#### 6.3.3.2 The Line-to-Line Fault

A line-to-line fault is simulated on the transmission line between the grid and the MARS system at  $t = 1.0$  s with a fault duration of 0.2 s. After 0.2 s, the fault is self-cleared. It can be observed that the MARS system can provide continuity of operation successfully during the fault and operates in a stable mode of operation during post-fault conditions.

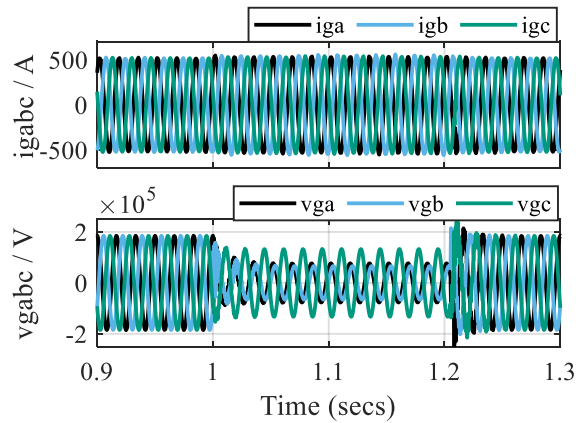


**Figure 6.10 – The MARS grid-side measured three-phase voltages and currents under a line-to-line fault.**

### 6.3.3.3 Loss of Generation Event

An event of 804.44 MW loss of generation in the WECC is simulated at  $t=1.5$ s. The grid side ac current and voltage shown in Figure 6.11 (a) remain intact. The frequency response measured at Pittsburg is shown in Figure 6.11 (b). It can be observed that the MARS system can provide continuity of operation successfully during the loss of generation event and operates in a stable mode of operation during post-event conditions.

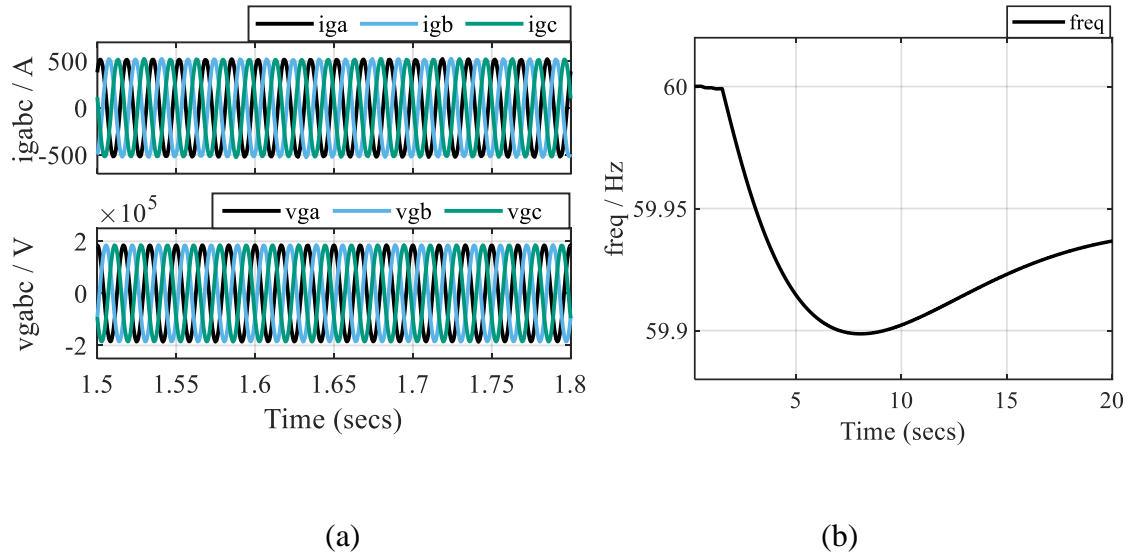


**Figure 6.11 – (a)The MARS grid-side measured three-phase voltages and currents under loss of generation event. (b)Ac-side grid frequency.**

Figure 6.12 shows the capacitor voltages of each type of SMs of phase A are very well regulated within the upper and lower limit within the dashed line, even during the fault. The simulation results verify the robustness of the proposed MPC, and the overall MARS control system is able to control grid side voltage and current, and balance the SM capacitor voltages even under severe conditions.

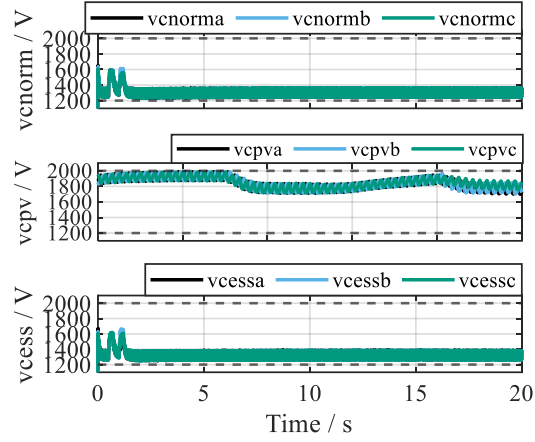


**Figure 6.12 – Capacitor voltages in representative SMs under various operating conditions.**

#### 6.3.3.4 Dynamic Response Comparison

Since the system with NN EBC requires longer time to stabilize, the three phase to ground fault is imposed at  $t=0.5s$  under MPC control, while the fault is applied at  $t=2s$  under NN EBC. The fault is clear after  $0.2s$ . At  $t=1s$ , a line-to-line fault is applied to the WECC system connected to the MARS with MPC. Similarly, a line-to-line fault is applied to the MARS with NN EBC. At  $t=1.5s$  and  $t=3s$ , the loss of generation happens for the MARS system with MPC and with NN EBC respectively. The THD of  $i_{gabc}$  with PI-based EBC is similar to the THD ( $i_{gabc}$ ) under NN-based EBC and is not shown here. Under both steady-state responses and the dynamic responses, The MPC offers a better performance compared to the NN-based EBC in Figure 6.10. The transient response time of MPC is more than twice as faster than the NN-based EBC and the THD is 3 times smaller than the THD of the NN-based EBC. These are significant improvements in the dynamic response and the robustness of the MARS under transient conditions with the implementation of the MPC.

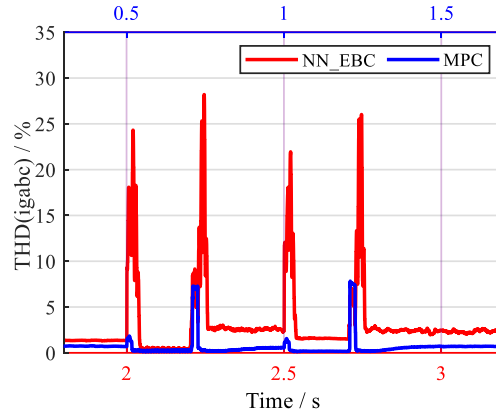


**Figure 6.13 – Comparison of THD ( $i_{gabc}$ ) during grid event with the implementation of the MPC and NN-based EBC.**

## 6.4 Summary

In this chapter, an MPC strategy is proposed and designed for the MARS system, which has multiple types of SMs in each arm. The MPC is designed based on the linearized discrete-time mathematical model of the MARS, enforcing the constraints of the modulation index, grid current, circulating current, and the SM capacitor voltages of ensemble PV SMs, normal SMs, and ESS SMs. In this way, the SM capacitor voltages under arbitrary operating conditions can be guaranteed to be stable. The cost function associated with the internal control objectives, i.e., tracking the grid-side current, minimizing the circulating current, and balancing the SM capacitor voltages, is minimized using a quadratic optimization solver.

The effectiveness of the proposed control strategy for the MARS under various operating conditions and different grid events is evaluated based on simulation studies in the PSCAD/EMTDC. The study results highlight the significant improvements in terms of dynamic response in the MARS control with MPC. The MPC offers a twice fast dynamic



response compared to other advanced methods proposed in this thesis and twice smaller THD of grid-side current during the transient states. The MPC is suitable for the MARS and MARS-type systems where strict performance requirements and faster convergence to steady states are needed.

## **CHAPTER 7. CONCLUSION AND FUTURE WORK**

### **7.1 Conclusion**

The fast growth of high-power grid-connected MMC-based hybrid systems has motivated extensive research efforts toward resolving the technical challenges of controlling such systems. The main objective of this thesis is to address some of the technical concerns related to the control of MARS, which is a typical grid-connected MMC-based hybrid system.

In this thesis, the SM capacitor voltage disparity of an MMC system with multiple external sources is discussed and explored in chapter 4. In such a system, the capacitor voltage disparity under some of the operating conditions originates from the limited capability of the capacitor voltage balancing algorithm, low dc power, and/or low reactive power. This issue of SM capacitor voltage disparity is addressed by the EBC, which injects a fundamental circulating current. However, implementing the EBC introduces extra power losses and increases the switching frequency for the operating conditions that are viable without the EBC. Thus, in this thesis, the operation boundary of the stable/unstable operating conditions is accessed through two types of machine learning algorithms. The machine learning algorithms can avoid complicated analytical derivation and achieve 97% accuracy in determining whether the EBC is necessary under given operating conditions. The RF and ANN ML algorithms are compared from training methods, utilization in the cHIL test, and accuracy perspectives. The ANN algorithm outperforms the RF and is implemented in both the PSCAD software and the cHIL platform. The PSCAD/EMTDC

simulation results showcase the power and switching frequency reduction obtained with the EBC criteria under 2,500 operating conditions. The cHIL experiments show the capacitor voltage disparity under several operating conditions and then demonstrate how those operating conditions become viable after enabling the EBC. The mechanism of the capacitor voltage imbalance has been further verified by the cHIL test, and the relationships between the system stability, reactive power, and dc power are investigated. In addition, the cyclic test fully demonstrates the system's stable operation under different power references with the implementation of the EBC and the EBC criteria in the MARS control. The proposed EBC method along with the EBC criteria, are applicable to an MMC system with any size in which a number of SMs include external power sources/inputs such as ESS, PV, wind, or a combination of them. With the help of the EBC, the operating region of the system can be extended, while improved efficiency and reduced switching frequency can be achieved by implementing the EBC criteria.

In chapter 5, a power mismatch elimination control consisting of a power reference generator and an NN-based EBC control is proposed for the MARS system to ensure stable operation under arbitrary operating conditions. The NN-based EBC acts as an alternative method to calculate the proper circulating current references in a feasible and computationally efficient way compared with the traditional PI-based control. It avoids the complicated tuning process, efficiently eliminates the power mismatch and balances the capacitor voltages under different conditions. Both the ANN and NARX algorithms are developed to learn the dynamics of the system and map the relationship between the circulating current and the capacitor voltage differences. Analytical analyses are also performed for inter-SM power mismatch elimination, inter-phase power mismatch

elimination, and inter-arm power mismatch elimination. The ESS is employed in the power mismatch control strategy to smooth the output power, compensate for the power mismatch, and avoid unnecessary system loss caused by the circulating current. The inter-arm and inter-phase power mismatches are tested using the MARS PSCAD/EMTDC model with the PSCAD/MATLAB interface to implement the NN-based EBC. Simulation results demonstrate the effectiveness of the proposed method under partial shading. The cHIL experimental results show that the proposed method can achieve capacitor voltage balancing and improve the system efficiency compared to the traditional PI control. In addition, the performance of the NN-based EBC control under different grid events is verified under various operating conditions, which further demonstrates the stability of the proposed control.

An MPC of MARS is proposed in chapter 6 for a more accurate and efficient control of the grid side current, circulating current, and the capacitor voltage balancing of different types of SMs. A model predictive controller is suitable for the control of MARS since it can easily handle the constraints imposed by integrating ESS and PV to the SMs and can help comply with the grid side current harmonic limits set by the grid code. An improved MPC is proposed in this thesis to optimally allocate uneven power of ESS and PV in one arm and counteract capacitor voltage deviations. Unlike the existing PI-based control, the proposed method can provide optimized low circulating current while maintaining the capacitor voltages within the upper and lower limits through proper tuning of the weights. In addition, it improves the THD of the ac side grid current. The case studies justified the superiority of the proposed method in terms of the system dynamic response.

The comparison of control performance with all proposed methods is roughly presented in Figure 7.1. Meanwhile, the operating region, system loss, design complexity, etc., are investigated and given in Table 7.1. As depicted, the proposed MPC strategy has the fastest dynamic response while the average system loss is also high. The average improvement of MPC regarding the dynamic response time and the THD of grid current during transient is 0.5x compared with other methods. Even though the NN-based EBC has the lowest avg system loss, the system dynamic performance is worse than the MPC. Finally, it can, thus, be concluded that the proposed model predictive control and the NN-based EBC have their own advantages and are overall superior to other methods. Depending on the different system requirements, the MPC and the NN-based EBC can be chosen for the MARS-type hybrid system.

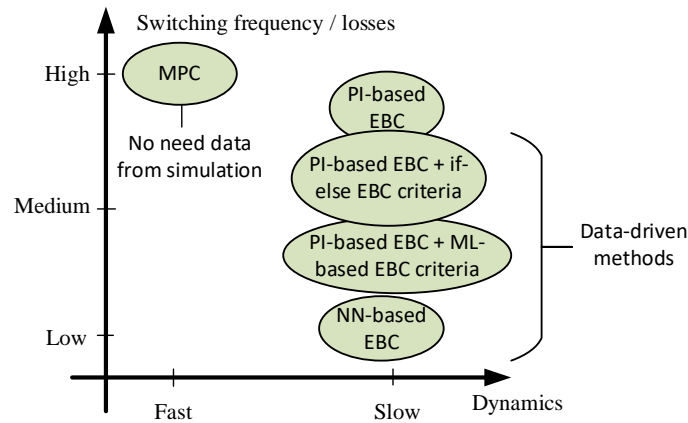


**Figure 7.1 – Comparison of different control strategies regarding the system loss and the system dynamics.**

**Table 7.1 – Comparison of different control strategies.**

	Benchmark control	PI-based EBC & if- else EBC criteria	PI based EBC and ML based EBC criteria	NN based EBC	MPC
Operating region	~50% operating conditions are not viable for the system.	Stable under all operating condition.	Stable under all operating condition.	Stable under all operating condition.	Stable under all operating condition.
System loss reduction compared to PI-based EBC	Not applicable	Average power loss reduction is 0.38MW	Average power loss reduction is 0.55MW	Average power loss reduction is 0.67MW	Higher than the PI based EBC.
Design complexity	Low	High	Medium	Medium	Low
System robustness under grid event	Not applicable	High	High	High	High

TDD ( $i_{gabc}$ ) under steady state.	Not applicable	0.118%	0.118%	0.118%	0.118%
Data set required	No	YES	YES	YES	No
Dynamic response time compared with NN- based EBC	Not applicable	~1x	~1x	~1x	~2x
THD ( $i_{gabc}$ ) under dynamics compared with NN- based EBC	Not applicable	~1x	~1x	~1x	~2x

## 7.2 Contributions

The SM capacitor voltage is first observed when testing the traditional controller of MARS under the operating condition of  $P_{ac}=100\text{MW}$ ,  $P_{dc}=30\text{MW}$ , and  $Q_{ac}=0$ . After that, more unstable operating conditions are found with conventional control of MARS at Pittsburg (400MW system rating) and MARS designed for another location of Victorville (1000MW system rating). It can be deduced that the SM capacitor voltage disparity exists

in most MMC-based systems with multiple or partially distributed energy in one arm. The phenomena of the SM capacitor voltage disparity along with the high dc power ripples impact the reliability and limit the operating region of MMC-based hybrid systems like MARS.

To understand the SM capacitor voltage disparity, the limit of the conventional capacitor voltage balancing algorithm is explored. The simulation results show that increasing the sorting frequency can help more operating conditions become viable for the system with conventional control. However, even with the highest sorting frequency, some unstable operating conditions still exist. The causes of the SM capacitor voltage disparity are also analyzed, and the variables with a high correlation to the defined SM capacitor voltage differences  $\sum(V_{c\sigma})^2$  are explored and studied. Thus, EBC addresses the inter-SM power mismatch issue is proposed.

Since the functioning of EBC keeps injecting circulating current under all operating conditions, increasing the switching frequency and reducing the system efficiency, ML-based EBC criteria are proposed to disable the EBC when it is unnecessary. It is necessary to explore the system's operating region when implementing the EBC criteria. The introduction of ML is due to the complexity of the operating region analytic derivation, and ML has its advantages when studying complicated nonlinear systems. A more efficient NN-based EBC is proposed to replace the ML-based EBC criteria and PI-based EBC with 64% operating conditions having improved circulating current magnitude and almost the same CPU utilization in real-time simulation. The dissertation is also the first to propose an MPC with multiple types of SMs and achieve better performance in terms of grid current compared to the NN-based EBC.



The discussion power mismatch caused by the partial shedding is unavoidable for an MMC-based hybrid system with PV and ESS. The proposed power mismatch elimination strategy is capable of mitigating leg and arm power mismatches in the MARS without altering the terminal voltage of the converter.

The data-driven control methods proposed requires large samples and thus increase the complexity of the control design process. Thus, a linearization based MPC is proposed in this thesis to improve the system robustness and the dynamic response. It is the first time to utilize MPC in the MMC-based system with uneven distribution of external source in each arm. The biggest challenge is the assumption that all capacitor voltages are balanced is not valid, and thus, the complexity of the system due to the large switching state optionally increased. This challenge is addressed in this thesis.

To provide extensive validation of the work, the high-fidelity model of MARS is implemented using PSCAD/EMTDC. The cHIL is also designed and implemented to validate the developed theory and ensure the viability of the controller.

### **7.3 Future Work**

The research presented in this dissertation can be improved from the following aspects in the future:

- Implement nonlinear MPC for the nonlinear model of MARS and compare the performance of the nonlinear MPC with the linearization-based MPC proposed in this thesis.

- The nonlinear MPC is not suitable for small-time step simulations. Thus future investigation will be to further improve the computationally efficiency by deploying an ML solution for MPC. The ML model can be trained using the data generated from MPC to achieve similar performance to the nonlinear MPC. At the same time, the computational cost is reduced due to the computation-light characters of ML.
- Explore the robustness of the MARS against ESS failures or PV failures by assessing the power balance between submodules when a subset of ESSs or PV panels is not operational.

## APPENDIX A. DESCRIPTION OF DEFAULT SUBHEADING SCHEME

### A.1 PV SM dc-dc Control

The IV characteristic curve of the PV panel is simplified to a 5-point extrapolating curve, and for the small signal analysis, the PV input current  $i_{pv}$  and the capacitor voltage follows the following relationship:

$$i_{pv} = m_{pv} v_{cpv} \quad (\text{A.1})$$

where  $m_{pv}$  is defined as  $m_{pv} = \frac{-i_3 + I_{mp}}{v_3 - V_{mp}}$ .

Thus, after considering the relationship, the small signal model of the PV indirect active interface is given by:

$$\begin{bmatrix} \dot{i}_{Lpv} \\ \dot{v}_{cpv} \end{bmatrix} = \underbrace{\begin{bmatrix} 0 & 1/L \\ -1/C & m_{pv}/C \end{bmatrix}}_A \underbrace{\begin{bmatrix} i_{Lpv} \\ v_{cpv} \end{bmatrix}}_x \quad (\text{A.2})$$

$$+ \underbrace{\begin{bmatrix} \overbrace{V_{sm}/L}^{B_1} \\ 0 \end{bmatrix} d + \begin{bmatrix} \overbrace{-(1-D)/L}^{B_2} & 0 \end{bmatrix} v_{sm}}_{B.u}$$

$$i_{Lpv} = \underbrace{\begin{bmatrix} 1 & 0 \end{bmatrix}}_{C_1} \begin{bmatrix} i_{Lpv} \\ v_{cpv} \end{bmatrix} \quad (\text{A.3})$$

$$v_{Cpv} = \underbrace{[0 \quad 1]}_{C_2} \begin{bmatrix} i_{Lpv} \\ v_{Cpv} \end{bmatrix} \quad (\text{A.4})$$

From the state space equations (A.2), (A.3), and (A.4), the open-loop transfer functions  $G_1(s) = \frac{i_{Lpv}(s)}{d_{pv}(s)}$  is obtained as:

$$G_1(s) = C_1(sI - A)^{-1}B_1 \quad (\text{A.5})$$

$$= [1 \quad 0] \left( \begin{bmatrix} s & 0 \\ 0 & s \end{bmatrix} - \begin{bmatrix} 0 & 1/L \\ -1/C & m_{pv}/C \end{bmatrix} \right)^{-1} \begin{bmatrix} V_{sm}/L \\ 0 \end{bmatrix}$$

Rewriting (A.5),  $G_1(s)$  is obtained as:

$$G_1(s) = C_1(sI - A)^{-1}B_1 = \frac{(s - m_{pv}/C)(V_{sm}/L_{pv})}{s^2 - \frac{m_{pv}}{C}s + \frac{1}{L_{pv}C_{pv}}} \quad (\text{A.6})$$

The characteristic equation is  $s^3 - \frac{m_{pv}}{C_{pv}}s^2 + \frac{1}{L_{pv}C_{pv}}s + \frac{K_p V_{sm}}{L_{pv}}s^2 + \frac{K_i V_{sm}}{L_{pv}}s - \frac{K_p V_{sm} m_{pv}}{L_{pv} C_{pv}}s - \frac{K_i V_{sm} m_{pv}}{L_{pv} C_{pv}}$ .

The outer-loop transfer function is obtained from:

$$G_2(s) = \frac{v_{cpv}(s)}{i_{Lpv}(s)} = \frac{\frac{v_{cpv}(s)}{d(s)}}{\frac{i_{Lpv}(s)}{d(s)}} = \frac{G_0(s)}{G_1(s)} \quad (\text{A.7})$$

$$G_0(s) = C_2(sI - A)^{-1}B_1 = \frac{-V_{sm}/L_{pv}}{s^2 - \frac{m_{pv}}{C_{pv}}s + \frac{1}{L_{pv}C_{pv}}} \quad (\text{A.8})$$

Substituting (A.6) and (A.8) and into (A.7),  $G_2(s)$  is obtained as:

$$G_2(s) = \frac{G_0(s)}{G_1(s)} = \frac{-1/L_{pv}}{s - \frac{m_{pv}}{C_{pv}}} \quad (\text{A.9})$$

The gains of the L3 PV outer loop controller  $K_{P,pv,out}$  and  $K_{I,pv,out}$  are tuned using the characteristic equation  $s^2 + (\frac{K_{P,o}-m_{pv}}{C_{pv}})s + \frac{K_{I,o}}{C_{pv}}$  such that the settling time  $t_s$  is an order of magnitude greater than the settling time of the inner loop.

$$K_{P,pv,out} = \frac{\frac{-8C_{pv}}{t_s} - m_{pv}}{C_{pv}} \quad (\text{A.10})$$

$$K_{I,pv,out} = \frac{(K_{P,pv,out} - m_{pv})^2}{4\omega^2 C_{pv}} \quad (\text{A.11})$$

where  $\omega$  is the natural frequency.

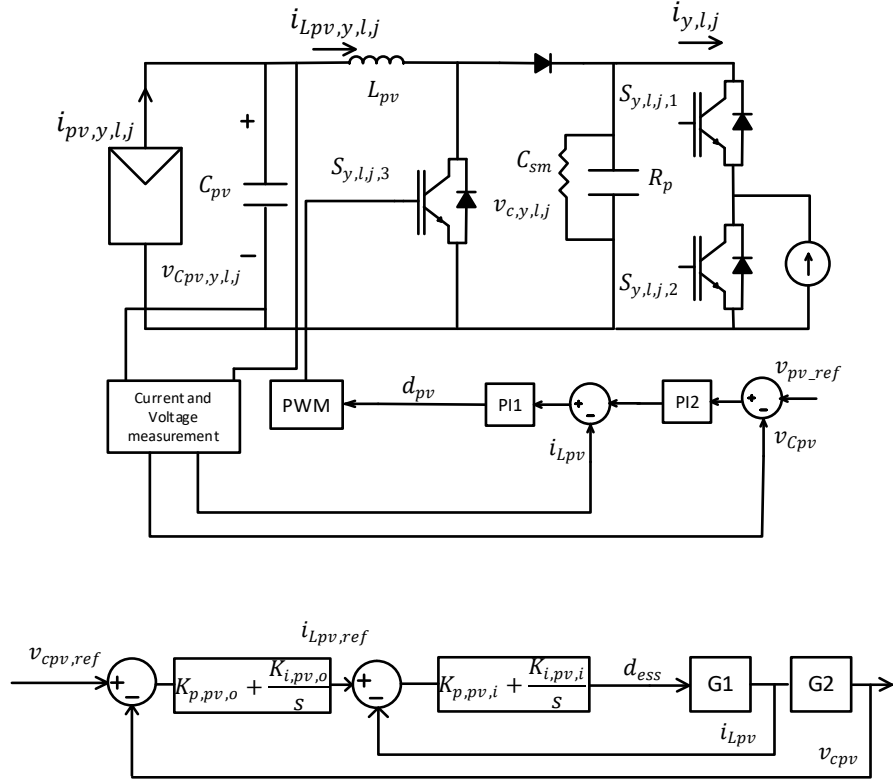


**Figure A.1 – Block diagram of L3 PV controller.**

## A.2 ESS SM dc-dc Control

$$\frac{dP_{ess}}{dt} = \frac{dv_{Cess}i_{Less}}{dt} = v_{Cess} \frac{di_{Less}}{dt} + i_{Less} \frac{dv_{Cess}}{dt} \quad (A.12)$$

When  $S_{y,i,j,3}$  is on,  $S_{y,i,j,4}$  is off and,

$$\frac{di_{ess}}{dt} = \frac{v_{Cess}}{L_{ess}} \quad (A.13)$$

$$\frac{dv_{Cess}}{dt} = \frac{i_{ess}}{C_{ess}} - \frac{i_{Less}}{C_{ess}} \quad (A.14)$$

When  $S_{y,i,j,3}$  is off,  $S_{y,i,j,4}$  is on,

$$\frac{di_{ess}}{dt} = \frac{v_{Cess} - v_{sm}}{L_{ess}} \quad (A.15)$$

$$\frac{dv_{Cess}}{dt} = \frac{i_{ess}}{C_{ess}} - \frac{i_{Less}}{C_{ess}} \quad (A.16)$$

$$\begin{aligned} \frac{dP_{ess}}{dt} = & d * \left( \frac{v_{Cess}^2}{L_{ess}} + \frac{(i_{ess} - i_{Less})i_{Less}}{C_{ess}} \right) + (1 \\ & - d) \left( \frac{v_{Cess}(v_{Cess} - v_{sm})}{L_{ess}} + \frac{(i_{ess} - i_{Less})i_{Less}}{C_{ess}} \right) \end{aligned} \quad (A.17)$$

$$i_{ess,ref} = K_{P,ess,out}(P_{ess,ref} - P_{ess}) + \frac{K_{I,ess,out}}{s}(P_{ess,ref} - P_{ess}) \quad (A.18)$$

$$\frac{di_{ess,ref}}{dt} = -K_{P,ess,out} \frac{dP_{ess}}{dt} + K_{I,ess,out}(P_{ess,ref} - P_{ess}) \quad (A.19)$$

Similarly,

$$i_{ess,ref} = K_{P,ess,out}(P_{ess,ref} - P_{ess}) + \frac{K_{I,ess,out}}{s}(P_{ess,ref} - P_{ess}) \quad (A.20)$$

$$d_{ess} = K_{P,ess,in}(i_{ess,ref} - i_{ess}) + \frac{K_{I,ess,in}}{s}(i_{ess,ref} - i_{ess}) \quad (A.21)$$

$$\frac{d(d)}{dt} = -K_{P,ess,in} \frac{dP_{ess}}{dt} + K_{I,ess,in}(P_{ess,ref} - P_{ess}) \quad (A.22)$$

variable  $x = v_{Cess}, i_{Less}, P_{ess}, i_{ess}$

$$x = X + \tilde{x} \quad (A.23)$$

where  $X$  and  $\tilde{x}$  represent the dc operating point and the low-frequency ac terms of  $x$ , respectively. Decomposing  $v_{C_{ess}}$ ,  $i_{ess}$ ,  $i_{ess,ref}$ , and  $P_{ess}$  based on (A.23) and substituting for them in (A.17), yields:

$$\frac{d\tilde{P}_{ess}}{dt} = \frac{i_{L_{ess}}\tilde{i}_{ess}}{C_{ess}} + \frac{i_{ess}\tilde{i}_{L_{ess}}}{C_{ess}} - \frac{2i_{L_{ess}}\tilde{i}_{L_{ess}}}{C_{ess}} + \frac{v_{sm}v_{C_{ess}}\tilde{d}}{L_{ess}} \quad (A.24)$$

$$i_{ess,ref} = K_{P,ess,out}(P_{ess,ref} - P_{ess}) + \frac{K_{I,ess,out}}{s}(P_{ess,ref} - P_{ess}) \quad (A.25)$$

From Figure A.2,  $i_{ess,ref}$  can be formulated as:

$$\frac{di_{ess,ref}}{dt} = -K_{P,ess,out}\frac{dP_{ess}}{dt} + K_{I,ess,out}(P_{ess,ref} - P_{ess}) \quad (A.26)$$

Decomposing  $i_{ess,ref}$ , and  $P_{ess}$  based on (A.23) and substituting for them in (A.25), yields:

$$\frac{d\tilde{i}_{ess,ref}}{dt} = -K_{P,ess,out}\frac{d\tilde{P}_{ess}}{dt} - K_{I,ess,out}\tilde{P}_{ess} \quad (A.27)$$

$$s\tilde{i}_{ess,ref} = \frac{\tilde{v}_{C_{ess}}}{L_{ess}} \quad (A.28)$$

$$\begin{aligned} & + \frac{V_{sm}}{L_{ess}} \left[ K_{P,ess,in}(\tilde{i}_{ess,ref} - \tilde{i}_{ess}) \right. \\ & \left. + \frac{K_{I,ess,in}}{s}(\tilde{i}_{ess,ref} - \tilde{i}_{ess}) \right] = A_1\tilde{i}_{ess,ref} + B_1\tilde{P}_{ess} \end{aligned}$$

$$s\tilde{P}_{ess} = A_2\tilde{i}_{ess,ref} + B_2\tilde{P}_{ess} \quad (A.29)$$



where

$$A_1 = -\frac{V_{sm}}{L_{ess}} \left( K_{P,ess,in} + \frac{K_{I,ess,in}}{s} \right)$$

$$A_2 = \left( -\frac{i_{ref}}{C_{ess}} - \frac{V_{sm}V_{cess}}{C_{ess}} \right) \left( K_{P,ess,in} + \frac{K_{I,ess,in}}{s} \right)$$

$$B_1 = -\frac{V_{sm}}{L_{ess}} \left( K_{P,ess,in} + \frac{K_{I,ess,in}}{s} \right) \left( K_{P,ess,out} + \frac{K_{I,ess,out}}{s} \right)$$

$$B_2 = -\left[ \frac{V_{cess}V_{sm}}{C_{ess}} \left( K_{P,ess,in} + \frac{K_{I,ess,in}}{s} \right) + \frac{I_{Less}}{C_{ess}} \right] \left( K_{P,ess,out} + \frac{K_{I,ess,out}}{s} \right)$$

The characteristic equation is  $(s - A_1)(s - B_2) - A_2B_1$ , and the settling time is obtained by analyzing the poles that can affect the settling. The poles that are located too far away are neglected. The settling is close to the first order case. The settling time of the ESS control are designed based on the following restriction:

$$t_{s,ess} \ll t_{s,EBC}$$

Thus, the L3 control loop and the L1 control loop can be decoupled when designing the parameters of the PI controller.

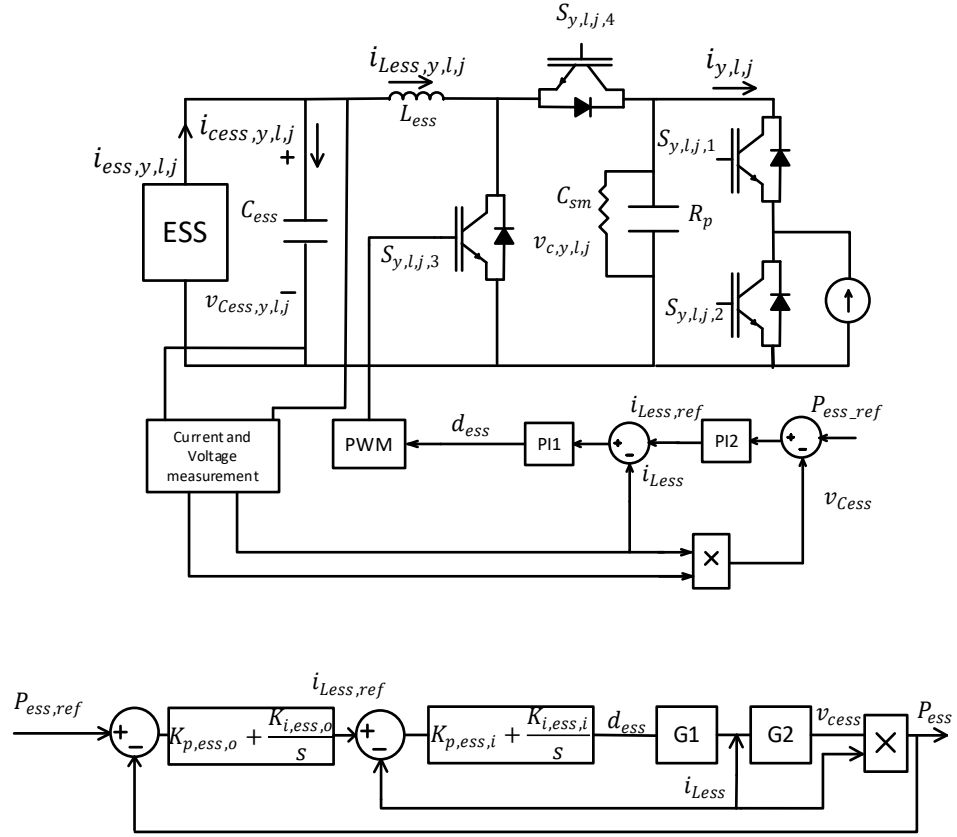


**Figure A.2 – Block diagram of L3 ESS controller.**

## **APPENDIX B. STANDARD COMPLIANCE OF THE MARS**

The MARS, with hundreds to thousands SMs, incorporate a complex hierarchical control system. Experiments are designed and performed to test the stability and performance of the hierarchical control system. In practice, the L1-L2 controller of the hierarchical control system will be implemented in the CPU-FPGA, while the L3 controller is in the hundreds-thousands of DSPs. To evaluate the hierarchical control system of the MARS, a unique power electronic hardware-in-the-loop (PE-HIL) real-time architecture is proposed. The PE-HIL, as shown in Figure B.1, consists of the MARS real-time simulator and the MARS controller. The MARS real-time simulator consists of the ac grid (179-bus WECC grid model) and the MARS interface, simulated in the CPU of OPAL-RT's OP5707 platform; The MARS PV and ESS SMs' model and their associated L3 controller are developed in the FPGA of the real-time simulation platform. The detailed information on the dc-dc converter FPGA model is introduced in [81]. Only one L3 controller that controls the PV/ESS SM's dc-dc converter is implemented in the DSP to achieve a low-cost evaluation of the control architecture. The L3 controller in the DSP receives measured input voltage and inductor current via analog copper I/Os from the PV/ESS dc-dc converter in the FPGA of the real-time simulator, and the command of PV voltage/ESS power reference is sent from L2 controllers through digital communication. In the open loop PE-HIL test, the active power/voltage reference (based on if ESS or PV SM's L3 controller is being tested) is not sent to the one L3 controller in DSP. After receiving the PV voltage/ESS power reference from the MARS L1-L2 controller, the L3 controller sends switching signals to the PV DAB module / ESS module in the MARS real-time simulator.

Both L1 and L2 controllers are located in the OPAL-RT's OP4510 simulator, while the L1 controller is in the CPU and the L2 controller is in the FPGA. The communication between the MARS L1-L2 controller and the MARS real-time simulator uses copper I/Os and SPF. Copper I/Os are used for the MARS real-time simulator to exchange measurement data with the L1 controller. The data includes measured arm currents, dc-side voltage, and ac-side voltages. In total, ten channels of analog I/Os are mapped to exchange system-level signals between the control system and real-time simulation platform. The SPF is used to send the measured front-end half-bridge capacitor voltage in each SM, arm currents, and maximum power available in PV to the L2 controller in the FPGA. In addition, the SFP sends the switching commands, and active power reference/voltage reference to the ESS SMs'/ PV SMs' L3 controllers in real-time simulator from the L2 controller. The PE-HIL test setup is shown in Figure B.2. The one L3 controller in physical implementation completes the evaluation process of the single PV SM/ESS SM controlled by the physical L3 controller, thus enables the characterization of the hierarchical control system of the MARS.

The open loop PE-HIL testbed described above is used to test the standard compliance of the MARS.

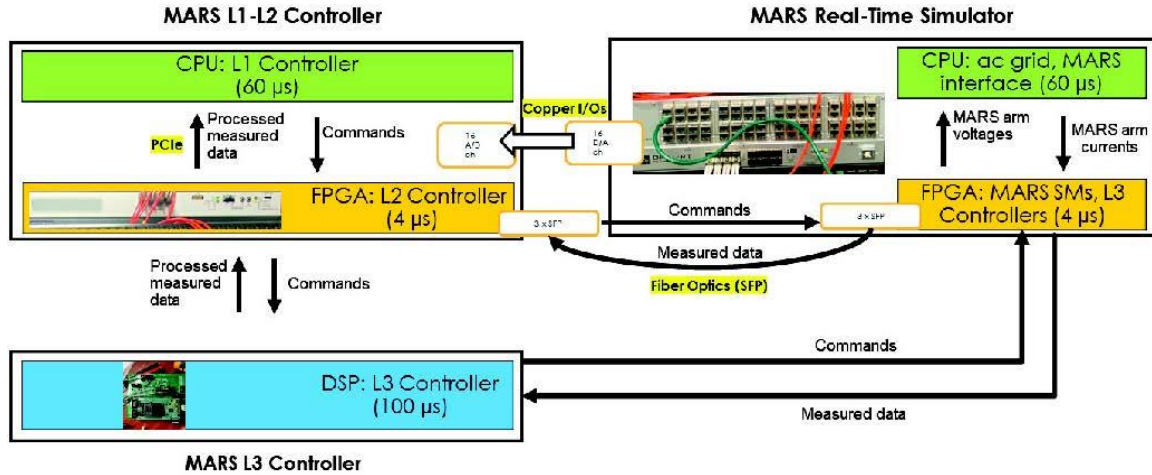


**Figure B.1 – PE-HIL setup to evaluate hierarchical control system of the MARS.**

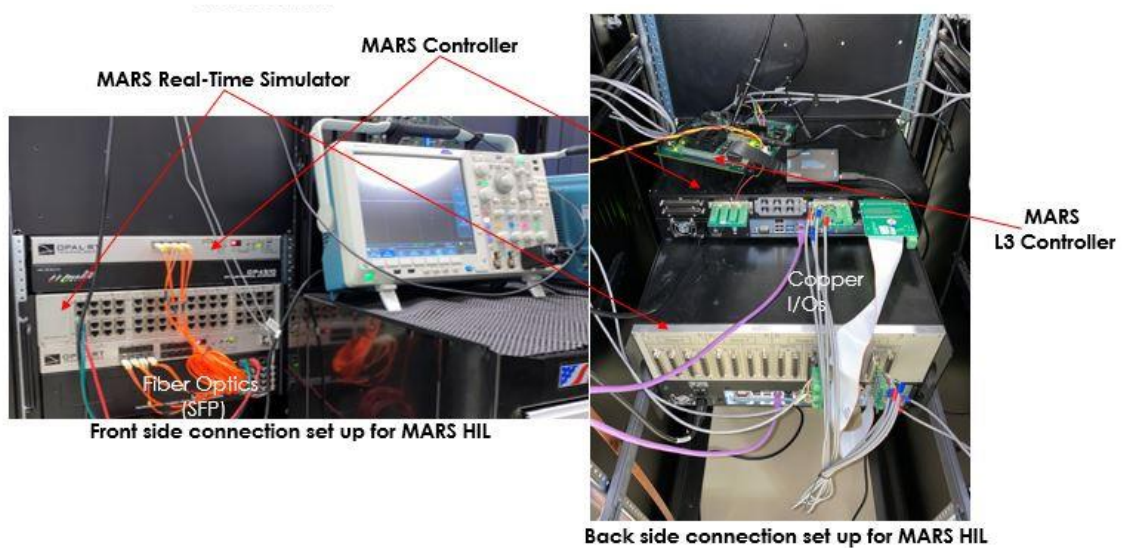


**Figure B.2 – The open loop MARS PE-HIL test layout.**

### **B.1 IEEE 1547-2018. PRC-024-3 compliance for voltage, and frequency support under defined disturbances**

The lowest voltage during three-phase fault and line-to-line fault under  $P_{ac}=P_{dc}=100\text{WM}$  are mapped onto the IEEE 1547-2018 voltage ride-through requirements and shown in Figure B.3. The same test has been applied to multiple

operating conditions. They can be visualized as point 1 and point 2, respectively. it can be observed that these two points are inside the permissive operation capability region and may ride-through region for three-phase fault and line-to-line fault in IEEE 1547-2018. The MARS system provided continuity of operation throughout during the three-phase fault and line-to-line fault. This indicates that the MARS system complies with the IEEE-1547-2018 as it provides continuity of operation without tripping during the three-phase fault and line-to-line fault under these three operating conditions.

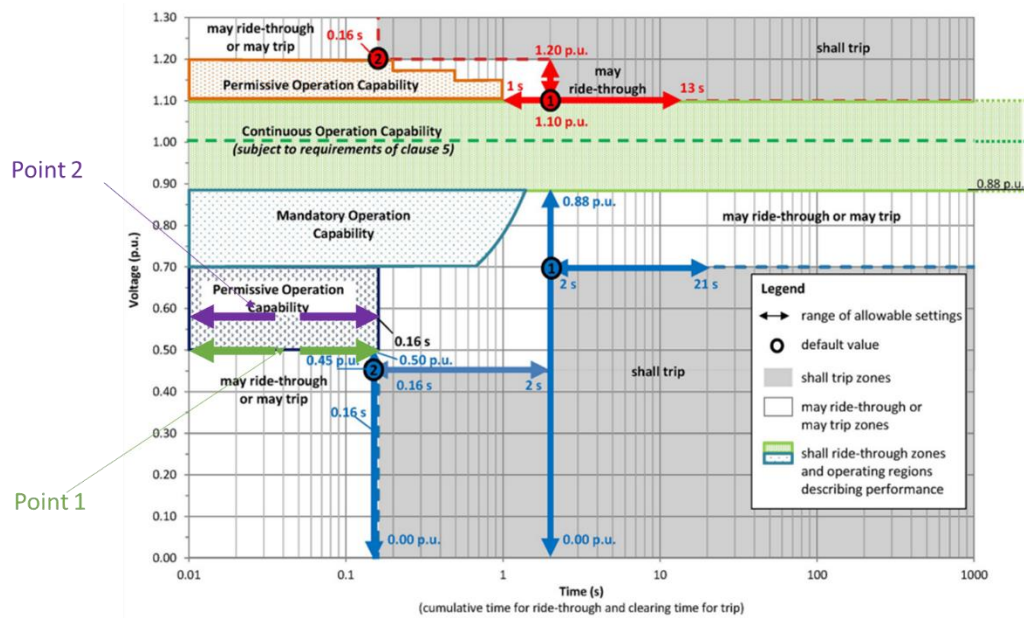


**Figure B.3 – Voltage ride-through requirements for IEEE 1547 2018 and duration for MARS at Pittsburg providing voltage support during balanced three-phase fault and unbalanced line-to-line fault.**

The grid frequency during the 804.44MW loss of generation with the frequency support from MARS as well as the no trip zone for the WECC grid are shown in Figure B.4 for the reference command of  $P_{ac}=P_{dc}=100\text{WM}$ . The same test has been applied to multiple operating conditions. It can be observed that the frequency nadir during the frequency disturbances is around 59.9Hz. The MARS system provides frequency support

during the loss of generation event, and the frequency nadir is always within the no-trip zone. As the system doesn't trip, it is in compliance with IEEE 1547-2018 and PRC-024-3 frequency protection settings. The grid side current and voltage, as well as the capacitor voltages, are provided to showcase the stable operation of MARS during the loss of generation event. MARS system can provide continuing operation during the loss of generation event.

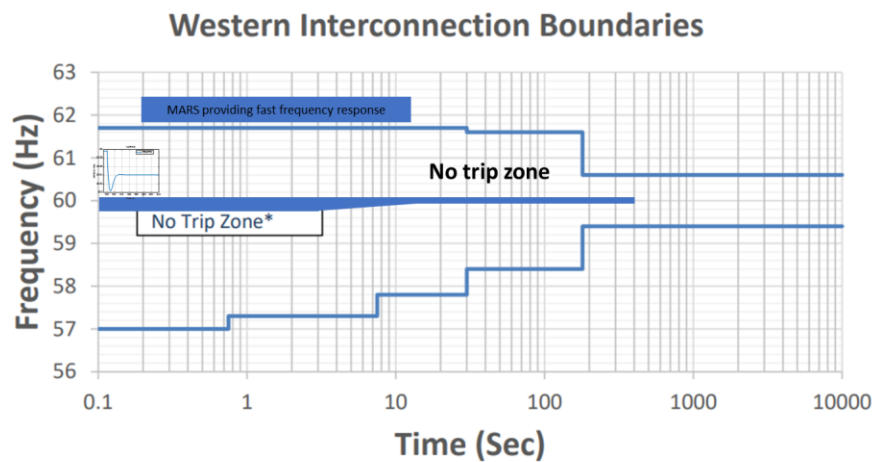


**Figure B.4 – Frequency protection setting for PRC-024-3 and preliminary characterization of MARS at Pittsburg based on fast frequency response provided by MARS during 804.4 MW loss of generation.**

## **B.2 Harmonics Compliance with IEEE 519-2014**

The total demand distortion (TDD) of the grid current of the MARS system at Pittsburg under different operating conditions are measured and the results under operating condition:  $P_{ac}=P_{dc}=100\text{WM}$  are shown in Figure B.5 (a). The corresponding instantaneous grid side current is shown in Figure B.5 (b). It can be observed from the figures that the TDD is well below the recommended limit of IEEE 519-2014 ( $<2\%$ ). This

indicates that the MARS system is in compliance with IEEE 519-2014 and the harmonics injected into the system by the MARS system do not affect the grid system.

**Operating condition1:  $P_{ac}=100\text{MW}$ ,  $P_{dc}=100\text{MW}$**

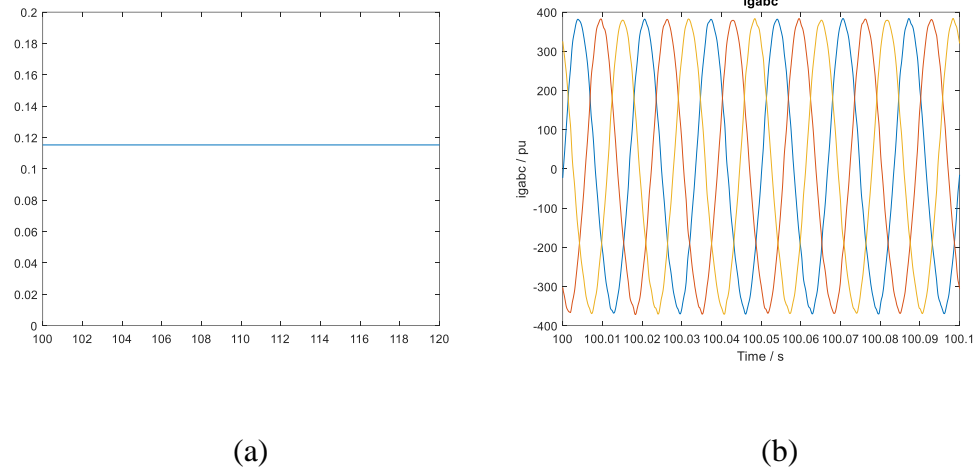


**Figure B.5 – Harmonics compliance for cHIL test: (a) TDD for grid current. (b)instantaneous grid current.**

### B.3 Harmonics Compliance with NERC PRC-024-3

Twelve different frequencies at the terminal of the MARS have been tested to evaluate the off-nominal frequency capability of MARS. They are marked as red dot in Figure B.6. Among the twelve frequency tests, ten test points lie on the off-normal frequency capability curve, the rest three test points lies within the curve. The frequency tests are achieved by replacing the WECC model with a frequency-controlled source, through changing the frequency input of the voltage source and changing the time duration. The cHIL experiments of thirteen tests points has been performed. For all the test points, the MARS system remains stable, and it provides continuity of operation without tripping during the events.



Three-phase faults with varying magnitudes and durations have been tested for 30 operating conditions. The fault magnitude and duration of the 28 tests pointed are illustrated on Figure B.7. Each test point is represented using a red dot. The rest 2 test points are long duration test which has fault magnitude of 0.9 and 1.1 respectively and both of them has a fault duration of 10,000s. Different magnitudes of the fault ride through tests are achieved by modifying the inductance (low voltage fault) or capacitance (over-voltage fault) of the three-phase fault and varying the location of the fault in WECC system. For all the test points, the MARS system remains stable, and it provides continuity of operation without tripping during the events.

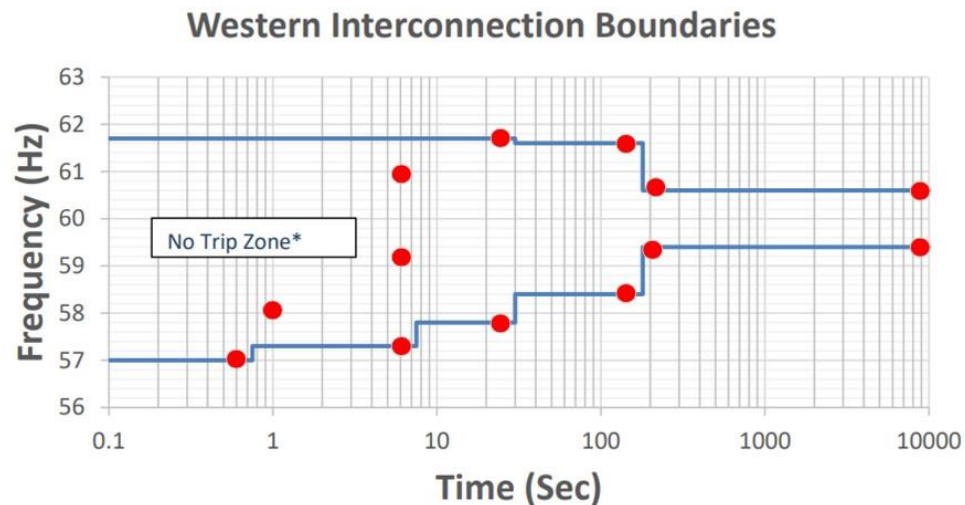


**Figure B.6 – Change in frequency tested at the western off normal frequency capability curve.**

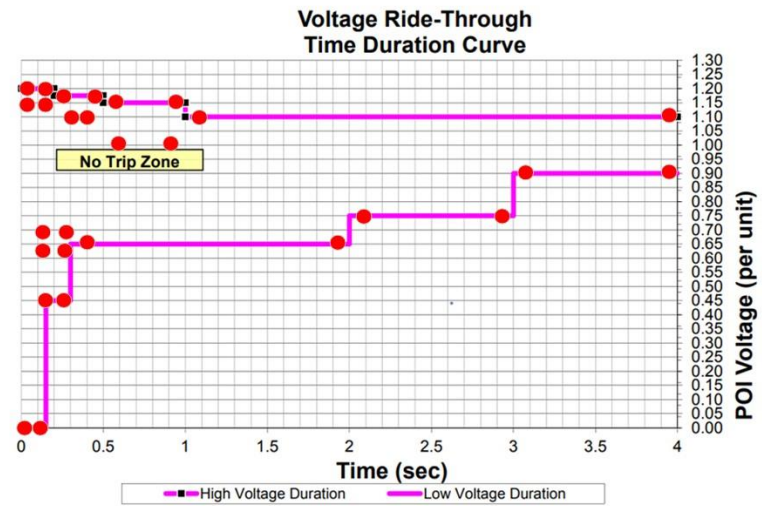


**Figure B.7 – Change in PCC voltage tested at the voltage ride-through time duration curve.**

## REFERENCES

- [1] IEA. Global energy review 2020. <https://www.iea.org/fuels-and-technologies/renewables>, 2020
- [2] IEA. Solar PV tracking report 2022. <https://www.iea.org/reports/solar-pv>, 2022
- [3] U.S. Energy Information Administration, “Most planned U.S. battery storage additions in next three years to be paired with solar”, Sep. 2021. <https://www.eia.gov/todayinenergy/detail.php?id=49756>
- [4] Enel Green Power, “Lily Solar + Storage Plant, USA”, <https://www.enelgreenpower.com/our-projects/operating/lily-solar-storage-plant>
- [5] M. Glinka and R. Marquardt, “A new AC/AC-multilevel converter family applied to a single-phase converter,” in *Power Electronics and Drive Systems*, 2003. PEDS 2003. The Fifth International Conference on, vol. 1, pp. 16–23 Vol.1, Nov 2003.
- [6] M. Glinka and R. Marquardt, “A new AC/AC multilevel converter family,” *IEEE Transactions on Industrial Electronics*, vol. 52, pp. 662–669, June 2005.
- [7] Gnanarathna, A. Gole, and R. Jayasinghe, “Efficient modeling of modular multilevel HVDC converters (MMC) on electromagnetic transient simulation programs,” *IEEE Transactions on Power Delivery*, vol. 26, pp. 316–324, Jan 2011.
- [8] Steffen Rohner, Steffen Bernet, Marc Hiller, and Rainer Sommer. “Modulation, losses, and semiconductor requirements of modular multilevel converters”, *IEEE transactions on Industrial Electronics*, 57(8):2633–2642, 2009.
- [9] K. Wang, Y. Li, and Z. Zheng, “Voltage balancing control and experiments of a novel modular multilevel converter,” in *2010 IEEE Energy Conversion Congress and Exposition (ECCE)*, pp. 3691–3696, Sept 2010.
- [10] R. Darus, J. Pou, G. Konstantinou, S. Ceballos, R. Picas, and V. Agelidis, “A modified voltage balancing algorithm for the modular multilevel converter: Evaluation for staircase and phase-disposition PWM,” *IEEE Transactions on Power Electronics*, vol. 30, pp. 4119–4127, Aug 2015.

- [11] Q. Tu, Z. Xu, and L. Xu, "Reduced switching-frequency modulation and circulating current suppression for modular multilevel converters," *IEEE Transactions on Power Delivery*, vol. 26, no. 3, pp. 2009–2017, Jul. 2011.
- [12] S. Li, X. Wang, Z. Yao, T. Li, and Z. Peng, "Circulating current suppressing strategy for MMC-HVDC based on nonideal proportional resonant controllers under unbalanced grid conditions," *IEEE Transactions on Power Electronics*, vol. 30, no. 1, pp. 387–397, Jan. 2015.
- [13] S. Yang, P. Wang, Y. Tang, M. Zagrodnik, X. Hu, and K. J. Tseng, "Circulating current suppression in modular multilevel converters with even-harmonic repetitive control," *IEEE Transactions on Industry Applications*, vol. 54, no. 1, pp. 298–309, Jan./Feb. 2018.
- [14] Z. Yang, P. Song, J. Song, X. Wang, and X. Li, "An MMC circulating current suppressing controller based on bridge arm common-mode voltage," *IEEE Access*, vol. 8, pp. 189471–189478, 2020.
- [15] M. Saeedifard and R. Iravani, "Dynamic performance of a modular multilevel back-to-back HVDC system," *IEEE Transactions on Power Delivery*, vol. 25, no. 4, pp. 2903–2912, Oct. 2010.
- [16] M. Hagiwara, K. Nishimura, and H. Akagi, "A modular multilevel PWM inverter for medium-voltage motor drives," *IEEE Energy Conversion Congress and Exposition (ECCE)*, Sep. 20–24, 2009, pp. 2557–2564.
- [17] Q. Tu, Z. Xu, and L. Xu, "Reduced switching-frequency modulation and circulating current suppression for modular multilevel converters," *IEEE Transactions on Power Delivery*, vol. 26, no. 3, pp. 2009–2017, July 2011.
- [18] L. Zhang, Z. Zhang, J. Qin, D. Shi and Z. Wang, "Design and performance evaluation of the modular multilevel converter (MMC)-based grid-tied PV-battery conversion system," *IEEE Energy Conversion Congress and Exposition (ECCE)*, Portland, OR, 2018, pp. 2649–2654.
- [19] F. Rong, X. Gong and S. Huang, "A novel grid-connected PV system based on mmc to get the maximum power under partial shading conditions," in *IEEE Transactions on Power Electronics*, vol. 32, no. 6, pp. 4320–4333, June 2017.

- [20] H. Bayat and A. Yazdani, "A power mismatch elimination strategy for an MMC-based photovoltaic system," in *IEEE Transactions on Energy Conversion*, vol. 33, no. 3, pp. 1519-1528, Sept. 2018.
- [21] T. Soong and P. W. Lehn, "Assessment of fault tolerance in modular multilevel converters with integrated energy storage," in *IEEE Transactions on Power Electronics*, vol. 31, no. 6, pp. 4085-4095, June 2016.
- [22] N. Li, F. Gao, T. Hao, Z. Ma and C. Zhang, "SOH balancing control method for the mmc battery energy storage system," in *IEEE Transactions on Industrial Electronics*, vol. 65, no. 8, pp. 6581-6591, Aug. 2018.
- [23] IEEE Standard Conformance Test Procedures for Equipment Interconnecting Distributed Energy Resources with Electric Power Systems and Associated Interfaces," in *IEEE Std 1547.1-2020*, vol., no., pp.1-282, 21 May 2020.
- [24] S. Rivera, B. Wu, R. Lizana, S. Kouro, M. Perez and J. Rodriguez, "Modular multilevel converter for large-scale multistring photovoltaic energy conversion system," *IEEE Energy Conversion Congress and Exposition (ECCE)*, 2013, pp. 1941-1946.
- [25] F. Rong, X. Gong and S. Huang, "A novel grid-connected PV system based on MMC to get the maximum power under partial shading conditions," in *IEEE Transactions on Power Electronics*, vol. 32, no. 6, pp. 4320-4333, June 2017.
- [26] N. Li, F. Gao, T. Hao, Z. Ma and C. Zhang, "SOH balancing control method for the MMC battery energy storage system," in *IEEE Transactions on Industrial Electronics*, vol. 65, no. 8, pp. 6581-6591, Aug. 2018.
- [27] A. Hillers and J. Biela, "Fault-tolerant operation of the modular multilevel converter in an energy storage system based on split batteries," *2014 16th European Conference on Power Electronics and Applications*, 2014, pp. 1-8.
- [28] G. Liang *et al.*, "Analytical derivation of intersubmodule active power disparity limits in modular multilevel converter-based battery energy storage systems," in *IEEE Transactions on Power Electronics*, vol. 36, no. 3, pp. 2864-2874, March 2021.
- [29] S. Debnath, J. Qin, B. Bahrani, M. Saeedifard and P. Barbosa, "Operation, control, and applications of the modular multilevel converter: A review," in *IEEE Transactions on Power Electronics*, vol. 30, no. 1, pp. 37-53, Jan. 2015.

- [30] M. Hagiwara, R. Maeda and H. Akagi, "Control and analysis of the modular multilevel cascade converter based on double-star chopper-cells (MMCC-DSCC)," in *IEEE Transactions on Power Electronics*, vol. 26, no. 6, pp. 1649-1658, June 2011.
- [31] M. Hagiwara, K. Nishimura and H. Akagi, "A modular multilevel PWM inverter for medium-voltage motor drives," *2009 IEEE Energy Conversion Congress and Exposition*, 2009, pp. 2557-2564.
- [32] F. Briz, M. López, A. Zapico, A. Rodríguez and D. Díaz-Reigosa, "Operation and control of MMCs using cells with power transfer capability," *2015 IEEE Applied Power Electronics Conference and Exposition (APEC)*, 2015, pp. 980-987.
- [33] Y. Ma, H. Lin, X. Wang, Z. Wang and Z. Ze, "analysis of battery fault tolerance in modular multilevel converter with integrated battery energy storage system," *2018 20th European Conference on Power Electronics and Applications (EPE'18 ECCE Europe)*, 2018, pp. P.1-P.8.
- [34] Z.Wang, H. Lin, and Y.Ma, "Improved capacitor voltage balancing control for multimode operation of modular multilevel converter with integrated battery energy storage system," *IET Power Electron.*, vol. 12, no. 11, pp. 2751–2760, Sep. 2019.
- [35] T. Soong and P. W. Lehn, "Internal power flow of a modular multilevel converter with distributed energy resources," in *IEEE Journal of Emerging and Selected Topics in Power Electronics*, vol. 2, no. 4, pp. 1127-1138, Dec. 2014.
- [36] H. Bayat and A. Yazdani, "A hybrid MMC-based photovoltaic and battery energy storage system," in *IEEE Power and Energy Technology Systems Journal*, vol. 6, no. 1, pp. 32-40, March 2019.
- [37] M. T. Wishart and R. G. Harley, "Identification and control of induction machines using artificial neural networks," in *IEEE Transactions on Industrial Applications.*, vol. 31, no. 3, pp. 612\_619, May 1995.
- [38] X. Sun, L. Chen, Z. Yang, and H. Zhu, "Speed-sensorless vector control of a bearingless induction motor with artificial neural network inverse speed observer," *IEEE/ASME Transactions on Mechatronics*, vol. 18, no. 4, pp. 1357\_1366, Aug. 2013.

- [39] M. Alzayed, H. Chaoui and Y. Farajpour, "Maximum power tracking for a wind energy conversion system using cascade-forward neural networks," in *IEEE Transactions on Sustainable Energy*, vol. 12, no. 4, pp. 2367-2377, Oct. 2021.
- [40] X. Liu *et al.*, "Event-Triggered neural-predictor-based FCS-MPC for MMC," in *IEEE Transactions on Industrial Electronics*, vol. 69, no. 6, pp. 6433-6440, June 2022.
- [41] S. Wang, T. Dragicevic, Y. Gao and R. Teodorescu, "Neural network based model predictive controllers for modular multilevel converters," in *IEEE Transactions on Energy Conversion*, vol. 36, no. 2, pp. 1562-1571, June 2021.
- [42] X. Liu *et al.*, "Predictor-based neural network finite-set predictive control for modular multilevel converter," in *IEEE Transactions on Industrial Electronics*, vol. 68, no. 11, pp. 11621-11627, Nov. 2021.
- [43] S. Wang, T. Dragicevic, G. F. Gontijo, S. K. Chaudhary and R. Teodorescu, "Machine learning emulation of model predictive control for modular multilevel converters," in *IEEE Transactions on Industrial Electronics*, vol. 68, no. 11, pp. 11628-11634, Nov. 2021.
- [44] X. Liu *et al.*, "Neural predictor-based low switching frequency fcs-mpc for mmc with online weighting factors tuning," in *IEEE Transactions on Power Electronics*, vol. 37, no. 4, pp. 4065-4079, April 2022.
- [45] P. Poblete, G. Pizarro, G. Droguett, F. Núñez, P. D. Judge and J. Pereda, "Distributed neural network observer for submodule capacitor voltage estimation in modular multilevel converters," in *IEEE Transactions on Power Electronics*, vol. 37, no. 9, pp. 10306-10318, Sept. 2022.
- [46] S. Wang, T. Dragicevic, Y. Gao, S. K. Chaudhary and R. Teodorescu, "Machine learning based operating region extension of modular multilevel converters under unbalanced grid faults," in *IEEE Transactions on Industrial Electronics*, vol. 68, no. 5, pp. 4554-4560, May 2021.
- [47] Q. Song, W. Liu, X. Li, H. Rao, S. Xu, and L. Li, "A steady-state analysis method for a modular multilevel converter," in *IEEE Transactions on Power Electronic.*, vol. 28, no. 8, pp. 3702-3713, Aug. 2013.

- [48] G. Konstantinou, J. Pou, D. Pagano, and S. Ceballos, "A hybrid modular multilevel converter with partial embedded energy storage," in *Energies*, vol. 9, no. 12, pp. 1012–1029, Sep. 2016.
- [49] J. I. Leon, S. Vazquez, and L. G. Franquelo, "Multilevel converters: Control and modulation techniques for their operation and industrial applications," in *Proc. IEEE*, vol. 105, no. 11, pp. 2066–2081, Nov. 2017.
- [50] F. Z. Peng, W. Qian, and D. Cao, "Recent advances in multilevel converter/inverter topologies and applications," in *Proc. Int. Power Electron. Conf.*, Jun. 2010, pp. 492–501.
- [51] H. Kim, S. Kim, Y.-H. Chung, D. -W. Yoo, C. -K. Kim and K. Hur, "Operating Region of Modular Multilevel Converter for HVDC With Controlled Second-Order Harmonic Circulating Current: Elaborating P-Q Capability," in *IEEE Transactions on Power Delivery*, vol. 31, no. 2, pp. 493-502, April 2016.
- [52] S. Norrga, L. Ängquist and K. Ilves, "Operating region extension for multilevel converters in HVDC applications by optimization methods," in *10th IET International Conference on AC and DC Power Transmission (ACDC)*, 2012, pp. 1-6.
- [53] Z. Yang, K. Zhang, X. Li, Y. Li and P. Song, "A Control Strategy for Suppressing Submodule Capacitor Voltage Fluctuation of MMC Based on Circulating Current Voltage Drop Balance," in *IEEE Access*, vol. 9, pp. 9130-9141, 2021.
- [54] Y. Yi, G. Yang, C. Qian and Y. Gui, "Branch Voltage Balancing Control Strategy Based on the Transfer Power Model by Zero-Sequence Circulating Current for the Hexverter," in *IEEE Access*, vol. 10, pp. 44326-44336, 2022.
- [55] X. Pan *et al.*, "Decoupling Capacitor Minimization of an MMC-Based Photovoltaic System with Three-Winding Power Channel," in *IEEE Transactions on Power Electronics*, vol. 37, no. 1, pp. 1012-1026, Jan. 2022.
- [56] M. Vatani, M. Hovd and M. Saeedifard, "Control of the modular multilevel converter based on a discrete-time bilinear model using the sum of squares decomposition method," in *IEEE Transactions on Power Delivery*, vol. 30, no. 5, pp. 2179-2188, Oct. 2015.



- [57] L. He, K. Zhang, J. Xiong, and S. Fan, "A repetitive control scheme for harmonic suppression of circulating current in modular multilevel converters," in *IEEE Transactions on Power Electronics*, vol. 30, no. 1, pp. 471–481, Jan. 2015.
- [58] S. Debnath and M. Saeedifard, "A new hybrid modular multilevel converter for grid connection of large wind turbines," in *IEEE Transactions on Sustainable Energy*, vol. 4, no. 4, pp. 1051–1064, Oct. 2013.
- [59] J. Qin and M. Saeedifard, "Predictive control of a modular multilevel converter for a back-to-back HVDC system," *IEEE Transactions on Power Delivery*, vol. 27, no. 3, pp. 1538–1547, Jul. 2012.
- [60] M. Vatani, B. Bahrani, M. Saeedifard, and M. Hovd, "Indirect finite control set model predictive control of modular multilevel converters," *IEEE Transactions on smart grid*, vol. 6, no. 3, pp. 1520–1529, May 2015.
- [61] F. Zhang, W. Li, and G. Joós, "A voltage-level-based model predictive control of modular multilevel converter," *IEEE Transactions on Industrial Electronics*, vol. 63, no. 8, pp. 5301–5312, Aug. 2016.
- [62] P. Guo et al., "A novel two-stage model predictive control for modular multilevel converter with reduced computation," *IEEE Transactions on Industrial Electronics*, vol. 66, no. 3, pp. 2410–2422, Mar. 2019.
- [63] B. Gutierrez and S.-S. Kwak, "Modular multilevel converters (MMCS) controlled by model predictive control with reduced calculation burden," *IEEE Transactions on Power Electronics*, vol. 33, no. 11, pp. 9176–9187, Nov. 2018.
- [64] X. Liu, L. Qiu, Y. Fang, Z. Peng, and D. Wang, "Finite-level-state model predictive control for sensorless three-phase four-arm modular multilevel converter," *IEEE Transactions on Power Electronics*, vol. 35, no. 5, pp. 4462–4466, May 2020.
- [65] S. Vazquez, C. Montero, C. Bordons, and L. G. Franquelo, "Design and experimental validation of a model predictive control strategy for a VSI with long prediction horizon," in *Ind. Electron. Soc., 39th Annu. Conf. IEEE*, 2013, pp. 5788–5793.
- [66] S. Mariéthoz and M. Morari, "Explicit model-predictive control of a PWM inverter with an LCL filter," *IEEE Transactions on Industrial Electronics*, vol. 56, no. 2, pp. 389–399, Feb. 2009.

- [67] H. Mahmoudi, M. Aleenejad, and R. Ahmadi, "Modulated model predictive control of modular multilevel converters in VSC-hvdc systems," *IEEE Transactions on Power Delivery*, vol. 33, no. 5, pp. 2115–2124, Oct. 2018.
- [68] A. Moraet et al., "Model-predictive-control-based capacitor voltage balancing strategies for modular multilevel converters," *IEEE Transactions on Industrial Electronics*, vol. 66, no. 3, pp. 2432–2443, 2018.
- [69] G. Darivianakis, T. Geyer and W. van der Merwe, "Model predictive current control of modular multilevel converters," *2014 IEEE Energy Conversion Congress and Exposition (ECCE)*, 2014, pp. 5016-5023.
- [70] S. Debnath, P. R. V. Marthi, Q. Xia, J. Pan, M. Saeedifard, V. N. Vipin, S. Chakraborty, and M. Arifujjaman, "Renewable integration in hybrid ac/dc systems using a multi-port autonomous reconfigurable solar power plant (MARS)," in *IEEE Transactions on Power Systems*, vol. 36, no. 1, pp. 603–612, 2021.
- [71] M. N. Kheraluwala, R. W. Gascoigne, D. M. Divan and E. D. Baumann, "Performance characterization of a high-power dual active bridge DC-to-DC converter," in *IEEE Transactions on Industry Applications*, vol. 28, no. 6, pp. 1294-1301, Nov.-Dec. 1992.
- [72] A. Jones, Title of book, Publisher's Name, City, 2004 H. Qin and J. W. Kimball, "Generalized average modelling of dual active bridge dc-dc converter," *IEEE Transactions on Power Electronics*, vol. 27, no. 4, pp. 2078–2084, 2012.
- [73] A. C. Zhao, S. D. Round, and J. W. Kolar, "Full-order averaging modelling of zero-voltage-switching phase-shift bidirectional dc-dc converters," *IET Power Electronics*, vol. 3, no. 3, pp. 400–410, 2010.
- [74] L. Shi, W. Lei, Z. Li, J. Huang, Y. Cui, and Y. Wang, "Bilinear discrete time modeling and stability analysis of the digitally controlled dual active bridge converter," *IEEE Transactions on Power Electronics*, vol. 32, no. 11, pp. 8787–8799, 2017.
- [75] S. Debnath and M. Chinthavali, "Numerical-Stiffness-Based Simulation of Mixed Transmission Systems," in *IEEE Transactions on Industrial Electronics*, vol. 65, no. 12, pp. 9215-9224, Dec. 2018.
- [76] S. Pingel et al., "Potential induced degradation of solar cells and panels," in *Proc. 35th IEEE Photovolt. Spec. Conf.*, Jun. 2010, pp. 002817–002822.

- [77] R. T. Naayagi, A. J. Forsyth, and R. Shuttleworth, "Bidirectional control of a dual active bridge dc-dc converter for aerospace applications," *IET Power Electron.*, vol. 5, pp. 1104–1118, Aug. 2012.
- [78] P. R. V. Marthi, S. Debnath, Q. Xia and M. Saeedifard, "Advanced models and fast simulation algorithms for MARS plants," *2020 IEEE/PES Transmission and Distribution Conference and Exposition (T&D)*, Chicago, IL, 2020, pp. 1-5.
- [79] X. She, A. Huang, X. Ni and R. Burgos, "AC Circulating Currents Suppression in Modular Multilevel Converter," *IECON 2012 - 38th Annual Conference on IEEE Industrial Electronics Society*, 2012, pp. 191-196.
- [80] H. Knaak, "Modular multilevel converters and HVdc/FACTS: A success story," in *Proc. 2011 14th European Conference on Power Electronics and Applications*, pp. 1-6.
- [81] S. Debnath, P. R. V. Marthi, Z.Dong, Q.Xia, " Power Electronic Hardware-in-the-Loop (PE-HIL): Testing Individual Controllers in Large-Scale Power Electronics Systems," *IEEE Energy Conversion Congress and Exposition (ECCE)*, 2022.
- [82] S. Rohner, S. Bernet, M. Hiller, and R. Sommer, "Modelling, simulation and analysis of a modular multilevel converter for medium voltage applications," in *Proc. IEEE Int. Conf. Ind. Technol.*, 2010, pp. 775–782.
- [83] S. Debnath, Q. Xia, M. Saeedifard, and M. Arifujjaman, "Advanced high-fidelity lumped emt grid modelling & comparison" *CIGRE Grid of the Future*, 2019.
- [84] M. Vasiladiotis, and A. Rufer , "Analysis and control of modular multilevel converters with integrated battery energy storage," *IEEE Transactions on Power Electronics*, vol. 30, no. 1, pp. 163-175, 2015.